Journal of Mammalian Evolution (2021) 28:1083–1143
https://doi.org/10.1007/s10914-021-09584-3

ORIGINAL PAPER

New Skull Material of *Taeniolabis taoensis* (Multituberculata, Taeniolabididae) from the Early Paleocene (Danian) of the Denver Basin, Colorado

David W. Krause[1,2] · Simone Hoffmann[3] · Tyler R. Lyson[1] · Lindsay G. Dougan[1] · Holger Petermann[1] · Adrienne Tecza[1] · Stephen G. B. Chester[4,5,6] · Ian M. Miller[1,7]

Accepted: 27 October 2021

Abstract

Taeniolabis taoensis is an iconic multituberculate mammal of early Paleocene (Puercan 3) age from the Western Interior of North America. Here we report the discovery of significant new skull material (one nearly complete cranium, two partial crania, one nearly complete dentary) of *T. taoensis* in phosphatic concretions from the Corral Bluffs study area, Denver Formation (Danian portion), Denver Basin, Colorado. The new skull material provides the first record of the species from the Denver Basin, where the lowest in situ specimen occurs in river channel deposits ~730,000 years after the Cretaceous-Paleogene boundary, roughly coincident with the first appearance of legumes in the basin. The new material, in combination with several previously described and undescribed specimens from the Nacimiento Formation of the San Juan Basin, New Mexico, is the subject of detailed anatomical study, aided by micro-computed tomography. Our analyses reveal many previously unknown aspects of skull anatomy. Several regions (e.g., anterior portions of premaxilla, orbit, cranial roof, occiput) preserved in the Corral Bluffs specimens allow considerable revision of previous reconstructions of the external cranial morphology of *T. taoensis*. Similarly, anatomical details of the ascending process of the dentary are altered in light of the new material. Although details of internal cranial anatomy (e.g., nasal and endocranial cavities) are difficult to discern in the available specimens, we provide, based on UCMP 98083 and DMNH.EPV 95284, the best evidence to date for inner ear structure in a taeniolabidoid multituberculate. The cochlear canal of *T. taoensis* is elongate and gently curved and the vestibule is enlarged, although to a lesser degree than in *Lambdopsalis*.

Keywords *Taeniolabis taoensis* · Multituberculata · Mammalia · Skull anatomy · Paleocene · Denver basin

✉ David W. Krause
David.Krause@dmns.org

Simone Hoffmann
simone.hoffmann@nyit.edu

Tyler R. Lyson
Tyler.Lyson@dmns.org

Lindsay G. Dougan
Lindsay.Dougan@dmns.org

Holger Petermann
Holger.Petermann@dmns.org

Adrienne Tecza
Adrienne.Tecza@dmns.org

Stephen G. B. Chester
StephenChester@brooklyn.cuny.edu

Ian M. Miller
imiller@ngs.org

[1] Department of Earth Sciences, Denver Museum of Nature & Science, 2001 Colorado Boulevard, Denver, CO 80205, USA

[2] Department of Anatomical Sciences, Stony Brook University, Stony Brook, NY 11794-8081, USA

[3] Department of Anatomy, College of Osteopathic Medicine, New York Institute of Technology, Old Westbury, NY 11568, USA

[4] Department of Anthropology, Brooklyn College, City University of New York, 2900 Bedford Avenue, Brooklyn, NY 11210, USA

[5] Department of Anthropology, The Graduate Center, City University of New York, 365 Fifth Avenue, New York, NY 10016, USA

[6] New York Consortium in Evolutionary Primatology, 200 Central Park West, New York, NY 10024, USA

[7] National Geographic Society, 1145 17th Street NW, Washington, DC 20036, USA

Introduction

Multituberculates were arguably the most successful evolutionary radiation of early mammals. Their temporal range extended from at least the Middle Jurassic to the late Eocene, an interval of approximately 130 million years (Kielan-Jaworowska et al. 2004; Butler and Hooker 2005; Schumaker and Kihm 2006; Dawson and Constenius 2018). They were most speciose and abundant in the Late Cretaceous (Judithian through Lancian North American Land Mammal Ages [NALMA]) and Paleocene of North America (Krause 1986; Cifelli et al. 2004; Kielan-Jaworowska et al. 2004; Weil and Krause 2008), represented by approximately 150 species and literally tens of thousands of specimens. It is therefore surprising that, despite this diversity and abundance, the skull anatomy of Late Cretaceous/Paleogene North American multituberculates is still very poorly known.

By contrast, complete or nearly complete skulls are known for a plethora of Late Cretaceous and Paleocene Asian multituberculate genera that have been described and analyzed in great detail (see reviews and reconstructions in Kielan-Jaworowska et al. 2004: figs. 8.38–8.40 and Wible et al. 2019: figs. 21–23). Skull material of Late Cretaceous European multituberculates is limited to brief descriptions of partial crania of the genera *Kogaionon* (Rădulescu and Samson 1996; reconstructed in Kielan-Jaworowska et al. 2004: fig. 8.42A), *Barbatodon* (Smith and Codrea 2015), and *Litovoi* (Csiki-Sava et al. 2018) and incomplete dentaries of *Barbatodon* (Csiki et al. 2005; Smith and Codrea 2015; Solomon et al. 2016). Although multituberculates have been reported from the southern supercontinent Gondwana (see review in Krause et al. 2017), no cranial material is known. A small fragment of a dentary was assigned to the possible multituberculate *Ferugliotherium* by Kielan-Jaworowska and Bonaparte (1996), but the affinities of *Ferulgiotherium* remain enigmatic (summarized in Rougier et al. 2021).

Dentaries are known for a plethora of North American multituberculate taxa but, aside from the cranial material of the early Paleocene (Puercan NALMA) *Taeniolabis taoensis* that is the subject of this report, substantial cranial specimens have been recorded for only three other species: (1) the Paleocene (Torrejonian NALMA) ptilodontid *Ptilodus montanus* (see Gidley 1909; Broom 1914; Simpson 1937b, c; Hopson et al. 1989; Wall and Krause 1992; Krause and Kielan-Jaworowska 1993), (2) the Paleocene (Tiffanian NALMA) microcosmodontid *Microcosmodon conus* (see Fox 2005), and (3) the Eocene (Wasatchian NALMA) neoplagiaulacid *Ectypodus tardus* (see Sloan 1979). The skull of *Ectypodus tardus* (YPM VPPU 14724) was never described comprehensively, although some details were mentioned in several papers (e.g., Krause 1982a; Wible 1991; Gambaryan and Kielan-Jaworowska 1995; Wible and Rougier 2000; Kielan-Jaworowska et al. 2005; Rougier et al. 2016; Wible et al. 2019) following Sloan's (1979) brief overview of it. A cranial fragment including the posterior part of the snout and the orbital region, identified as belonging to the Paleocene (Tiffanian) neoplagiaulacid *Ectypodus* sp. C (since referred to *Krauseia clemensi* by Vianey-Liaud 1986), has also not been described in detail (Gingerich et al. 1983). Some isolated cranial fragments of the Late Cretaceous (Maastrichtian) eucosmodontid *Stygimys kuszmauli* and the neoplagiaulacid *Mesodma thompsoni* were illustrated but given only cursory treatment by Sloan and Van Valen (1965: figs. 3, 4). In addition, the discovery of several skulls of the Late Cretaceous (Campanian) North American ptilodontoid *Filikomys primaevus* was announced in a recent brief paper by Weaver et al. (2021) but these specimens also remain to be described in detail; a partial rostrum of this species was initially attributed to *Cimexomys judithae* by Montellano et al. (2000). Finally, skulls of the Late Cretaceous (Maastrichtian) North American cimolomyid *Meniscoessus robustus* (see Weil and Tomida 2001, 2003, 2017) and the Paleocene (Tiffanian) neoplagiaulacid *Neoplagiaulax* sp. (Kotrappa and Farke 2015) have been reported in conference abstracts but remain largely undescribed.

Taeniolabis taoensis is an iconic Paleocene mammal from the Western Interior of North America, illustrated as a representative of the Multituberculata in many textbooks and other secondary literature sources for over a century (e.g., Scott 1913; Simpson 1937a; Romer 1966; Kermack and Kermack 1984; Kurtén 1971; Savage and Long 1986; Rose 2006; Prothero 2017). It is notable in several respects:

1. *T. taoensis* (Cope 1882c) was among the first Cenozoic multituberculates to be described. The species was initially placed in the genus *Polymastodon* but was later deemed to be synonymous with the earlier-named *Taeniolabis sulcatus* Cope, 1882b, which is now considered a nomen dubium (see complicated history of synonymies in Simmons 1986, 1987). *Neoplagiaulax eocaenus* Lemoine, 1880 from Europe and *Ptilodus mediaevus* Cope, 1881 from North America were named in the year or two preceding the description of *T. taoensis*. *Catopsalis foliatus* Cope, 1882a was described earlier in the same year as *Polymastodon taoensis* Cope, 1882c. *Catopsalis pollux* (Cope, 1882c), now also a junior synonym of *T. taoensis*, and *Ptilodus trovessartianus* (Cope, 1882c), now placed in *Parectypodus* (see Krause 1977; Tsentas 1981), were described in the same paper as *Polymastodon taoensis*.

2. *T. taoensis* (Cope, 1882c) is the type species of the genus *Taeniolabis* Cope, 1882b, which is the type genus of the Taeniolabididae Granger and Simpson (1929), and, in turn, the Taeniolabidoidea Sloan and Van Valen (1965).
3. *T. taoensis* is commonly used to provide phylogenetically defined clade names for several higher mammalian taxa. Sereno (2006:319) defined Theriiformes as the "least inclusive clade containing *Mus musculus* Linnaeus, 1758 and *Taeniolabis taoensis* (Cope, 1882c)"; Allotheria as the "most inclusive clade containing *Taeniolabis taoensis* (Cope, 1882c) but not *Mus musculus* Linnaeus, 1758 or *Ornithorhynchus anatinus* (Shaw, 1799)"; and Multituberculata as the "least inclusive clade containing *Taeniolabis taoensis* (Cope, 1882c) and *Paulchoffatia delgadoi* Kühne, 1961." Similarly, Williamson et al. (2016: 200) defined Taeniolabidoidea "as the most inclusive clade containing *T. taoensis* Cope, 1882c, but not *Es. [sonodon] browni* Simpson, 1927, *Men.[iscoessus] robustus* Marsh, 1889a, *Cimo.[lomys] gracilis* Marsh, 1889a *Cime.[xomys] judithae* Sahni, 1972, *Catopsbaatar catopsaloides* (Kielan-Jaworowska, 1974); *Eu. [cosmodon] molestus* Cope, 1886; *Mesodma formosa* Marsh, 1889b; *Ptilodus montanus* Douglass, 1908; *Krauseia clemensi* (Sloan, 1981), *Mi.[crocosmodon] conus* Jepsen, 1930, *Buginbaatar transaltaiensis* Kielan-Jaworowska and Sochava, 1969, *Kogaionon ungureanui* Rădulescu and Samson (1996), or *Boffius splendidus* Vianey-Liaud, 1979." They also defined Taeniolabididae as "the most inclusive clade containing *T. taoensis* (Cope, 1882c), but not *L.[ambdopsalis] bulla* Chow and Qi, 1978" and, conversely, Lambdopsalidae as "the most inclusive clade containing *L. bulla* Chow and Qi, 1978, and not *T. taoensis* (Cope, 1882c)." Finally, Hoffmann et al. (2020: 215) defined Gondwanatheria phylogenetically "as the most inclusive clade including *Gondwanatherium* but not *Taeniolabis*, *Cifelliodon*, or *Shenshou*."
4. *T. taoensis* is an index taxon that defines the base of the third of three Puercan (early Paleocene) NALMA biochrons – this is the *Taeniolabis taoensis/Periptychus carinidens* Interval Zone (Pu3) of Lofgren et al. (2004). The Corral Bluffs section of the Denver Formation was specifically recognized by Archibald et al. (1987) as one of only two other areas where both Pu2 and Pu3 Interval Zones might be recognized but the section had not, in fact, yielded remains of *T. taoensis*. That deficiency was also noted by Eberle (2003), Lofgren et al. (2004), and Dahlberg et al. (2016) but was eliminated with the discovery of several specimens of *T. taoensis* reported by Lyson et al. (2019a) that are described in detail in this paper.
5. *T. taoensis* is the largest known multituberculate and, more broadly, the largest known allotherian. Cope (1882b) initially estimated that it was the size of a sheep but later (Cope 1882c, 1884a) concluded that it equaled or exceeded the size of *Macropus giganteus* (= *M. major*), the Eastern Grey Kangaroo, males of which can reach up to 90 kg (Poole 1982). Romer (1966) drew a size comparison with woodchucks (*Marmota monax*), which have body masses ranging from 3.1 to 5.1 kg (Kwiecinski 1998), whereas Sloan (1979) estimated a body mass of 40 kg. More recent workers (Kielan-Jaworowska et al. 2004; Weil and Krause 2008; Scott et al. 2016) have suggested a body mass more comparable to that of, or even larger than, the North American beaver *Castor canadensis* (normally ~12–20 kg but up to 39 kg; Jenkins and Busher 1979). Evans et al. (2012) estimated the maximum body mass of *T. taoensis* to be 30 kg. Wilson et al. (2012) employed a formula based on m1 area that yielded a body mass estimate of > 100 kg for the species. However, Wilson and colleagues concluded that the scaling of m1 area to body mass is different in multituberculates than in the therian reference group and therefore that cranial length would be a more accurate predictor for large multituberculates. When they employed this metric, their estimate was 22.7 kg for *T. taoensis*. Williamson et al. (2016) also reported a marked discrepancy in size when employing m1 area (103.0–107.6 kg) versus skull length (21.8 kg). Scott et al. (2016) developed a variety of body mass estimates for taeniolabidids based on tooth row length and m1 area. Like Wilson et al. (2012) and Williamson et al. (2016), their estimates based on m1 area were very high for *T. taoensis*, ranging from 33.6 to 107.5 kg but, when based on tooth row length, were much smaller, 7.7 to 19.4 kg. Finally, based on a nearly complete cranium described herein (DMNH EPV.95284) and using regressions based on cranial size (geometric mean of maximum cranial length and width), Lyson et al. (2019a) obtained a mean estimate of 34.0 kg for the body mass of *T. taoensis* (95% confidence interval = 20.8–55.6 kg).
6. *T. taoensis* has long been considered to be the "most specialized of known multituberculates" (e.g., Granger and Simpson 1929: 611; Matthew 1937) and to possess the most derived dentition of any known multituberculate. The species has among the fewest teeth of any multituberculate (dental formula of 2.0.1.2/1.0.1.2 shared with at least *Lambdopsalis* and *Sphenopsalis*, compared to as high as 3.1.5.2/1.0.4.2 for the most plesiomorphic multituberculates – see Krause et al. 2020d: Table 4). Furthermore, of the large number of multituberculate species sampled by Wilson et al. (2012), *T. taoensis* has the highest orientation patch count (OPC), a measure of dental complexity (Evans et al. 2007). The OPC value for *T. taoensis* even exceeds that of extant herbivorous rodents.

Despite its iconic status, *T. taoensis* is not particularly well known anatomically, in part because many of the plethora of previously discovered specimens have not yet been described and in part because, as for most fossil mammalian species, the vast majority of the known specimens are isolated teeth and fragmentary jaws, primarily dentaries. Previous description of cranial material of *T. taoensis* is largely based on a single specimen, AMNH 16321. This specimen was discovered by W. J. Sinclair in 1913 in numerous fragments that were pieced together by W. Granger and described by Broom (1914), Granger and Simpson (1929), and Simpson (1937b). AMNH 16321 is fairly complete but is highly fragmented and missing the entire mesocranial and basicranial regions, as well as most of the palate and the lateral wall of the braincase. The lower jaw is known primarily from AMNH 16310, a left dentary comprised of the horizontal ramus and the anterior portion of the ascending ramus, and AMNH 745, a left dentary preserving the condylar region, also described by the same authors. Although well preserved, AMNH 16310 is lacking the posterior half of the ascending ramus whereas AMNH 745 consists of several fragments and is missing most of the dorsal portion of the ascending ramus. Cope (1884a, 1884b), Osborn and Earle (1895), Gregory (1910), Broom (1914), and several others (see "Description" below) also described and/or illustrated partial dentaries, including AMNH 748 and AMNH 968, which, again, do not completely preserve portions of the ascending ramus. A nearly complete but considerably deformed cranium and lower jaws, UCMP 98083, was illustrated by Greenwald (1988) but not described; because it was of a juvenile, it was employed by Greenwald in a study of dental eruption and replacement in multituberculates.

Here, with the assistance of micro-computed tomography (μCT), we describe significant new skull material (one nearly complete cranium, two partial crania, and a nearly complete dentary) of *T. taoensis* recovered from the Corral Bluffs study area, Denver Formation, Denver Basin, Colorado. The new skull material provides the first record of the species from the basin (Lyson et al. 2019a). Furthermore, also employing μCT imaging, we more fully describe AMNH 16310, AMNH 16321, and UCMP 98083 from the Nacimiento Formation of the San Juan Basin, New Mexico. This study is the first to apply μCT technology to specimens of any species of *Taeniolabis* and, in fact, to any of the known crania of North American Cenozoic multituberculates. This contribution will be limited to description of the skull anatomy of *T. taoensis* and comparison to that of other taeniolabidoids. Some taeniolabidid craniodental material recovered from the Denver Basin does not appear to be referable to *T. taoensis* and will be described in a subsequent paper, which will include a phylogenetic analysis and reassessment of taeniolabidoid species relationships. The current paper is intended to provide the comparative anatomical foundation for this future, more analytical work.

Geological Setting, Age Control, and Paleobotanical Context

The Corral Bluffs study area is located immediately east (~20 km) of the Colorado Front Range in the southwestern corner of the Denver Basin and within the eastern city limits of Colorado Springs, Colorado, USA (Fig. 1). The basin contains Cambrian through Eocene rocks including synorogenic strata that were deposited during both the Ancestral Rockies and Laramide orogenies. During the Late Cretaceous and Early Paleogene, the basin was a depocenter and accumulated synorogenic sediments that occur in two unconformity-bound packages informally named the Denver 1 (D1) and Denver 2 (D2) sequences (Raynolds 1997, 2002). The D1 sequence, which comprises the exposure in the Corral Bluffs study area, is the earlier of the two synorogenic sequences and is comprised of the Denver Formation (Maastrichtian and Danian) and the lower Dawson Formation. The D1 sequence overlies the Laramie Formation and is overlain by the upper Dawson Formation that forms the D2 sequence (Raynolds and Johnson 2003; Dechesne et al. 2011). The D1 sequence accumulated in the Denver Basin between ca. 68 and 64 Ma during the early Laramide Orogeny and is composed of reworked Mesozoic and Paleozoic sediments as well as Precambrian basement rock shed during uplift of the Colorado Front Range (Raynolds 1997, 2002; Raynolds and Johnson 2003). In the Corral Bluffs study area, the D1 sequence is dominated by sandstone and mudstone beds interpreted to represent riverine and floodplain depositional environments including channel, crevasse splay, and ponded water settings (Lyson et al. 2019a).

Megafloral and fragmentary vertebrate fossils were first discovered in Corral Bluffs in the early 1900s (Lee 1913). Studies on these collections, as well as on subsequent fossil discoveries throughout the 1900s and early 2000s, largely focused on the biostratigraphy of Corral Bluffs. Early analyses noted fragmentary dinosaur fossils in arroyos at the base of the bluffs and archaic early Paleocene mammal fossils eroding out of well-exposed, cliff-forming strata higher in the bluffs. These early fossil collections were used to loosely determine the placement of the Cretaceous/Paleogene (K/Pg) boundary in the section (Knowlton 1930; Gazin 1941; Brown 1943). Subsequent biostratigraphic work identified Puercan 2 (Pu2) interval zone mammals collected from the cliff-forming portion of the bluffs (Middleton 1983; Eberle 2003). In addition, several studies documented the diversity of mammals (Middleton 1983; Eberle 2003), turtles (Middleton 1983; Hutchison and Holroyd 2003; Lyson and Joyce 2011), and plants (Benson 1998; Johnson et al. 2003), with some of the turtle specimens being exceptionally complete (Lyson et al. 2021a, 2021b). More recently,

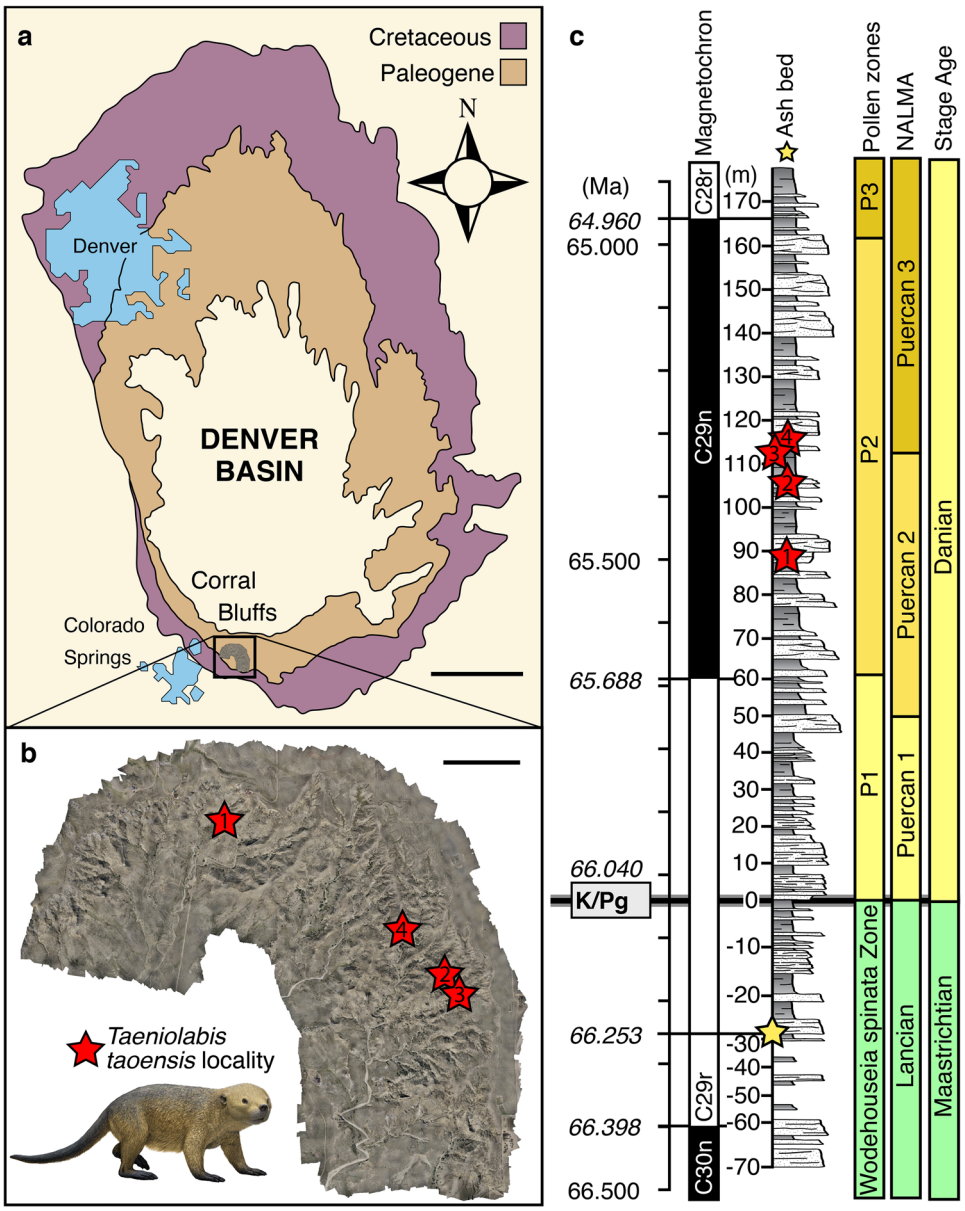

Fig. 1 Geographic, magnetostratigraphic, lithostratigraphic, chronostratigraphic, and biostratigraphic placement of localities at which specimens of *Taeniolabis taoensis* occur in the Denver Basin. **a**, Map of the Denver Basin showing the location of the Corral Bluffs study area (highlighted by box and enlarged in part b) in the southwestern region of the basin. **b**, High-resolution photogrammetry model of the eastern portion of the Corral Bluffs study area that produced specimens of *T. taoensis* (denoted by red stars): 1 – DMNH EPV.136300/DMNH Loc. 12111; 2 – DMNH EPV.95284/DMNH Loc. 6266; 3 – DMNH EPV.134082/DMNH Loc. 6500; 4 – DMNH EPV.130973/DMNH Loc. 7064 (Table 1). **c**, Magnetostratigraphic, lithostratigraphic, chronostratigraphic, and biostratigraphic logs showing stratigraphic placement of localities at which specimens of *T. taoensis* (denoted by red stars) occur. Stratigraphy is tied to the Geomagnetic Polarity Time Scale (Gradstein et al. 2012; Ogg 2012) using remanent magnetization of the rocks in the Corral Bluffs study area, two CA-ID-TIMS U–Pb-dated volcanic ashes (denoted by yellow stars; these ash beds are at the same stratigraphic level and are interpreted as being the same laterally continuous bed that crops out approximately 750 m apart), and the palynologically defined K/Pg boundary (italicized dates) (Fuentes et al. 2019; Lyson et al. 2019a). The composite lithostratigraphic log is dominated by intercalated mudstone and sandstone, reflecting a variety of fluvial facies (Lyson et al. 2019a). Pollen interval zones are defined by diversification of *Momipites* spp. (family Juglandaceae) (Nichols and Fleming 2002) and placement of North American Land Mammal Ages (NALMA), as defined by Lofgren et al. (2004), is modified from Lyson et al. (2019a). Abbreviations: m, meters; Ma, million years ago; K/Pg, Cretaceous/Paleogene boundary. (modified from Lyson et al. 2019a). Scale bar in **a** = 20 km, **b** = 500 m

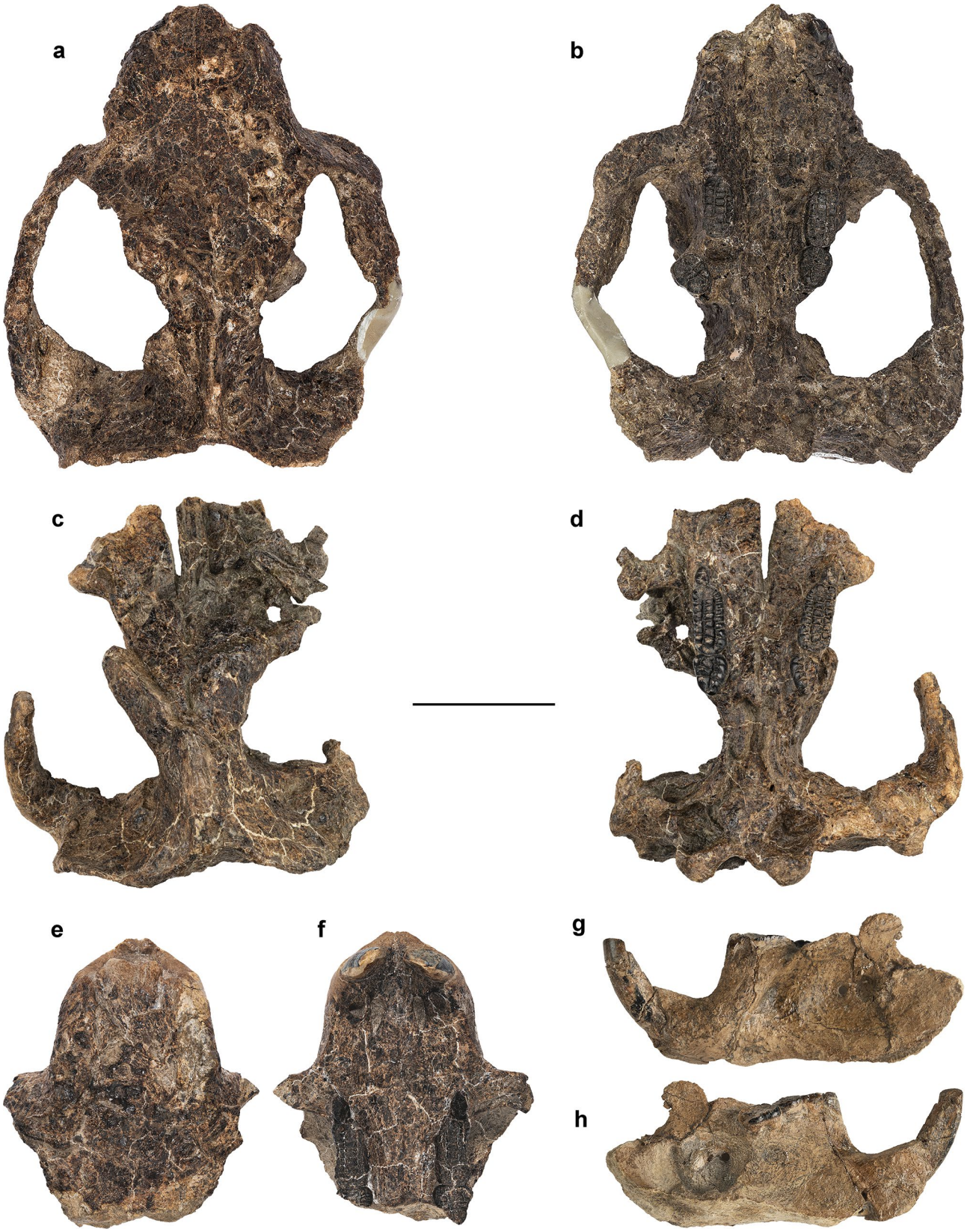
a
b
c
d
e
f
g
h

◂**Fig. 2** Skull material of *Taeniolabis taoensis* from the Denver Basin, Colorado. **a**, **b**, DMNH EPV.95284, nearly complete cranium in dorsal and ventral views. **c**, **d**, DMNH EPV.134082, posterior portion of cranium in dorsal and ventral views. **e**, **f**, DMNH EPV.136300, anterior portion of cranium in dorsal and ventral views. **g**, **h**, DMNH EPV.130973, left dentary in lateral and medial views. Scale bar = 5 cm

Lyson et al. (2019a) documented a remarkable assemblage of recently discovered vertebrate and megafloral fossil localities. Most vertebrate fossils are preserved in non-coprolite phosphatic concretions, a presently unique mode of preservation in terrestrial environments, and are exceptionally complete (Lyson et al. 2019a, 2021a, 2021b). Importantly, Lyson et al. (2019a) documented the presence of *Taeniolabis taoensis,* whose appearance defines the onset of the Pu3 interval zone (Lofgren et al. 2004) in the Denver Basin for the first time. This, coupled with the chronostratigraphic framework of Fuentes et al. (2019), provided a temporal foundation to determine the timing of the Pu2/Pu3 transition in the Denver Basin.

Six specimens provisionally referred to *T. taoensis* were available to Lyson et al. (2019a): two intact crania (DMNH EPV.95284, Fig. 2a, b; DMNH EPV.134082, Fig. 2c, d), one intact lower jaw (DMNH EPV.130973, Fig. 2g, h), and three fragmentary, unprepared specimens. With the then available material, Lyson et al. (2019a) conservatively placed the Pu2/3 boundary at the lowest in situ specimen (DMNH EPV.134082) of *T. taoensis*, approximately 113.4 m above the palynologically defined K/Pg boundary. They noted the possibility of an alternative placement of the Pu2/3 boundary ~6 m lower in the section (107.3 m above the K/Pg boundary) based on the presence of a nearly complete cranium (DMNH EPV.95284) found loose but intact on the surface of the outcrop (see Fig. 1c).

The three fragmentary specimens of *T. taoensis* noted by Lyson et al. (2019a) were found as float lower in the section (~90 m above the K/Pg boundary) on a broad, flat, upper surface of a large, laterally continuous, sandstone unit, informally referred to as the "Bill Sandstone" (Middleton 1983; Eberle 2003). The major sandstone beds in the Corral Bluffs study area, like the Bill Sandstone, are cliff forming, and often form "platforms" on their upper surface. As a result, they are major accumulation surfaces for concreted fossil material eroding out of the slopes above these surfaces. In the case of the three fragmentary specimens noted by Lyson et al. (2019a), additional preparation revealed that two of these specimens were misidentified and that the third is referable to a taeniolabidid that is likely not *Taeniolabis taoensis*; the latter specimen will be dealt with in a subsequent manuscript. However, since Lyson et al. (2019a), one additional fragmentary specimen referable to *T. taoensis* (DMNH EPV.136300, Fig. 2e, f), comprising the anterior portion of a cranium, was discovered as float on top of the Bill Sandstone unit and at the base of a ~15 m steep slope (Table 1, 89.8 m above the K/Pg boundary). Given that this specimen was found as float at the base of a steep slope on a major accumulation surface, we maintain the finding by Lyson et al. (2019a) of the placement of the Pu2/3 boundary at the lowest in situ *T. taoensis* specimen (DMNH EPV.134082) at approximately 113.4 m above the palynologically defined K/Pg boundary (Fig. 1c).

The four Corral Bluffs specimens currently referred to *T. taoensis* are from different localities and each is preserved in a phosphatic concretion. Two specimens were found in situ and two specimens were found as float (Table 1). One of the four specimens (lower jaw DMNH EPV.130973) was found in an amorphous mudstone facies that Lyson et al. (2019a) interpreted as representing a floodplain. Three of the four specimens (all cranial) were preserved in concretions that incorporated coarse sand in the groundmass, demonstrating that they eroded out of channel deposits. The association of relatively intact *T. taoensis* and other vertebrate specimens (e.g., crania, not isolated teeth) with coarse-grained lithologies suggested to Lyson et al. (2019a) that the specimens so

Table 1 Stratigraphic placement, age of locality (using two models), elements preserved, depositional environment, and type of occurrence (in situ vs displaced) for each specimen of *Taeniolabis taoensis* in the Denver Basin

DMNH Specimen#/ locality#	Stratigraphic position (m) above K/Pg boundary	Age model GPTS 2012 (Ma)	Age model Clyde et al. (2016) (Ma)	Element	Lithology/ Depositional environment	In situ?
EPV.130973/Loc. 7064	115.1	65.31	65.33	Nearly complete left dentary	Mudstone/ Floodplain	Yes
EPV.134082/Loc. 6500	113.4	65.32	65.35	Posterior portion of cranium	Sandstone/ River channel	Yes
EPV.95284/Loc. 6266	107.3	65.36	65.40	Nearly complete cranium	Sandstone/ River channel	No
EPV.136300/Loc. 12111	89.8	65.49	65.55	Anterior portion of cranium	Sandstone/ River channel	No

preserved represent species that probably inhabited riverine environments, based on the following logic:

1. Five facies were identified at the Corral Bluffs study area and sandstone-dominated facies were interpreted as representing riverine environments whereas finer grained siltstone- and mudstone-dominated facies were interpreted as representing overbank floodplain environments (Lyson et al. 2019a).
2. Other vertebrates found at the Corral Bluffs study area were also predominantly found within a specific lithology. For instance, baenid turtles have a strong association with a sandstone lithology and chelydroid turtles have a strong association with finer-grained siltstone and mudstone lithologies.
3. Both anatomical (Hutchison 1984; Lyson et al. 2019b) and sedimentological (Holroyd and Hutchison 2002; Lyson and Joyce 2009a, 2009b; Holroyd et al., 2014) data suggest that baenid turtles lived in aquatic riverine environments, while these same data suggest that chelydroid turtles lived in ponded water environments. Additionally, extant chelydroid taxa are predominately found in ponded water floodplain environments (Ernst and Barbour 1989).

Combined, these data suggest that the lithologic/taxon associations observed at the Corral Bluffs study area can be used to infer paleoenvironment, as has been used to infer other paleoecostyems (e.g., Lyson and Longrich 2011). As a result, consistent with the earlier analysis by Lyson et al. (2019a), we interpret the environment in which *T. taoensis* lived as dominated by river channels and corresponding floodplains draining the Laramide highlands to the west.

Precise stratigraphic placement for each specimen was obtained using the methods outlined in Lyson et al. (2019a; see also Table 1). This, coupled with the chronostratigraphic framework developed for the Corral Bluffs study area by Fuentes et al. (2019), allowed us to obtain precise ages for each *T. taoensis* specimen (Table 1). The chronostratigraphic framework is derived from the identification of three magnetochron boundaries (C30n/C29r, C29r/C29n, and C29n/C28r), the palynologically defined K/Pg boundary, and two chemical abrasion isotope dilution thermal ionization mass spectrometry (CA-ID-TIMS) $^{206}Pb/^{238}U$ dates on zircons separated from thin (ca. 2–3 cm thick) tonstein beds preserved within lignite beds (Fig. 1). The tonstein beds are interpreted to be the diagenetic remnants of volcanic ash falls into still water. These temporal benchmarks were used to calculate average sedimentation rates and interpolated ages for the section (Fuentes et al. 2019; Lyson et al. 2019a). Two age estimates for each *T. taoensis* specimen are provided based on two different age models (Table 1). These age models, the global Geomagnetic Polarity Time Scale (Gradstein et al. 2012) and estimates based on Denver Basin sediments (Clyde et al. 2016), have slight differences in the age estimates for the magnetochron boundaries and the K/Pg boundary. The interpolated ages for each *T. taoensis* specimen using both age models are provided in Table 1. Finally, considering recent biostratigraphic and magnetostratigraphic work in the section at Corral Bluffs, we note that all specimens of *T. taoensis* were recovered from sediments that include the *Momipites wyomingensis – Kurtzipites trispissatus* pollen zone (P2) and that all were found in magnetochron 29n (Nichols and Fleming 2002; Lyson et al. 2019a) (Fig. 1).

The stratigraphic placement of in situ *T. taoensis* specimens in the Corral Bluffs study area facilitates placement of this mammalian species in megafloral context. Lyson et al. (2019a) analyzed a dataset of 6,401 fossil leaves representing 233 morphospecies. These taxa were collected from 65 Late Cretaceous and early Paleocene localities covering ~1.2 Myr (30 m in the Late Cretaceous representing ~213 kyr, and 150 m in the early Paleocene representing ~917 kyr). They used this dataset to estimate plant raw richness, originations, extinctions, and standing richness, as well as mean annual temperature (MAT). At ~110 m above the palynologically defined K/Pg boundary, equivalent with the Pu2/Pu3 boundary as defined by the lowest in situ *T. taoensis* specimen (at 113.4 m), these data show the highest levels of raw richness and extinction in the Paleocene megafloral record in the bluffs (Lyson et al. 2019a: suppl.). While the number of fossils collected influences these data, they nonetheless indicate floral turnover at the Pu2/Pu3 boundary. Importantly, we see the first appearace of the angiosperm family Leguminosae (=Fabaceae) outside of Central America (Centeno-Gonzalez et al. 2021) anywhere in the world in the form of both fossil legume pods and leaflets at this stratigraphic level (Lyson et al. 2019a). Legumes would have represented a new, high-protein food source for herbivores such as *T. taoensis* on the early Paleocene landscape. Finally, Lyson et al. (2019a) observed a ~3 °C increase in leaf-estimated MAT at the Pu2/Pu3 boundary. Taken together, these data indicate that floral and faunal turnover (likely migration) driven by temperature increase and the arrival of new plant food sources occurred at the Pu2/Pu3 boundary.

Materials and Methods

Specimens

As noted above, there are many known but undescribed specimens of *Taeniolabis taoensis* from the San Juan Basin that have been collected for well over a century; these reside primarily in collections at AMNH, KU, NMMNH, and UCMP. Simmons (1987) provided a list of referred specimens known at the time and, based on online catalogs, it appears that additional specimens have been discovered since. However, because our study is focused on skull anatomy and because the vast majority of specimens consist of isolated teeth and fragmentary jaws, they are mostly not considered here.

Our study of skull anatomy of *T. taoensis*, assisted by µCT imagery, is therefore largely limited to more detailed description of previously documented specimens — AMNH 16310, AMNH 16321, and UCMP 98083 (listed above in "Introduction"), all from the San Juan Basin — and original description of the new material from the Corral Bluffs study area of the Denver Basin, consisting of four specimens. Synoptic overviews of each of the seven primary specimens in the study sample, to indicate relative completeness and quality of preservation (prior to µCT scanning), are provided below; they are photographically illustrated in Figs. 2 and 3.

DMNH EPV.95284 (DMNH locality 6266, Denver Basin) – Nearly complete cranium missing anterior-most portion of premaxilla (and all of the incisors except for the base of left I2) and small portion of right zygomatic arch; poor surface preservation (Fig. 2a, b); found within displaced concretion at base of a 2–3 m high ridge, suggesting it had not been transported a great distance.

DMNH EPV.134082 (DMNH locality 6500, Denver Basin) – Partial cranium missing dorsal and anterior portions of the snout and anterior parts of the zygomatic arches; poor surface preservation (Fig. 2c, d); found within in situ concretion.

DMNH EPV.136300 (DMNH locality 12111, Denver Basin) – Anterior portion of cranium found within displaced concretion except for tip of snout (anterior portions of premaxillae and both I2s), which was exposed but has better surface preservation than the more posterior parts that were inside the concretion; deformation slight, primarily involving ventral displacement of nasals (Fig. 2e, f); displaced concretion was found at the base of a ~15 m high ridge, and thus may have been transported a great distance.

DMNH EPV.130973 (DMNH locality 7064, Denver Basin) – Moderately well-preserved left dentary missing only apical portions of coronoid process and mandibular condyle (Fig. 2g, h); found within in situ concretion.

AMNH 16321 (locality listed on specimen label as "2 mi. above Ojo Alamo," which is in the Bisti/De-na-zin area, Williamson et al. 2012, San Juan Basin) – Moderately complete but highly fragmented cranium; µCT imaging of this specimen reveals that it is much less complete than in the current, restored specimen (Fig. 3a, b), and also less than illustrated by Broom (1914: pls. XI, XII), who published the only photographs of the specimen. For instance, whereas the photographs in Broom (1914) indicate the presence of a left I2, and the reconstruction includes all four upper incisors (Fig. 3a, b), the µCT scan of the specimen demonstrates that none of the incisors are real.

AMNH 16310 (locality listed on specimen label as "2 mi. above Ojo Alamo," which is in the Bisti/De-na-zin area, Williamson et al. 2012, San Juan Basin) – Very well preserved left dentary missing posterior half of ascending process, including most of coronoid process. The missing portions were (incorrectly) reconstructed in plaster and are illustrated in Fig. 3c, d.

UCMP 98083 (UCMP locality V-70181, San Juan Basin) – Severely deformed and fragmented but nearly complete cranium and both dentaries of juvenile individual (Greenwald 1988: fig. 1).

In full disclosure, a limitation of this study is that it was conducted during the 2020/2021 COVID-19 pandemic, which severely restricted previously planned direct access to original specimens at various museums. AMNH 16310 and AMNH 16321 had been borrowed and UCMP 98083 had been scanned (but not borrowed) prior to the pandemic. However, J. Meng kindly provided photographs of several AMNH cranial and mandibular specimens from the San Juan Basin, most of which had been referred to *T. taoensis* and discussed in the literature previously. These included AMNH 3036, holotype specimen consisting of "right maxilla fragment with M^{1-2} and fragments of skull" (Simmons 1987: 798); AMNH 745 (combined with AMNH 16310 in reconstruction of left dentary by Granger and Simpson 1929: fig. 4A); AMNH 748 and AMNH 968, partial dentaries included in reconstruction of skull by Gregory (1910: fig. 8); and AMNH 27734, nearly complete right dentary. Three of the dentaries (AMNH 745, AMNH 748, AMNH 27734) are illustrated in Fig. 3e–j, with the condylar region of AMNH 27734 highlighted in Fig. 3k–n. We employed the photographs for a few supplementary or confirmatory observations of anatomical structures that were not visible, or poorly visible, on the seven primary specimens in our study sample to which we had direct access (or µCT scans in the case of UCMP 98083). It is also important to note that these photographs revealed that the reconstruction of the cranium of *T. taoensis* by Gregory (1910: fig. 8), reported as being based upon AMNH 3075, is actually based on the holotype specimen, AMNH 3036. AMNH 745, 748, and 968 are from Coal Creek Canyon, AMNH 27734 is from Barrel Spring Arroyo, whereas AMNH 3036 is simply listed as coming from "N.W. New Mexico." Finally, T. Williamson (pers. comm, 11/13/2019) alerted us to the existence of a cranial specimen in the NMMNH collections, NMMNH P-47645, and provided a photograph of it; it is highly concreted, deformed, and fragmented, and does not appear to yield any new anatomical information.

Another limitation of our study is that, even with µCT technology, we were able to discern very few details of the nasal and endocranial cavities because of very low-density contrast between matrix and bone in the available sample. By contrast, the density difference was slightly better in UCMP 98083, which allowed segmentation of the inner ear; its anatomy is detailed below.

Measurements

Linear measurements of the skull and dentition were taken directly from the specimens wherever possible using a Mitutoyo CD-8″ CSX caliper. Other measurements were extracted from digital images using a combination of

Fig. 3 Skull material of *Taeniolabis taoensis* from the San Juan Basin, New Mexico. **a**, **b**, AMNH 16321, fragmentary, incomplete cranium restored with substantial amounts of plaster, in dorsal and ventral views. **c**, **d**, AMNH 16310, left dentary, the posterior portion of which was restored with plaster, in lateral and medial views. **e**, **f**, AMNH 745, left dentary, in lateral and medial views. **g**, **h**, AMNH 748, right dentary in lateral and medial views. **i**, **j**, AMNH 27734, right dentary in lateral and medial views. **k**, **l**, **m**, **n**, enlarged photographs of mandibular condyle of AMNH 27734 (see **i**, **j**) in lateral, medial, dorsal, and posterior views. Scale bar = 5 cm

ImageJ, the 2-dimensional projections in ORS Dragonfly, and Adobe Illustrator, which permitted precise location of measurement endpoints and calculation of linear distances. Angular measurements were extracted from digital photographs using the Measure Tool in Adobe Photoshop or by using semi-transparent protractors overlain on images in PowerPoint (Microsoft Office). Linear and angular measurements of the inner ear were taken with the Amira 3D measurement tool. Total inner ear length and cochlear canal curvature follow Schultz et al. (2017). All linear measurements are in millimeters (mm).

Computed Tomography and Imaging

Data and images for DMNH EPV.95284, DMNH. EPV.130973, DMNH EPV.134082, DMNH EPV.136300, and UCMP 98083 were produced at the High-Resolution X-ray Computed Tomography Facility of the University of Texas at Austin (UTCT). Data and images for AMNH 16310 and AMNH 16321 were produced in the Microscopy and Imaging Facility of the American Museum of Natural History (AMNH) in New York.

16-bit TIFF stacks of raw scan data were processed in ORS Dragonfly (v 4.0, 4.1, 2020.1) with the artifact correction Gradient-Domain-Fusion filter and the contrast enhancing CLAHE (Contrast Limited Adaptive Histogram Equalization) filter. These filtered image stacks were rendered into surface meshes through dynamic threshold segmentation and meshing tools using ORS Dragonfly versions 4.0, 4.1, and 2020.1. Morphological smoothing and closing operations were applied to segmentations prior to meshing. All meshes were decimated by 50%. Meshes were smoothed with the Hamming Window Smoothing method, at 10–15 iterations. UCMP 98083 inner ear images were smoothed with the Laplacian Smoothing method at 15 iterations. Surface meshes were smoothed for final output in ORS Dragonfly 2020.1 and exported in the stereolithography (stl) file type. Final images were rendered in Blender 2.82 with the Cycles render engine and orthographic camera. The inner ear was reconstructed in Amira; label fields were imported into Dragonfly for final processing and imaging.

Basic individual scan parameters, which vary for each specimen and facility, are reported below, as are adjustments made to the datasets.

DMNH EPV.95284 (Fig. 4) – nearly complete cranium first scanned encased in phosphatic concretion at UTCT. Scan parameters: North Star Imaging (NSI) scanner. Fein Focus High Power (FFHP) source, 200 kV, 0.13 mA, aluminum filter, source to object 492.0 mm, source to detector 1316.851 mm, isometric voxel size = 90.9 µm, total slices = 1,927. After mechanical preparation, DMNH EPV.95284 was scanned again at UTCT. Scan parameters: NSI scanner. FFHP source, 180 kV, 0.15 mA, aluminum filter, source to detector 1317.262 mm, isometric voxel size = 82.7 µm, total slices = 1,925. Contrast between bone and sediment matrix was poor in both scans. CLAHE filtering resulted in major striping artifacts in the dataset and failed to homogenize contrast levels across the image stack. Due to the inconsistent contrast levels, window leveling had to be adjusted regularly during segmentation. Similarly, adjusting the Look Up Table (LUT) helped increase contrast levels.

DMNH EPV.134082 (Fig. 5) – posterior portion of cranium scanned at UTCT. Scan parameters: NSI scanner. FFHP source, 200 kV, 0.17 mA, brass filter, source to detector 731.325 mm, isometric voxel size 73.7 µm, total slices = 1,752.

DMNH EPV.136300 (Fig. 6) – anterior portion of cranium scanned at UTCT. Scan parameters: NSI scanner. FFHP source, 160 kV, 0.85 mA, aluminum filter, source to detector 733.22 mm, isometric voxel size = 50.3 µm, total slices = 1,892. Contrast levels were higher and more consistent than in any other scan of DMNH material. Contrast was improved by adjusting LUT and window leveling.

AMNH 16321 (Fig. 7) – fragmentary cranium scanned at AMNH Microscopy and Imaging Facility. Scan parameters: Phoenix scanner. FFHP source, 200 kV, 0.24 mA, copper + copper filters, source to detector 812.661 mm, isometric voxel size = 60.9 µm, total slices = 1,937.

UCMP 98083 (Fig. 8) – nearly complete cranium and both dentaries scanned at UTCT. Scan parameters: NSI scanner. FFHP source, 150 kV, 0.12 mA, aluminum filter, source to detector 730.451 mm, isometric voxel size = 51.7 µm, total slices = 1,888. Contrast between bone and sediment matrix was generally poor and inconsistent across the image stack. Application of CLAHE filter resulted in striping artifacts and exacerbated inhomogeneity of the dataset. LUT and window leveling required regular adjusting.

DMNH EPV.130973 (Fig. 9a–c) – nearly complete left dentary scanned at UTCT. Scan parameters: NSI scanner. FFHP source, 140 kV, 0.25 mA, aluminum filter, source to detector 1317.167 mm, isometric voxel size = 62.5 µm, total slices = 1,941.

AMNH 16310 (Fig. 9d–f) – left dentary missing posterior portion scanned at AMNH Microscopy and Imaging Facility. Scan parameters: Phoenix scanner. FFHP source, 200 kV, 0.24 mA, copper filter, source to detector 812.661 mm, isometric voxel size = 60 µm, total slices = 1,727.

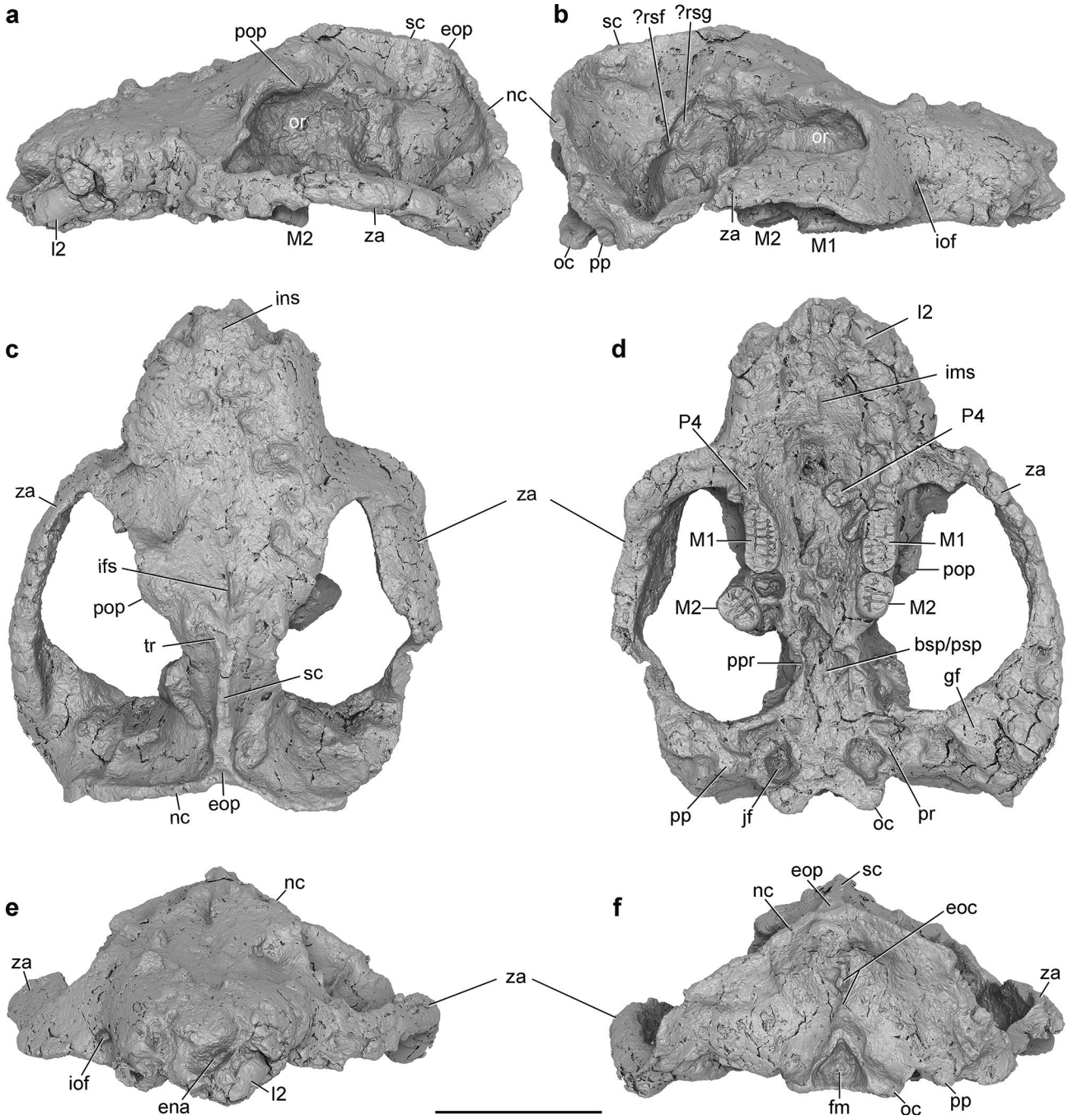

Fig. 4 Rendering of 3D virtual model of nearly complete cranium of *Taeniolabis taoensis*, DMNH EPV.95284, based on μCT data, in **a**, left lateral; **b**, right lateral; **c**, dorsal; **d**, ventral; **e**, anterior; and **f**, posterior views. Abbreviations: bsp/psp, basisphenoid/presphenoid; ena, external nasal aperture; eoc, external occipital crest; eop, external occipital protuberance; fm, foramen magnum; gf, glenoid fossa; I2, upper second incisor; ifs, interfrontal suture; ims, intermaxillary suture; ins, internasal suture; iof, infraorbital foramen; jf, jugular fossa; M1, upper first molar; M2, upper second molar; nc, nuchal (=lambdoidal) crest; oc, occipital condyle; or, orbit; P4, upper fourth premolar; pop, postorbital process; pp, paroccipital process; ppr, pterygopalatine ridge; pr, promontorium; ?rsf, possible foramen for ramus superior of stapedial artery; ?rsg, possible groove for ramus superior of stapedial artery; sc, sagittal crest; tr, temporal ridge; za, zygomatic arch. Scale bar = 5 cm

Institutional Abbreviations

AMNH, American Museum of Natural History, New York, New York; CCM, Carter County Museum, Ekalaka, Montana; DMNH, Denver Museum of Nature & Science, Denver, Colorado; IRSNB M, Royal Belgian Institute of Natural Sciences, Brussels, Belgium; IVPP, Institute of Vertebrate Paleontology and Paleoanthropology, Beijing, China; KU, Biodiversity Institute & Natural History Museum, University of Kansas, Lawrence, Kansas; NMMNH, New Mexico Museum of Natural History and Science, Albuquerque, New Mexico; PSS-MAE, Paleontological and Stratigraphic Section of the Geological Institute, Mongolian Academy of Sciences, Ulaan Baatar, Mongolia (Mongolian–American Museum of Natural History Expedition); UALVP, University of Alberta Laboratory of Vertebrate Paleontology, Edmonton, Alberta; UCMP, University of California Museum of Paleontology, Berkeley, California; UTCT, High-Resolution X-ray Computed Tomography Facility, University of Texas, Austin, Texas; UMVP, University of Minnesota Vertebrate Paleontology collections, Minneapolis, Minnesota; V.J., Museum of the Geological Service, Lisbon, Portugal; YPM VPPU, Yale Peabody Museum of Natural History, Vertebrate Paleontology Princeton University Collection, New Haven, Connecticut; ZPal, Institute of Palaeobiology, Academy of Sciences, Warsaw, Poland.

Anatomical Abbreviations

aI3, alveolus for upper third incisor; am, ampulla; ap, apex; aP4, alveolus for upper fourth premolar; asc, anterior semicircular canal; bo, basioccipital; bof, basioccipital fossa; bor, basioccipital ridge; bs, broken surface; bsp/psp, basisphenoid/presphenoid; bzr, broken zygomatic root; cc, crus commune; ci, crista interfenestralis; cn, cochlear nerve; co, cochlear canal; cp, coronoid process; cri, canal for ramus inferior; crp, crista parotica; di, deciduous lower incisor; dI2, deciduous upper second incisor; ecc, endocranial cavity; ena, external nasal aperture; eo, exoccipital; eoc, external occipital crest; eop, external occipital protuberance; fips, foramen for inferior petrosal sinus; fj, facet for jugal; fm, foramen magnum; fmV, foramen for mandibular division of trigeminal nerve; fnc, floor of nasal cavity; fps, frontal-parietal suture; fr, frontal; fv, fenestra vestibuli; gf, glenoid fossa; i, lower incisor; I2, upper second incisor; I3, upper third incisor; if, incisive foramen; ifs, interfrontal suture; imr1, intramasseteric ridge 1; imr2, intramasseteric ridge 2; ims, intermaxillary suture; inp, internarial process; ins, internasal suture; iof, infraorbital foramen; ipms, interpremaxillary suture; ips, interpalatine suture; izr, intermediate zygomatic ridge; j, jugal; jf, jugular fossa; lf, lateral flange; lsc, lateral semicircular canal; m1, lower first molar; M1, upper first molar; m2, lower second molar; M2, upper second molar; mco, mandibular condyle; mcr, masseteric crest; mf, mental foramen; mfos, masseteric fossa; mfov, masseteric fovea; ml, masseteric line; mn, mandibular notch; ms, mandibular symphysis; mss, maxillary-squamosal suture; mx, maxilla; n, nasal; nc, nuchal (= lambdoidal) crest; nf, nasal foramen or foramina; oc, occipital condyle; oml, origin of masseter lateralis; omspa, origin of masseter superficialis pars anterior; omspp, origin of masseter superficialis pars posterior; on, odontoid notch; or, orbit; otf, orbitotemporal fenestra; p4, lower fourth premolar; P4, upper fourth premolar; pa, parietal; pf, pterygoid fossa; plf, perilymphatic foramen; plg, perilymphatic groove; pmr, premaxillary ridge; pms, premaxillary-maxillary suture; pmx, premaxilla; pop, postorbital process; pp, paroccipital process; ppr, pterygopalatine ridge; pr, promontorium; ps, pterygoid shelf; psc, posterior semicircular canal; ptf, posttemporal foramen; ?rsf, possible foramen for ramus superior of stapedial artery; ?rsg, possible groove for ramus superior of stapedial artery; sc, sagittal crest; ses, supraoccipital-exoccipital suture; sf, stapedius fossa; so, supraoccipital; tg, temporal groove; tr, temporal ridge; vo, vomer or suture for vomer; vs, vestibule; za, zygomatic arch; zpm, zygomatic process of maxilla; zps, zygomatic process of squamosal.

Systematic Paleontology

MAMMALIA Linnaeus, 1758
ALLOTHERIA Marsh, 1880
MULTITUBERCULATA Cope, 1884a
CIMOLODONTA McKenna, 1975
TAENIOLABIDOIDEA Sloan and Van Valen, 1965
TAENIOLABIDIDAE Granger and Simpson, 1929

Williamson et al. (2016: 204) included only two genera in this family, *Taeniolabis* and a new genus, *Kimbetopsalis*, which was erected to receive a new species, *K. simmonsae*. The authors regarded *K. simmonsae* to be "the basal-most member of Taeniolabididae and.... a plausible progenitor for *T. taoensis*, which first appeared in the San Juan Basin within the next 200 Kyr." Kondrashov and Lucas (2015: 133), however, opined that *K. simmonsae* was not sufficiently distinct from *Taeniolabis* to establish a new genus, stating that "the size and ratio differences are minor." Whereas we concur that the differences in overall size and cusp numbers are not great, we provisionally retain the species in *Kimbetopsalis* pending analysis of newly discovered taeniolabidid specimens from the Denver Basin that do not appear to be referable to *T. taoensis*.

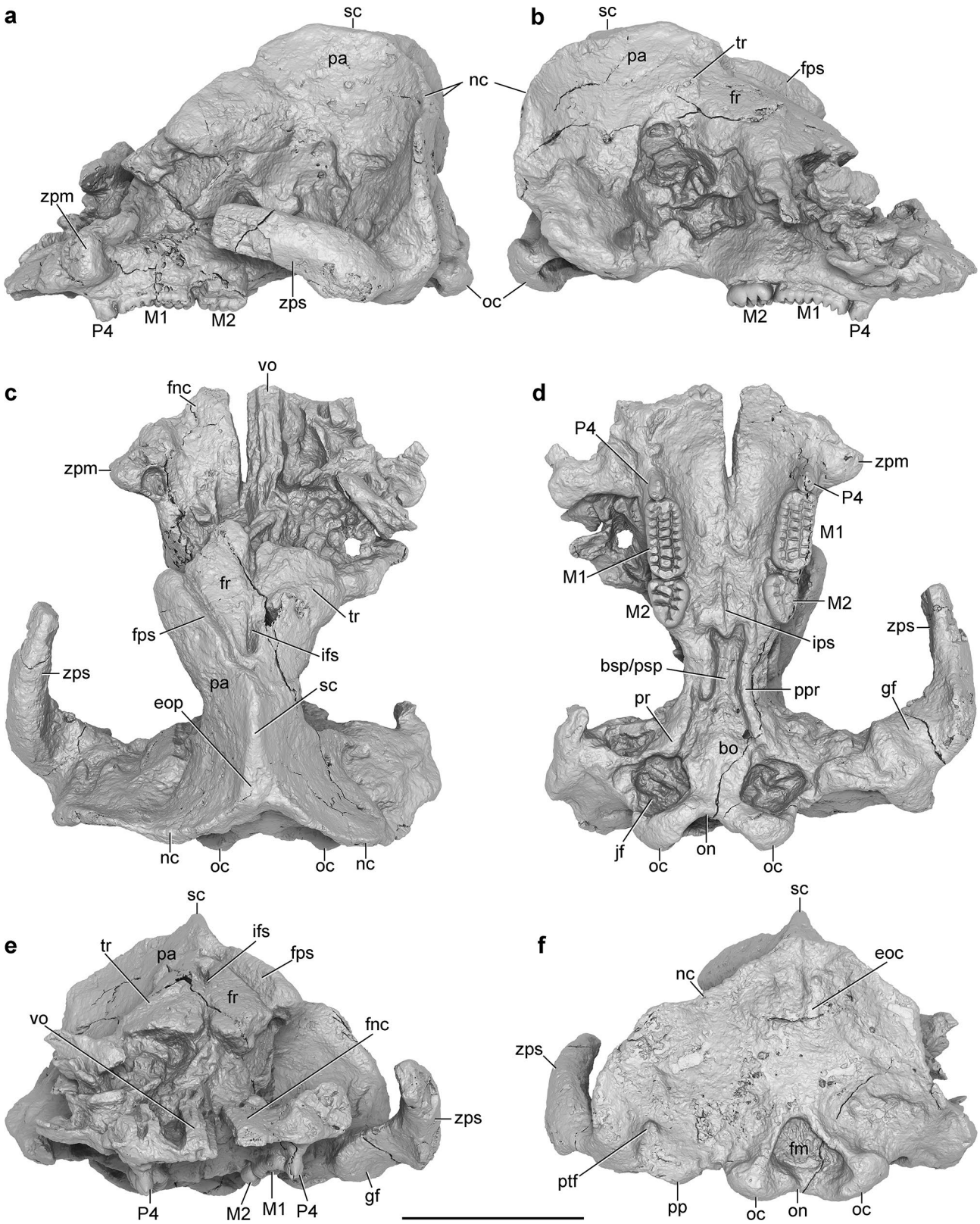

TAENIOLABIS Cope, 1882b

The alpha taxonomic history of the genus *Taeniolabis*, erected by Cope (1882b), is somewhat complicated but was summarized by Simmons (1986, 1987), who synonymized several species with *T. taoensis*. Simmons, in addition to naming a new species, *T. lamberti*, concluded that there was

◂**Fig. 5** Rendering of 3D virtual model of posterior portion of cranium of *Taeniolabis taoensis*, DMNH EPV.134082, based on μCT data, in **a**, left lateral; **b**, right lateral; **c**, dorsal; **d**, ventral; **e**, anterior; and **f**, posterior views. Abbreviations: bo, basioccipital; bsp/psp, basisphenoid/presphenoid; eoc, external occipital crest; eop, external occipital protuberance; fm, foramen magnum; fnc, floor of nasal cavity; fps, frontal-parietal suture; fr, frontal; gf, glenoid fossa; ifs, interfrontal suture; ips, interpalatine suture; jf, jugular fossa; M1, upper first molar; M2, upper second molar; nc, nuchal crest; oc, occipital condyle; on, odontoid notch; P4, upper fourth premolar; pa, parietal; pp, paroccipital process; ppr, pterygopalatine ridge; ptf, posttemporal foramen; sc, sagittal crest; tr, temporal ridge; vo, vomer or suture for vomer; zpm, zygomatic process of maxilla; zps, zygomatic process of squamosal. Scale bar = 5 cm

only one other valid species, *T. taoensis*, a species that had earlier been included in *Polymastodon*, which was explicitly recognized as the junior synonym of *Taeniolabis* by Matthew and Granger (1925).

Type Species *Taeniolabis taoensis* (Cope, 1882c)

Included Species *T. taoensis* (Cope, 1882c) and *T. lamberti* Simmons (1987). If *Kimbetopsalis* is a junior synonym of *Taeniolabis*, as argued by Kondrashov and Lucas (2015), then there is possibly a third species of *Taeniolabis*, *T. simmonsae*.

Diagnosis The most recent diagnosis of *Taeniolabis* was provided by Simmons (1987: 797) and was restricted to dental characters, as follows: "Dimensions of i1, I2, and M2/m2 greater than in any other multituberculate. Seven or more cusps in the labial cusp row and six or more cusps in the lingual cusp row of m1. Four or more cusps in lingual cusp row of m2. Nine or more cusps in labial and lingual cusp rows of M1. Four or more cusps in medial cusp row of M2. Ratio of tooth length p4/m1 less than 0.40." With the cranial material described herein, and because other taeniolabidoid taxa are also represented by cranial material, we are in the position to revise the diagnosis for the genus more comprehensively. We defer doing so, however, until we have described and analyzed new taeniolabidid skull material from the Denver Formation that we currently regard as not referable to *T. taoensis* (Krause et al. in prep.) and until we can examine the many dental specimens of *T. taoensis* housed in other museums (to which access is currently restricted because of the pandemic).

TAENIOLABIS TAOENSIS (Cope, 1882c)

Holotype Specimen AMNH 3036, right maxillary fragment with M1–2 and fragments of skull (see clarification in Simmons 1987 regarding composition of holotype). Maxillary fragment illustrated by Cope (1884a: fig. 3e, b: pl. XXIIIc, fig. 6). Cranial fragments illustrated by Gregory (1910: fig. 8) but mistakenly labeled as AMNH 3075.

Referred Specimens DMNH EPV.95284, nearly complete cranium (Figs. 2a, b, and 4); DMNH EPV.134082, posterior portion of cranium (Figs. 2c, d, and 5); DMNH EPV.136300, anterior portion of cranium (Figs. 2e, f, and 6); and DMNH EPV.130973, nearly complete left dentary (Figs. 2g, h, and 9a–c). Dimensions (Tables 2 and 3) and cusp formulae (Table 4) of the molars in these specimens fall within the ranges of variation for the San Juan Basin specimens measured and counted by Simmons (1987), the only exception being M1 lengths in DMNH EPV.95284 and DMNH EPV.136300, which fall less than 1 mm below the rather narrow range of the San Juan Basin M1 lengths. We provisionally take these measurements and counts as providing confirmatory evidence for assignment of the DMNH specimens to *T. taoensis*.

Diagnosis "P4/p4, M1/m1, and length of lower tooth row larger than in any other multituberculate, including *T. lamberti*.... Anterior edge of coronoid process lies labial to posterior half of m1" (Simmons 1987: 799). As for the diagnosis of the genus, we defer revising the diagnosis of *T. taoensis* until we have more fully assessed new taeniolabidid material from the Denver Formation (Krause et al. in prep.).

Description

Cranium

The cranial material from the Corral Bluffs study area is the most complete for *Taeniolabis taoensis*. This material, coupled with that previously described from the San Juan Basin (without the aid of μCT technology), allows us to provide descriptions of most elements in more detail than possible heretofore. This is preceded by an overview of cranial size and shape and how the latter differs from those in previous reconstructions.

Cranial Size and Body Mass Estimates Various measurements of the available crania of *T. taoensis* are provided in Table 5. Employing overall cranial size (geometric mean of maximum cranial length and width) as seemingly the most practical metric for estimating body mass in multituberculates (Wilson et al. 2012; Lyson et al. 2019a), *T. taoensis* was estimated by Lyson et al. (2019a) to have had a body mass of 34.0 kg (95% confidence interval = 20.8–55.6 kg). The measurements and resulting estimate were based on DMNH EPV.95284, the most complete available cranium. We revise that estimate here because of the discovery of DMNH EPV.136300 (Fig. 6), which demonstrated for the first time that the premaxilla extended farther anteriorly (approximately 7 mm) in *T. taoensis* than previously realized, and thus that the

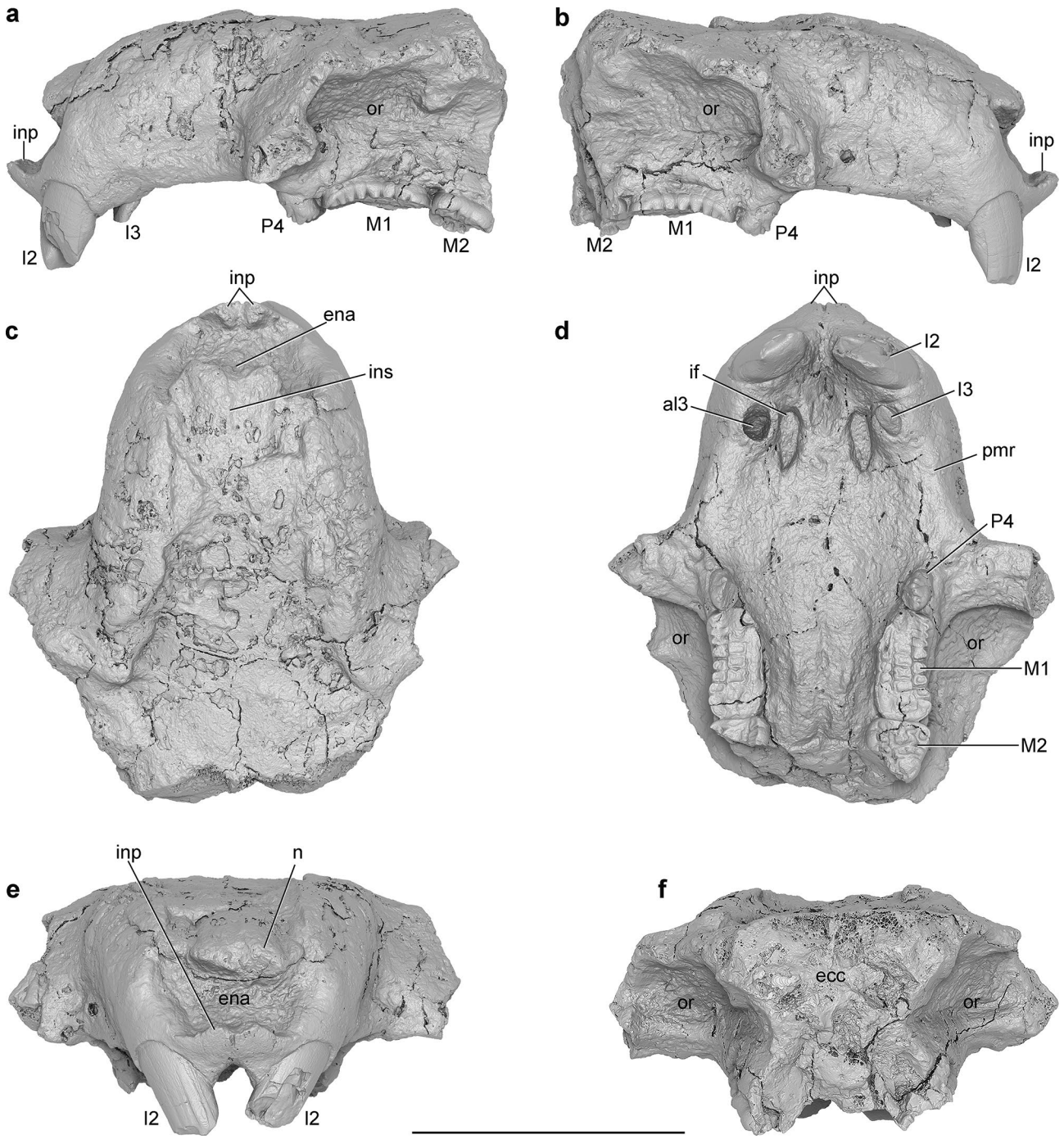

Fig. 6 Rendering of 3D virtual model of anterior portion of cranium of *Taeniolabis taoensis*, DMNH EPV.136300, based on µCT data, in **a**, left lateral; **b**, right lateral; **c**, dorsal; **d**, ventral; **e**, anterior; and **f**, posterior views. Abbreviations: aI3, alveolus for upper third incisor; ecc, endocranial cavity; ena, external nasal aperture; I2, upper second incisor; I3, upper third incisor; if, incisive foramen; inp, internarial process; ins, internasal suture; M1, upper first molar; M2, upper second molar; n, nasal; or, orbit; P4, upper fourth premolar; pmr, premaxillary ridge. Scale bar = 5 cm

condylobasal length in DMNH EPV.95284 (Fig. 4) was underestimated. Revised (only condylobasal length) and other measurements for DMNH EPV.95284 are provided in Table 5, as are original measurements for AMNH 16321 and UCMP 98083, the only other two specimens for which condylobasal length and bizygomatic breadth can be directly measured or calculated. Using the same regression equations as employed by Lyson et al. (2019a; see Krause et al.

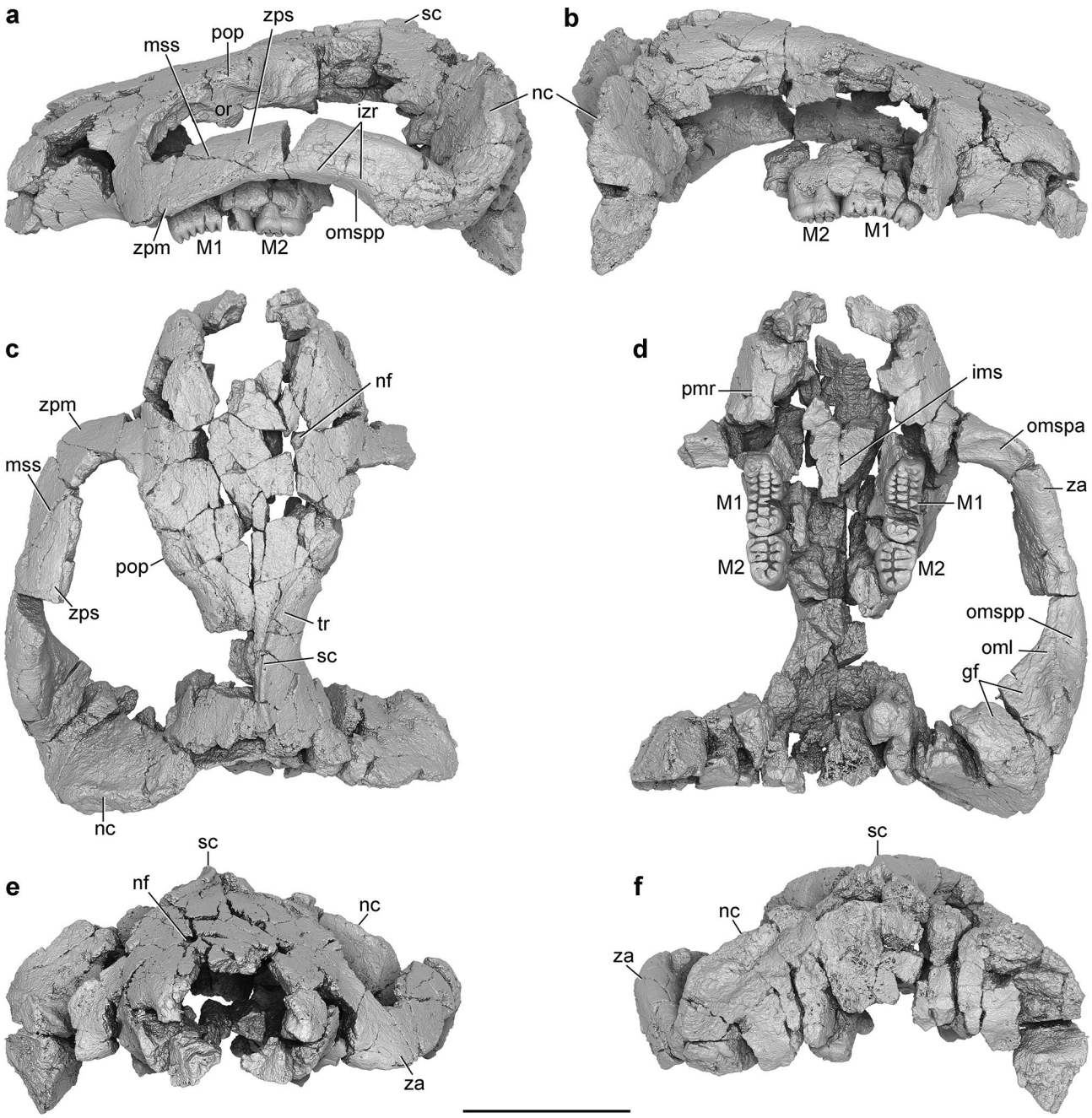

Fig. 7 Rendering of 3D virtual model of fragmentary cranium of *Taeniolabis taoensis*, AMNH 16321, based on μCT data, in **a**, left lateral; **b**, right lateral; **c**, dorsal; **d**, ventral; **e**, anterior; and **f**, posterior views. Abbreviations: gf, glenoid fossa; ims, intermaxillary suture; izr, intermediate zygomatic ridge; M1, upper first molar; M2, upper second molar; mss, maxillary-squamosal suture; nc, nuchal (=lambdoidal) crest; nf, nasal foramen; oml, origin of masseter lateralis; omspa, origin of masseter superficialis pars anterior; omspp, origin of masseter superficialis pars posterior; or, orbit; pmr, premaxillary ridge; pop, postorbital process; sc, sagittal crest; tr, temporal ridge; za, zygomatic arch; zpm, zygomatic process of maxilla; zps, zygomatic process of squamosal. Scale bar = 5 cm

2014a for equations and comparative data set of over 400 extant species belonging to 20 orders of therian mammals), the revised body mass estimate based on DMNH EPV.95284 is 36.6 kg (cranial size = 153.3 mm; 95% confidence interval = 22.4–59.9 kg). The body mass estimate based on cranial size of AMNH 16321 is slightly greater (39.7 kg; cranial size = 157.0 mm; 95% confidence interval = 24.2–65.1 kg), whereas that based on cranial size of UCMP 98083, the juvenile skull, is understandably much less (5.3 kg; cranial size = 87.2 mm; 95% confidence interval = 3.3–8.4 kg).

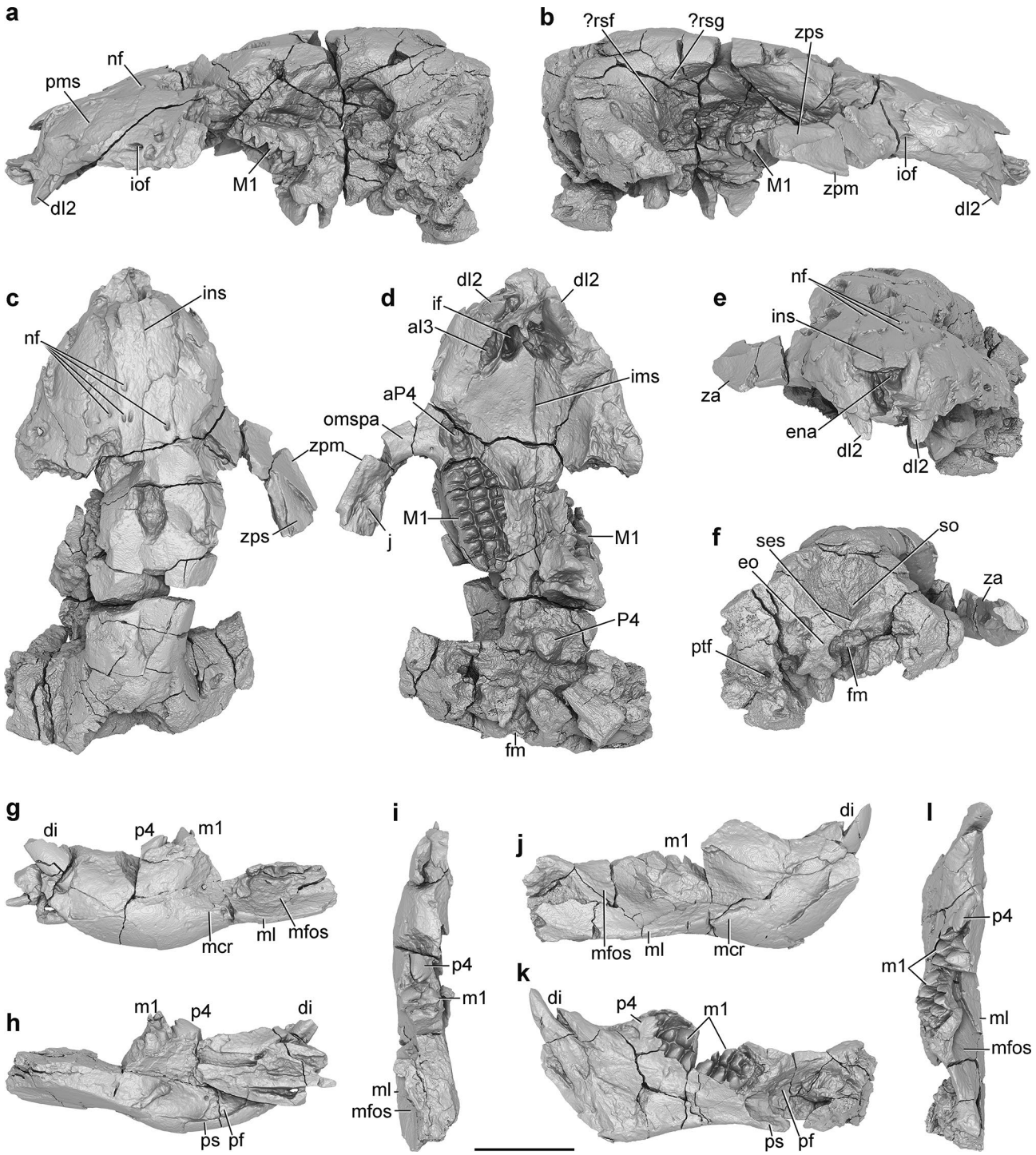

Fig. 8 Rendering of 3D virtual model of nearly complete skull of juvenile *Taeniolabis taoensis*, UCMP 98083, based on µCT data. Cranium in **a**, left lateral; **b**, right lateral; **c**, dorsal; **d**, ventral; **e**, anterior; and **f**, posterior views. Left dentary in **g**, lateral; **h**, medial; and **i**, dorsal (occlusal) views. Right dentary in **j**, lateral; **k**, medial; and **l**, dorsal (occlusal) views. Abbreviations: aI3, alveolus for upper third incisor; aP4, alveolus for upper fourth premolar; di, deciduous lower incisor; dI2, deciduous upper second incisor; ena, external nasal aperture; eo, exoccipital; fm, foramen magnum; if, incisive foramen; ims, intermaxillary suture; ins, internasal suture; iof, infraorbital foramen; j, jugal; m1, lower first molar; M1, upper first molar; mcr, masseteric crest; mfos, masseteric fossa; ml, masseteric line; nf, nasal foramina; omspa, origin of masseter superficialis pars anterior; p4, lower fourth premolar; P4, upper fourth premolar; pf, pterygoid fossa; pms, premaxillary-maxillary suture; ps, pterygoid shelf; ptf, posttemporal foramen; ?rsf, possible foramen for ramus superior of stapedial artery; ?rsg, possible groove for ramus superior of stapedial artery; ses, supraoccipital-exoccipital suture; so, supraoccipital; za, zygomatic arch; zpm, zygomatic process of maxilla; zps, zygomatic process of squamosal. Scale bar = 2 cm

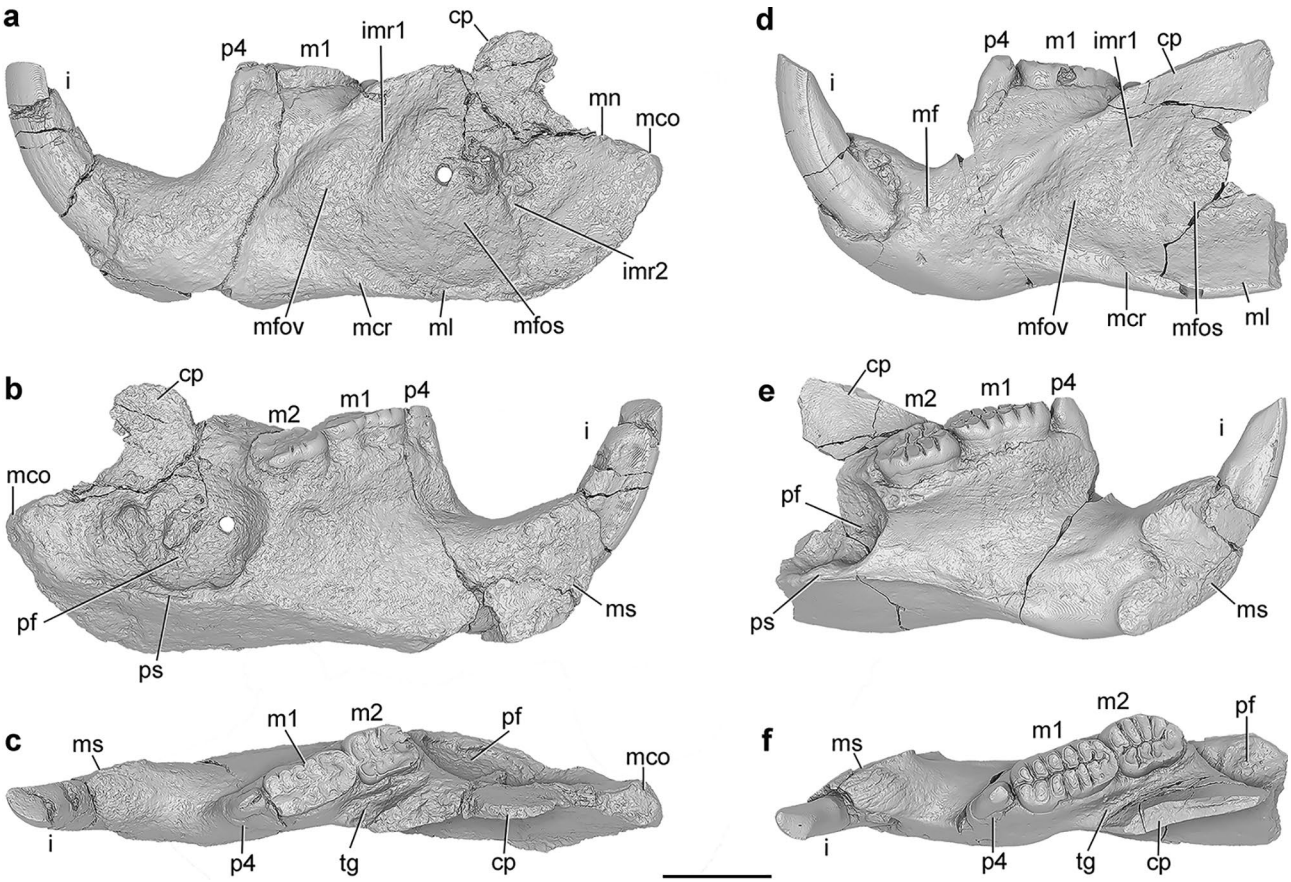

Fig. 9 Rendering of 3D virtual model of left dentaries of *Taeniolabis taoensis*, based on µCT data. **a**–**c**, DMNH EPV.130973; **d**–**f**, AMNH 16310. **a**, **d**, lateral views; **b**, **e**, medial views; **c**, **f**, dorsal (occlusal) views. Abbreviations: cp, coronoid process (incomplete in both specimens); i, lower incisor; imr1, intramasseteric ridge 1; imr2, intramasseteric ridge 2; m1, lower first molar; m2, lower second molar; mco, mandibular condyle; mcr, masseteric crest; mf, mental foramen; mfos, masseteric fossa; mfov, masseteric fovea; ml, masseteric line; mn, mandibular notch; ms, mandibular symphysis; p4, lower fourth premolar; pf, pterygoid fossa; ps, pterygoid shelf; tg, temporal groove. Round hole in masseteric fossa of **a** and pterygoid fossa in **b** is a preparation artifact. Scale bar = 2 cm

Table 2 Measurements (in mm) of upper dentition in study sample of *Taeniolabis taoensis* compared to those in study sample of Simmons (1987). Measurements of UCMP 98083 from Greenwald (1988). All lengths (L) are mesiodistal; all widths (W) are buccolingual. Incisor measurements taken at or near alveolus. Left and right sides designated as (l) and (r), respectively

		I2L	I2W	I3L	I3W	P4L	P4W	M1L	M1W	M2L	M2W
DMNH EPV.95284 (l)		—	—	—	—	—	—	21.4	10.9	13.6	11.4
DMNH EPV.95284 (r)		—	—	—	—	—	—	21.5	11.0	14.3	11.2
DMNH EPV.134082 (l)		—	—	—	—	6.8	5.2	22.8	11.4	14.4	11.8
DMNH EPV.134082 (r)		—	—	—	—	6.5	5.1	22.3	11.1	14.0	11.8
DMNH EPV.136300 (l)		11.5	8.1	5.9	3.9	7.7	5.5	21.1	11.3	—	12.6
DMNH EPV.136300 (r)		11.8	8.2	—	—	7.9	5.6	21.2	10.9	—	—
AMNH 16321 (l)		—	—	—	—	—	—	24.2	11.3	14.5	12.4
AMNH 16321 (r)		—	—	—	—	—	—	23.6	11.0	14.9	12.1
UCMP 98083 (r)		—	—	—	—	7.2	5.6	22.8	11.5*	—	—
Simmons (1987)	N	0	0	0	0	5	5	22	22	11	11
	OR	—	—	—	—	6.5–7.7	5.0–5.7	21.9–24.4	10.8–12.1	12.3–16.0	11.2–12.8
	$\bar{x}$	—	—	—	—	7.1	5.3	23.0	11.6	14.4	12.0

*Estimated measurement

Table 3 Measurements (in mm) of lower dentition in study sample of *Taeniolabis taoensis* compared to those in study sample of Simmons (1987). Measurements of UCMP 98083 from Greenwald (1988). All lengths (L) are mesiodistal; all widths (W) are buccolingual. Incisor measurements taken at or near alveolus. Left and right sides designated as (l) and (r), respectively

		i1L	i1W	p4L	p4W	m1L	m1W	m2L	m2W
DMNH EPV.130973		12.4	8.9	6.9	4.1	19.1	9.4	14.5	10.8
AMNH 16310		10.8	6.9	6.7	4.5	20.9	9.7	15.0	11.2
UCMP 98083 (l)		—	—	6.9*	—	—	—	—	—
UCMP 98083 (r)		—	—	—	4.7*	20.5*	10.4*	—	—
Simmons (1987)	N	0	0	17	17	35	35	40	40
	OR	—	—	5.9–7.4	3.9–5.5	18.7–21.4	9.4–11.4	12.5–16.6	9.9–13.5
	$\bar{x}$	—	—	6.6	4.7	19.8	10.4	14.1	11.5

*Estimated measurement

Cranial Shape Based on AMNH 3036, a partial cranium consisting of a few posterior fragments, the cranium of *T. taoensis* was originally reconstructed by W. D. Matthew (in Gregory 1910: fig. 8, who apparently mislabeled this specimen in the caption as AMNH 3075) as slender and elongate, with a narrow, pointed snout in dorsal view and a strongly arched (concave ventrally) diastema between the incisors and cheekteeth, a low braincase, and a distinct convexity above the orbit in side view. The discovery of AMNH 16321 resulted in major revisions to the dorsal outline and later reconstructions by Broom (1914: figs. 6, 8), Simpson (1926: fig. 2), and Granger and Simpson (1929: figs. 4–6) more accurately depicted a much shorter, broader cranium (almost as wide as long), with widely flaring zygomatic arches that, anteriorly, project almost directly laterally, and also a short, blunt snout. In lateral view, the cranium was reconstructed by these later authors with a large, relatively flat diastema, a very deep, strongly arched (convex dorsally, concave ventrally) zygomatic arch, and a strongly domed, relatively high braincase. The cranial reconstructions of Granger and Simpson (1929) became the standard depiction for *T. taoensis* and were frequently duplicated or closely followed in later works (e.g., Simpson 1935: fig. 16; Matthew 1937: figs. 71–73; Simpson 1937b: fig. 3; Romer 1966: fig. 309A; Sloan 1979: fig. 4, 1981: text-fig. 6.14; Krause 1982b: fig. 1, 1986: fig. 4; Kermack and Kermack 1984: fig. 8.13; Carlson and Krause 1985: fig. 1; Savage and Long 1986; Kielan-Jaworowska and Hurum 1997: figs. 10C, 11C; Kielan-Jaworowska et al. 2004: figs. 8.39I, 8.40C; Rose 2006: fig. 4.8; Weil and Krause 2008: fig. 2.2A; Rougier et al. 2016: fig. 29; Adams et al. 2019: fig. 1d; Wible et al. 2019: figs. 21C, 22C, 23C). The largest change to the reconstructions of Granger and Simpson (1929) was made to the lateral view by Sloan (1979, 1981; followed by Wible et al. 2019: fig. 21C), who concluded that the orbit was larger and more posteriorly situated, with the anterior part of the orbit occupied by a portion of the masseter muscle. Furthermore, Sloan (1979, 1981), unlike Broom (1914), Simpson (1926), and Granger and Simpson (1929), did not include a laterally visible jugal bearing a dorsally projecting postorbital process (marking the posterior limit of the orbit).

Table 4 Cusp formulae of upper and lower molars in study sample of *Taeniolabis taoensis* compared to those in study sample of Simmons (1987). Left and right sides designated as (l) and (r), respectively

	M1	M2	m1	m2
DMNH EPV.95284 (l)	9?:9?:9?	1:4:6	—	—
DMNH EPV.95284 (r)	–:–:9?	1?:4?:6?	—	—
DMNH EPV.134082 (l)	8:9:10	–:–:5	—	—
DMNH EPV.134082 (r)	8:9:10	1:4:5	—	—
DMNH EPV.136300 (l)	–:–:–	1:4:–	—	—
DMNH EPV.136300 (r)	9:–:–	1?:–:–	—	—
AMNH 16321 (l)	8:9:9	1:4:5	—	—
AMNH 16321 (r)	8:9:9	1:4:5	—	—
UCMP 98083 (l)	—	—	—	—
UCMP 98083 (r)	8:9:–	—	7?:6?	—
DMNH EPV.130973	—	—	7?:6?	4?:4?
AMNH 16310	—	—	7:6	4:4
Simmons (1987)	8–11:9–10:9–11[a]	1:4–5:4–6	7–8:6–7	4–6:4–6

[a]Williamson et al. (2016: Table 1) list 12 maximum cusps in the medial row

The new material from Corral Bluffs reveals that several adjustments need to be made to the cranial reconstructions of Granger and Simpson (1929), who depicted the cranium in dorsal (fig. 5A), ventral (fig. 6), lateral (fig. 4), and posterior (fig. 5B) views; neither they nor any other workers illustrated an anterior view. Revised reconstructions of the cranium of *T. taoensis* in all five standard views (dorsal, ventral, lateral, anterior, and posterior) are provided in Fig. 10a–e.

Dorsal View: (1) the premaxillae, with their anterodorsally projecting internarial processes, extend considerably

Table 5 Measurements (in mm) of crania in study sample of *Taeniolabis taoensis*. Because of deformation, breakage, and/or poor surface preservation of all of the crania in the sample, all cranial measurements over 50 mm are rounded to the nearest millimeter and must be regarded as estimates only. Left and right sides designated as (l) and (r), respectively

	DMNH EPV.95284	DMNH EPV.134082	DMNH EPV.136300	AMNH 16321	UCMP 98083
Condylobasal length[a]	161	—	—	159	95.8
Bi-zygomatic breadth[b]	146	—	—	155	79.4
Occipital height[c]	54	64	—	—	—
Snout length[d]	68.0	—	59.2	64.4	35.4
Cheektooth row length[e]	—	41.9 (r)	—	46.0 (l); 45.2 (r)	—
Depth of zygomatic arch	21.3 (r)	—	—	20.8 (l)	17.7 (r)
Width of zygomatic arch	8.6 (r)	—	—	9.4 (l)	—
Length of glenoid fossa	—	24.7 (l)	—	27.7 (l)	—
Width of glenoid fossa	—	23.7 (l)	—	25.2 (l)	—
Diastema between L and R I2 aveoli	—	—	9.4	—	—
Diastema between I2 and I3	—	—	3.7 (l); 4.8 (r)	—	—
Diastema between I3 and P4	—	—	25.0 (l); 24.4 (r)	23.6 (l); 23.4* (r)	—
Minimum width between M1s	24.3	23.4	20.5	—	—
Foramen magnum height	13.3	15.4	—	—	—
Foramen magnum width	15.7	19.1	—	—	—

*Estimated because of incompleteness

[a]Measured as anteroposterior distance between aboral margin of occipital condyles and prosthion

[b]Measured as maximum mediolateral distance between lateral margins of zygomatic arches (doubled if measurable on only one side)

[c]Measured as dorsoventral distance from basion (midline of ventral margin of foramen magnum) to external occipital protuberance (=inion); intersection of left and right nuchal crests with sagittal crest)

[d]Measured as anteroposterior distance between anterior margin of orbit sensu lato (i.e., including orbital pocket) and prosthion

[e]Measured from mesial margin of P4 to distal margin of M2

farther anteriorly than previously known, thus completely obscuring observation of the upper central incisors (I2s) in this view and making the front of the snout more pointed than previously recognized (DMNH EPV.136300, Fig. 6c); (2) the angle between the snout and the root of the zygomatic arch is slightly more accentuated (DMNH EPV.136300, Fig. 6c); (3) the orbit is positioned farther posteriorly than reconstructed by Granger and Simpson (1929) but more anteriorly than reconstructed by Sloan (1981); see also "Lateral View" below; (4) the size (height) of the sagittal and nuchal (=lambdoidal) crests are taller and more ridge-like than previously estimated (DMNH EPV.95284, Fig. 4c; DMNH EPV.134082, Fig. 5c); (5) the cranial vault is not evenly rounded but instead ends in a distinct peak where the sagittal and nuchal crests intersect (external occipital protuberance), which is farther posterior than previously reconstructed (DMNH EPV.95284, Fig. 4c); and (6) the occipital condyles are not as anteriorly positioned relative to the nuchal crests as previously reconstructed (DMNH EPV.95284, Fig. 4b, d; DMNH EPV.134082, Fig. 5a–d).

Ventral View: (1) the premaxillae extend farther anteriorly, beyond the level of the upper central incisors (DMNH EPV.136300, Figs. 6d and 11); (2) the I3s are preserved in situ for the first time (DMNH EPV.136300, left side, Figs. 6d and 11); (3) the incisive foramina are slightly smaller and slightly more lateral, closer to the alveoli of I3 (DMNH EPV.136300, Figs. 6d and 11); (4) the maxillary portion of the palate is not as strongly domed (DMNH EPV.95284, Fig. 4d; DMNH EPV.136300, Figs. 6d and 11) as described by Granger and Simpson (1929); (5) the posterior end of the palate ends farther anteriorly, roughly at the level of the middle (DMNH EPV.95284, Fig. 4d) or posterior end (DMNH EPV.134082, Fig. 5d) of M2, rather than well posterior to M2, and has a more bulbous, midline, posterior projection; (6) the sutures between the premaxillae and the maxillae on the palate are seen for the first time in DMNH EPV.136300 (Figs. 6d and 11); (7) the sutures between the maxillae and the palatines can be discerned in DMNH EPV.134082 (Fig. 5d) for the first time (these sutures were not rendered by Granger and Simpson 1929: fig. 6, but were added by Kielan-Jaworowska and Hurum 1997: fig. 11C, incorrectly); and (8) details of the mesocranium and basicranium are revealed for the first time in DMNH EPV.95284 (Figs. 4d and 14b), DMNH EPV.134082 (Figs. 5d, 14c), and UCMP 98083 (Figs. 8d, 14d).

Lateral View: (1) the premaxillae, with their anterodorsally projecting internarial processes, extend farther anteriorly than previously known (DMNH EPV.136300, Fig. 6a,

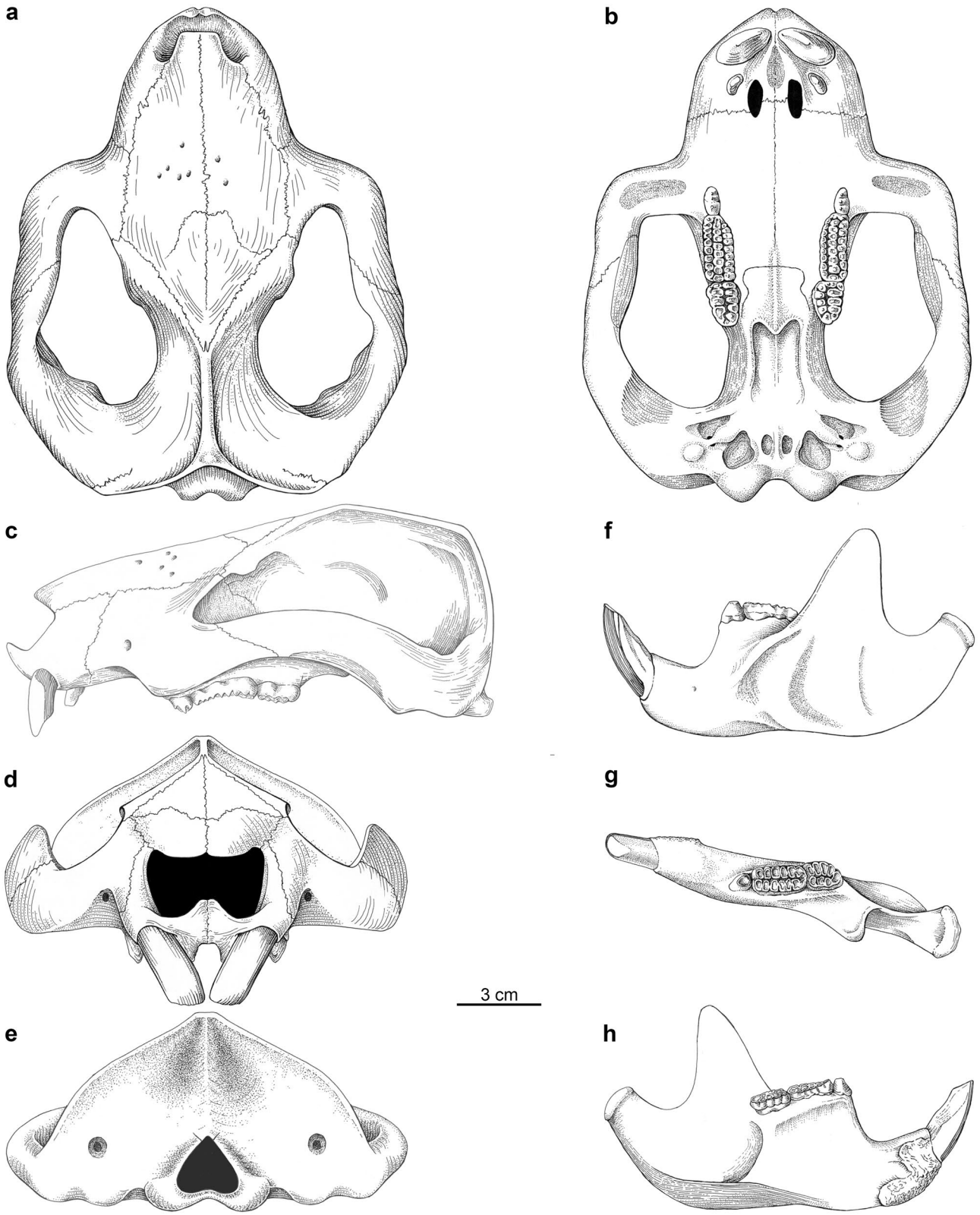

Fig. 10 Reconstruction of the skull of *Taeniolabis taoensis*. Cranium (based on DMNH EPV.95284, DMNH EPV.134082, DMNH EPV.136300, AMNH 16321, and UCMP 98083) in **a**, dorsal; **b**, ventral; **c**, left lateral; **d**, anterior; and **e**, posterior views. Left dentary (based on DMNH EPV.130973, AMNH 745, AMNH 748, AMNH 968, AMNH 16310, AMNH 27734, and UCMP 98083) in **f**, lateral; **g**, dorsal; and **h**, medial views. Scale bar = 3 cm

b); (2) the I3s are preserved in situ for the first time (DMNH EPV.136300, left side, Fig. 6a); (3) the orbit is more posteriorly positioned than estimated by Granger and Simpson (1929: fig. 4) but not as anteriorly positioned as estimated by Sloan (1981: fig. 6.14); (4) the jugal cannot be seen in lateral view rising above the level of the zygomatic arch as in earlier reconstructions; (5) a lacrimal bone is entirely absent (both on the orbital rim and within the orbit (DMNH EPV.136300, Fig. 12); (6) the frontal contributes substantially to the medial wall of the orbit, passing deep to the anterolateral extension of the parietal that passes forward to contact the nasal and maxilla (DMNH EPV.136300, Fig. 12); (7) the size (height) of the sagittal and nuchal crests are taller and more ridge-like than previously estimated (DMNH EPV.95284, Fig. 4a, b; DMNH EPV.134082, Fig. 5a, b); (8) the cranial vault is not evenly rounded posteriorly but instead ends in a distinct peak where the sagittal and nuchal crests intersect (external occipital protuberance), which is farther posterior than previously reconstructed (DMNH EPV.95284, Fig. 4a); and (9) the occipital condyles are not as anteriorly positioned relative to the nuchal crests as previously reconstructed and can be seen in this view (DMNH EPV.95284, Fig. 4b; DMNH EPV.134082, Fig. 5a, b).

Posterior View: (1) the nuchal crests are taller and more ridge-like than previously reconstructed, such that the dorsal aspect of the cranial cavity is barely visible (DMNH EPV.95284, Fig. 4f; DMNH EPV.134082, Fig. 5f); (2) the paroccipital processes are not enlarged to the extent that they extend ventrally below the level of the occipital condyles (DMNH EPV.95284, Fig. 4f; DMNH EPV.134082, Fig. 5f); (3) the foramen magnum is triangular rather than rounded in outline and is bordered dorsolaterally on each side by a prominent rim (DMNH EPV.95284, Fig. 4f; DMNH EPV.134082, Fig. 5f); (4) a large posttemporal foramen in the petrosal can be identified for the first time (DMNH EPV.134082, Fig. 5f); and (5) the occipital condyles are not as large and bulbous (DMNH EPV.95284, Fig. 4f; DMNH EPV.134082, Fig. 5f).

Nasals The nasals of *Taeniolabis* are extraordinarily long and broad elements that dominate the roof of the nasal cavity and form the dorsal margin of the external nasal aperture. They are wider posteriorly than anteriorly. As described and/or illustrated previously (Broom 1914; figs. 6, 8; Granger and Simpson 1929; figs. 4, 5A), each nasal articulates along strongly interdigitated sutures with the premaxillae and maxillae ventrolaterally, the parietal posterolaterally, and the frontal posteromedially. Interestingly, the midline suture with the contralateral nasal is also strongly interdigitated (rather than being planar) in at least AMNH 16321 (Figs. 3a, 7c); segments of this internasal suture can be discerned on the surface of DMNH EPV.95284 (Fig. 4c), DMNH EPV.136300 (Fig. 6c), and UCMP 98083 (Fig. 8c) but details cannot be distinguished. The medial aspects of the frontals project anteriorly to insert between the posterior ends of the nasals such that the nasal-frontal suture on each side is, from medial to lateral, oriented transversely, then obliquely (anteromedial to posterolateral), and then transversely again, ending at the triple junction with an anterolateral extension of the parietal.

The nasals are incomplete anteriorly in AMNH 16321 (Figs. 3a, b and 7a–e) and were reconstructed in dorsal and lateral views by Broom (1914: figs. 6, 8), Simpson (1926: fig. 2), and Granger and Simpson (1929: figs. 4, 5A) to extend anteromedially to meet their counterparts in the midline but to terminate at almost the same level as the premaxillae. DMNH EPV.95284 (Fig. 4a–c) and especially DMNH EPV.136300 (Fig. 6a–c), which have relatively complete premaxillae, demonstrate for the first time that these earlier reconstructions are inaccurate. The relatively complete premaxillae preserved in DMNH EPV.136300 (Fig. 6a–c) reveal the presence of strong internarial processes that extend the premaxillae considerably farther anteriorly than previously realized (see "Premaxillae" below). As such, the termination of the nasals anteriorly falls well short of the anterior extent of the premaxillae (see reconstructions in Fig. 10a, c). As seen in DMNH EPV.95284 (Fig. 4c), DMNH EPV.136300 (Fig. 6c), and UCMP 98083 (Fig. 8c), the anterior shape of the nasals in dorsal view is more squared than estimated by Broom (1914: fig. 6), Simpson (1926: fig. 2), and Granger and Simpson (1929: figs. 5A). We do not see definitive evidence of sutures near the midline anteriorly that might indicate the presence of an internarial bar formed by the premaxillae and inserted between the anterior ends of the left and right nasals but also acknowledge that none of the available specimens preserves this area pristinely; we therefore provisionally regard an internarial bar to be absent in *T. taoensis*. A distinct notch in the lateral outline of the external nasal aperture occurs where the nasal and premaxilla meet (Fig. 10a, c). This is not the same structure identified as an "anterior nasal notch" by Lillegraven and Krusat (1991; see also Wible and Rougier 2000), which occurs along the anterior margin of the nasal, not at its lateral edge.

Broom (1914) and Granger and Simpson (1929) did not record the presence of nasal foramina in AMNH 16321 but at least one large nasal foramen, now obscured by matrix and/or plaster on the original specimen (Fig. 3a) but visible on the µCT scans (Fig. 7c, e), is present on the right side; the canal leading from it projects posterointernally. Miao (1988: 18; see also Hurum 1994) stated that nasal foramina were present in a cranium of *Taeniolabis* "being studied by Simmons (personal communication)." This is presumably UCMP 98083, which was illustrated in ventral (but not dorsal) view by Greenwald (1988: fig. 1A). We here also confirm the presence of nasal foramina in UCMP 98083 (Fig. 8a, c, e). The available µCT scans reveal that there are at least five large foramina in the left nasal of UCMP 98083,

whereas only one is visible in the less well preserved right nasal. The foramina, which appear to pass internally into the nasal cavity, occur in the posterior half of each nasal and short neurovascular grooves extend generally anteriorly from the foramina toward the front or side of the snout. The single foramen visible on the right nasal is situated more posteriorly than any of those on the left. Four of the five foramina on the left are distributed along a more-or-less transverse line, with the fifth situated more anteriorly. We suspect that there are more foramina in the right nasal of UCMP 98083 (as illustrated in Fig. 10a) but that they are obscured by the relatively high amount of breakage on that side. Nonetheless, it is apparent that pronounced asymmetry in the number and position of nasal foramina is present. We could not conclusively confirm the presence of nasal foramina in any of the Corral Bluffs cranial specimens of *T. taoensis* but believe that this is owing to poor surface preservation.

Premaxillae The premaxillae were not well known previously, particularly anteriorly along the midline and on the palate. The sutures with the maxillae on the lateral aspects of the snout and with the nasals dorsally are as depicted by Broom (1914: figs. 6, 8) and Granger and Simpson (1929: figs. 4, 5A) in AMNH 16321. However, the premaxillae are fragmentary in this specimen and preclude evaluation of the presence or absence of the internarial process, the precise size, shape, orientation, and borders of the incisive foramina (anterior palatine foramina of Broom 1914; Granger and Simpson 1929), and the position and shape of the sutures with the maxillae on the palate.

The premaxilla bears two incisors (I2 and I3) and has three processes –– facial (posterodorsal), palatal, and internarial –– the last of which was previously entirely unknown for *Taeniolabis*. The facial process on the side of the snout is more or less vertical in orientation, but gently convex laterally, and ascends to contact the nasal along a strongly interdigitated, roughly horizontal suture. As it ascends, the process does not change greatly in anteroposterior length. The posterior suture with the maxilla, also strongly interdigitated, is longer than that with the nasal, extends from anteroventral to posterodorsal in lateral view, and is slightly convex anteriorly.

The palatal processes of the premaxillae are transversely domed, resulting in a gently concave palate, particularly anteriorly. The medial portion of the sutures between the palatal processes of the premaxillae and maxillae was previously unknown. We can confirm that, laterally, the sutures on AMNH 16321 (Fig. 7d) are as depicted in Granger and Simpson (1929: fig. 6), passing posteromedially from the premaxillary ridge (crista premaxillaris of Kielan-Jaworowska et al. 2005) for a short distance toward the midline. We cannot trace this premaxillary-maxillary suture on the palate of AMNH 16321 with confidence any farther toward the midline and therefore cannot determine if it intersects or passes posterior to the posterior border of the incisive foramen. Digital segmentation of DMNH EPV.136300, however, reveals that the suture passes directly medially from where it crosses the premaxillary ridge to intersect the incisive foramen toward its posterior end (Fig. 11). The suture then passes directly medially from near mid-length on the medial aspect of the incisive foramen to meet its contralateral counterpart on the other side of the interpremaxillary suture. This differs from the reconstruction in Kielan-Jaworowska and Hurum (1997: fig. 11C), who drew the suture as touching the posterior border of the incisive foramen but not passing any farther medially.

As definitively shown by DMNH EPV.136300, the incisive foramina are generally as conjectured by Granger and Simpson (1929: fig. 6, dashed lines) from AMNH 16321 but are smaller, more nearly oval (rather than reniform),

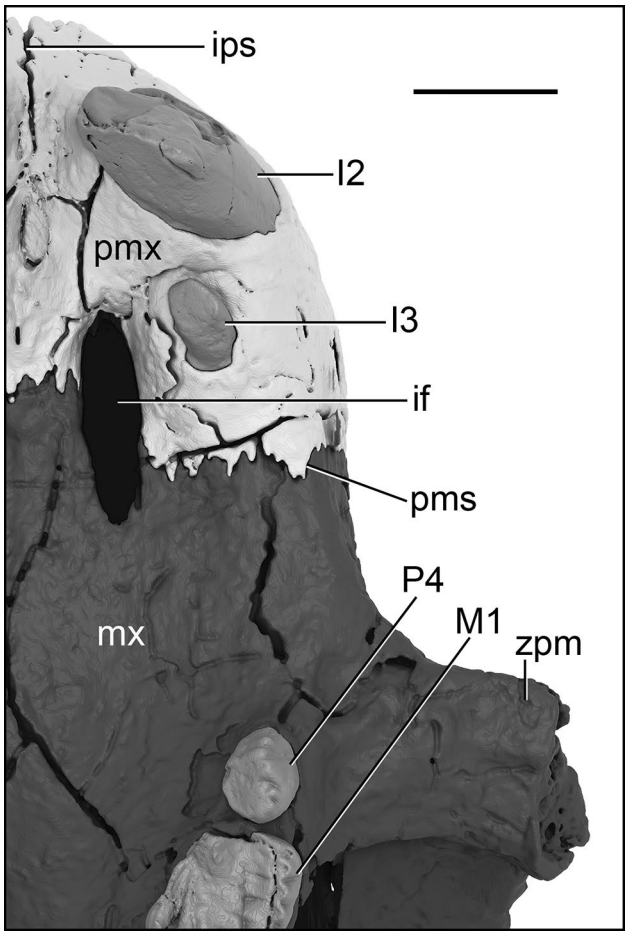

Fig. 11 Rendering of 3D virtual model of left side of palate, in ventral view, of *Taeniolabis taoensis*, DMNH EPV.136300, based on μCT data, illustrating premaxilla (light gray) and maxilla (dark gray) and the suture between them relative to the incisive foramen. Teeth are rendered in intermediate gray. Abbreviations: I2, upper second incisor; I3, upper third incisor; if, incisive foramen; ipms, interpremaxillary suture; M1, upper first molar; mx, maxilla; P4, upper fourth premolar; pms, premaxillary-maxillary suture; pmx, premaxilla; zpm, zygomatic process of maxilla. Scale bar = 1 cm

and slightly more lateral, closer to the alveoli of I3 than described and depicted by those authors. Although Broom (1914) explicitly stated that the size of the incisive foramina could not be determined in AMNH 16321 because of breakage, Granger and Simpson (1929: 614) described them as "oval, about 15 mm. long, and quite lateral in position, just internal to I^3." The best-preserved incisive foramen is on the left side of DMNH EPV.136300 (Figs. 6d and 11); it is elliptical in shape and measures 10.3 mm long and 3.4 mm wide, thus shorter than estimated and depicted by Granger and Simpson (1929: fig. 6).

The alveolus of I3 lies completely within the premaxilla. Its anterior border is directly lateral to the anterior border of the incisive foramen and its lateral border is immediately medial to the premaxillary ridge (best seen in DMNH EPV.136300 [Fig. 6d] and AMNH 16321 [Fig. 7d]), which marks the boundary between the facial and palatal processes of the bone. The premaxillary ridge is not sharp but is instead low and rounded (best seen on right side of AMNH 16321; Fig. 7d). Wible et al. (2019) opined that the ridge is absent in *Taeniolabis* (and *Ptilodus*); we regard it as present but low and rounded and just not as sharp and crest-like as in some other multituberculates, although it also appears as quite low and rounded in forms like *Catopsbaatar* (Kielan-Jaworowska et al. 2005: fig. 2C) and *Guibaatar* (Wible et al. 2019: fig. 3). Kielan-Jaworowska et al. (2005: 489) considered the ridge to be a probable synapomorphy of Djadochtatherioidea, stating that "to our knowledge it does not occur in other multituberculates," but its presence in *Taeniolabis* indicates that this is likely not the case. A premaxillary ridge is also depicted by Miao (1988: fig. 18) as quite sharp in *Lambdopsalis*. The alveoli of I2 and I3 in DMNH EPV.136300 (Figs. 6d and 11) are separated by short diastemata (Table 5) that are less than the lengths of the alveoli of I2. These distances appear to be shorter on AMNH 16321 but fracturing and plaster preclude accurate measurement on this specimen; plate XI in Broom (1914), which includes a photograph prior to reconstruction, suggests that the size of the diastemata are greater but this area is now damaged and less complete (compare Figs. 2b and 7d).

The anterior portions of the premaxillae of *Taeniolabis* were previously unknown; reconstructions of this region (Broom 1914; fig. 6; Granger and Simpson 1929; figs. 5A, 6), based on AMNH 16321, depicted a large empty space between the left and right I2s (see also Figs. 2a, b and 7c, d). The anterior parts of the premaxillae are, however, almost completely preserved in DMNH EPV.136300 (Figs. 6d and 11) and show, for the first time, that this space is occupied by substantial anterodorsal projections, the internarial processes, formed by the premaxillae. In lateral view, the internarial processes extend even farther anteriorly than the anterior-most extent of the I2s (Fig. 6a, b, d). The tips of the processes are, unfortunately, missing due to breakage and/or post-depositional erosion, thus precluding observation of their full height. However, because we do not see evidence of internarial processes inserted between the anterior ends of the nasals, we believe that they terminated shortly above where they are broken away and that they did not form a complete internarial bar separating the external nasal aperture into left and right halves (see reconstruction in Fig. 10a, c, d). The extensive bases of the left and right internarial processes abut one another and are separated only by the interpremaxillary suture. In anterior view (Figs. 6e and 10d), the ventral surfaces of the premaxillae form a strongly arched (concave ventrally) surface between the left and right I2s.

Septomaxillae There is no evidence of septomaxillae in any of the new specimens of *T. taoensis*, confirming Broom's (1914) earlier suspicion of their absence based on AMNH 16321.

Vomer We were unable to detect convincing evidence of the vomer in any of the available cranial specimens but regard this as simply owing to preservational issues and, in terms of μCT imaging, to the poor density contrast between bone and rock matrix, although there are indications of its presence in DMNH EPV.136300. There is, however, a prominent longitudinal ridge, which may be paired, on the dorsal surfaces of the premaxillae and maxillae on DMNH EPV.134082 (Fig. 5c, e), which has the floor of the nasal cavity exposed. The ridge appears to be situated to the right of the midline but it may be a slightly displaced midline structure and may represent the base to which the vomer articulated. Other displaced bony remnants in DMNH EPV.134082 are preserved more posteriorly that could represent the actual vomer but it is impossible to determine.

Lacrimals The lacrimal of *Taeniolabis* was described as having a small dorsal exposure by Kielan-Jaworowska and Hurum (1997). However, the lacrimal bone was not identified in *Taeniolabis* by Broom (1914), Granger and Simpson (1929), or other earlier workers, with Broom stating (p. 128) that, "[I]f one occurs, it must be very small and situated low down within the orbit." Indeed, although the anterior rim of the orbit is fragmented in AMNH 16321 and, whereas the nasomaxillary suture is abundantly clear, there is no trace of a suture in this region, thus tentatively confirming that the lacrimal did not have any facial exposure and indicating that the maxilla contributed exclusively to the formation of the anterior orbital rim. Similarly, none of the Corral Bluffs specimens available to us reveals evidence of a lacrimal, either on the orbital rim or within the orbit. This is arguably the result of poor preservation of surface detail in these specimens but digital segmentation of the mid-region of the cranium of DMNH EPV.136300 (Fig. 12) did not reveal the preservation of a lacrimal, either on the orbital rim or inside the

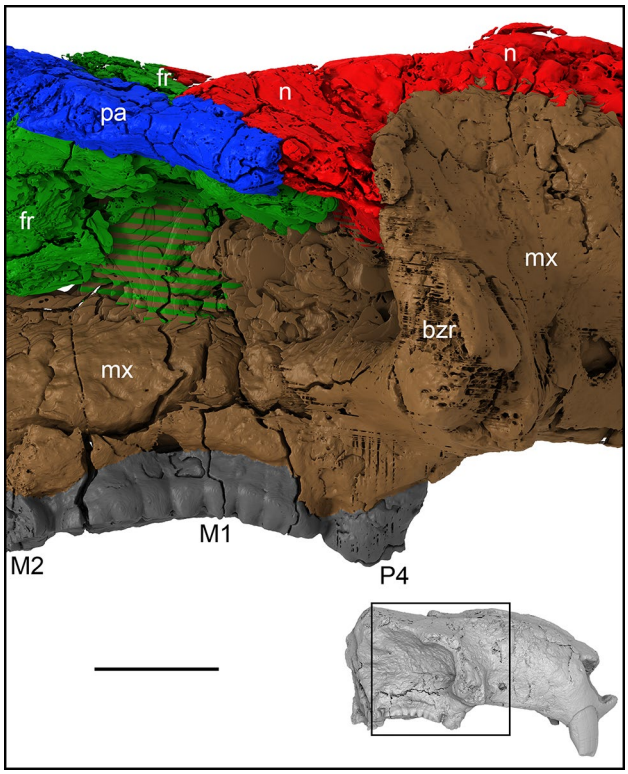

Fig. 12 Rendering of 3D virtual model of medial wall and rim of right orbit of *Taeniolabis taoensis*, DMNH.EPV.136300, based on μCT data. Position indicated in right lateral view of entire specimen in inset at lower right. Frontal is depicted in green, parietal in blue, nasal in red, maxilla in brown, and maxillary teeth (P4–M2) in gray. Region where discrimination between frontal and maxilla not possible shown with green and brown stripes and region where discrimination between nasal and maxilla not possible shown with red and brown stripes. Abbreviations: bzr, broken zygomatic root; fr, frontal; M1, upper first molar; M2, upper second molar; mx, maxilla; n, nasal; P4, upper fourth premolar; pa, parietal. Scale bar = 1 cm

orbit. Furthermore, because we also do not see evidence of a lacrimal in UCMP 98083, we conclude that it was entirely absent in *Taeniolabis*.

Maxillae The maxilla of *T. taoensis* is a large element that houses a small, simple premolar (P4) and two, large, complex molars (M1, M2) in its alveolar process. The left and right cheektooth rows are approximately parallel to one another but diverge slightly anteriorly.

The facial process of the maxilla articulates via interdigitated sutures anteriorly with the premaxilla and dorsally with the nasal, essentially as depicted by Broom (1914: figs. 6, 8) and Granger and Simpson (1929: figs. 4, 5A). The facial process also extends posteromedially along and medial to the orbital rim to contact a long, anterolaterally directed projection of the parietal; this contact is possible, in part, because of the absence of an intervening facial process of the lacrimal. The contribution of the maxilla to the anterior orbital rim is more completely preserved in DMNH EPV.95284 (Fig. 4) and DMNH EPV.136300 (Fig. 6) than it is in AMNH 16321 (Fig. 7), in which much of the rim is broken away, but is best revealed by digital segmentation of the partially preserved anterior orbital rim (zygomatic root) in DMNH EPV.136300 (Fig. 12). This specimen demonstrates that the lacrimal is indeed absent and that the anterior orbital rim is composed solely by the maxilla. The only additional feature worthy of note on the facial process is a single, infraorbital foramen and a prominent groove extending anteriorly from it, situated directly anterior to the large root of the zygoma and well anterior to the level of P4.

Digital segmentation of the mid-region of the cranium in DMNH EPV.136300 demonstrates that the maxilla provides a vast contribution to the medial orbital wall, extending dorsally for a considerable distance from the alveolar process (Fig. 12). There, it contacts the nasal anterodorsally and the frontal dorsally, although the suture between the maxilla and frontal cannot be discerned in one area. Unfortunately, features that plausibly lie within or bordered by the maxilla (e.g., maxillary and sphenopalatine foramina) on the medial wall of the orbit cannot be seen. Because a lacrimal is not present, the facial process of the maxilla contributes exclusively to the anterior and some of the dorsal part of the orbital rim, which is continued posteriorly by the parietal.

The facial process of the maxilla transitions into the zygomatic process but, in dorsal view, there is a prominent angle between the longitudinal axes of the two that marks the anterior margin of the root of the zygoma. The included angle, measured along the external margins of the two processes, in the least deformed of the Corral Bluffs specimens, DMNH EPV.136300 (Fig. 6c, d), is approximately 123°, slightly sharper than rendered by Granger and Simpson (1929: fig. 5A; ~129°) and especially by Broom (1914; Fig. 6; 138°) based on AMNH 16321 (our measurement of AMNH 16321 is roughly consistent with that obtained by Granger and Simpson). The anterior margin of the root of the zygoma is well anterior to P4 and the posterior margin begins roughly opposite the embrasure between P4 and M1.

The zygomatic process of the maxilla is extraordinarily deep and its dorsal surface forms the ventral margin of the orbit. The process extends posteriorly to contact the slightly less deep zygomatic process of the squamosal. The two processes articulate on the zygomatic arch along a planar suture that, in lateral view, is restricted to the anterior half of the arch (i.e., the zygomatic process of the maxilla is much shorter than the zygomatic process of the squamosal) and extends from anterodorsal to posteroventral.

Hopson (in Hopson et al. 1989) stated that the presence or absence of a jugal could not be determined in AMNH 16321. UCMP 98083 (Figs. 8d and 13) reveals the presence of an anterior fragment of the rudimentary jugal on the medial aspect of the zygomatic process of the maxilla (see "Jugals" below). This contrasts with the reconstructions by Broom (1914: figs. 6, 8) and Granger and Simpson (1929: figs. 4, 5A), which depict (in dotted outlines) a much larger jugal, with at least part of it rising above the zygomatic processes of the maxilla and squamosal, bearing a postorbital process. UCMP 98083 indicates that the jugal would likely not be visible in lateral view (Fig. 8b).

An anterior zygomatic ridge on the lateral aspect of the zygomatic arch of the maxilla, marking the dorsal boundary for the origin of masseter superficialis pars anterior, was described as present in AMNH 16321 by Kielan-Jaworowska et al. (2005: 509; based on observation of photographs in Broom 1914: pls. XI, XII). In addition, Yaoming Hu (pers. comm. to Kielan-Jaworowska et al. 2005: 509) was said to have identified an anterior zygomatic ridge in AMNH 16321. We are unable to confirm this identification on the original specimen; the right zygomatic arch is mostly missing but the left arch is quite well preserved, although fragmented with several small missing areas filled with plaster; compare Fig. 3a, b with Fig. 7a, c, d). We also cannot identify curved ridges on what is preserved of the right zygomatic arch of UCMP 98083 (Fig. 8b, c). The lateral surface of the zygomatic process of the maxilla on both AMNH 16321 and UCMP 98083 is essentially smooth (except for cracks) and gently convex. There is, however, a prominent depression, wide anteriorly and tapering and becoming indistinct posteriorly, on the ventral surface of this process in AMNH 16321 (Fig. 7d), that, despite incompleteness and fracturing, appears to be present in UCMP 98083 (Fig. 8d) as well. We assume, therefore, that the masseter superficialis pars anterior originated from this depression rather than from the lateral surface of the process. The poor surface preservation of the Corral Bluffs specimens precludes independent confirmation of these observations.

Granger and Simpson (1929:614) described the maxillary portion of the palate on AMNH 16321 "as greatly arched or domed, reaching its greatest height between the premolars." This region of the palate in AMNH 16321 is reconstructed with large amounts of plaster (Fig. 3b; see Broom 1914: pl. XI and Fig. 7d for images of the specimen without plaster infillings). The DMNH specimens, especially DMNH EPV.136300 (Fig. 6d), which is the least deformed in this region, indicate that the maxillary portion of the palate, although arched/domed, is not as strongly concave as reconstructed in AMNH 16321. The greatest degrees of curvature of the palate appear to be farther posterior, between the M1s, and far anteriorly, on the premaxillae between the I2s.

On the palate, the full extent of the suture of the maxilla with the premaxilla was digitally segmented in DMNH EPV.136300 and is shown to pass medially from the premaxillary ridge and intersect the posterior margin of the incisive fossa (Fig. 11; see more detailed description in "Premaxillae" section above). Faint sutures between the maxillae and the palatines can be seen on only one specimen, DMNH EPV.134082 (Fig. 5d); the fact that they are more or less symmetrically developed lends credence to their identification. The combined sutures (described more fully in the "Palatines" section below), beginning opposite the distal quarter of M1, result in a shape similar to that of a bell, with the top of the bell situated anteriorly (see reconstruction in Fig. 10b). We could not identify either major or minor palatine foramina but ascribe this to poor preservation rather than to true absence. Finally, whereas Broom (1914: 128) identified a "small, oval" palatal vacuity, Granger and Simpson (1929: 614) opined that AMNH 3041 (a specimen not seen in the current study) "seems positively to indicate that palatal vacuities were not present," but then, in a later paper, Simpson (1937b: 735) left some doubt, stating that "[t]here was probably no palatal vacuity" in *T. taoensis*. The Corral Bluffs specimens, particularly DMNH EPV.136300 (Fig. 6d), demonstrate conclusively that palatal vacuities are absent.

Palatines The palatines appear to not have been preserved in AMNH 16321; they are now reconstructed in plaster (compare Figs. 3b and 7d; see also Broom 1914: pl. XI), although Granger and Simpson (1929: fig. 6) drew some dashed lines indicating that the hard palate extended well posterior to the distal ends of M2. Distinct palatine-maxilla sutures were reconstructed by Kielan-Jaworowska and Hurum 1997: fig. 11C) to indicate that the palatines were, together, roughly bell-shaped with a sharply pointed posterior tip and extending from medial to M2 to, again, well posterior to M2 but we are unaware of any previously known specimens that demonstrate this size, position, and shape.

The palatines are completely, although poorly, preserved in two of the Corral Bluffs specimens, DMNH EPV.95284 (Fig. 4d) and DMNH EPV.134082 (Fig. 5d), and anterior parts of them are present in DMNH EPV.136300 (Fig. 6d). Although fractured and deformed, they are also preserved in UCMP 98083 (Fig. 8d). Of these specimens, only DMNH EPV.134082 reveals faint sutures with surrounding bones (reconstructed in Fig. 10b) and even these must be characterized as somewhat uncertain. The anterior-most extent of the tentative suture with the maxilla is on the midline opposite the posterior quarter of M1. It extends laterally in a strong convexity and then posteriorly along a sinuous line until passing lateral to the pterygopalatine ridge and medial to the distal end of M2 and the retromolar extension of the maxilla. The fact that the maxillary-palatine sutures are

symmetrically present on both sides in DMNH EPV.134082 provides some degree of confidence in their identification. It is clear that the central area of the palatines did not extend as far posteriorly as indicated in previous reconstructions and nor did they terminate medially in a very sharp point (Granger and Simpson 1929: fig. 6; Kielan-Jaworowska and Hurum 1997: fig. 11C; Wible et al. 2019: fig. 22C). Although the left and right palatines come together posteriorly to form a blunt, uvula-like tip that may have extended slightly past the level of the posterior margins of the left and right M2s, the main portions of the palatines did not. Also, although the posterior ends of the palatines appear to be slightly thickened toward the midline and potentially ventrally deflected slightly in DMNH EPV.134082 (Fig. 5d) and DMNH EPV.95284 (Fig. 4d), there is no convincing evidence for a large, strongly thickened, laterally expansive, markedly raised postpalatine torus as seen in several Late Cretaceous djadochtatherioids (see "Bony Palate" below). We therefore regard this feature to be absent in *Taeniolabis*, which is consistent with how it was scored by Rougier et al. (2016) and Wible et al. (2019). Finally, despite the new specimens, and μCT analysis of them as well as of previously known specimens, the positions of the major and minor palatine foramina cannot be discerned and whether or not the palatine has any exposure within the orbit also remains unknown.

Jugals Broom (1914: 128) reconstructed the jugal of *Taeniolabis* in AMNH 16321, stating that the anterior portion "did not reach far round the anterior orbital margin" and "probably had a postorbital process," and that the posterior portion was "perfectly preserved" and "merely a narrow splint of bone." Hopson et al. (1989:206), as had Simpson (1937b) previously, however, concluded that the presence or absence of a jugal in AMNH 16321 "cannot be determined due to the poor preservation of the bone surface on the zygoma." We essentially concur with these authors but do see a depression on the medial aspect of the squamosal portion of the left zygomatic arch, along the dorsal half, that could represent a "scar" for the posterior end of the jugal (Fig. 7d). More anteriorly, there is a faint outline of what might be a suture for the rest of the element extending onto the zygomatic process of the maxilla. These traces are not convincing but are in approximately the same position as those depicted for the reconstructed zygomatic arch of *Ptilodus* depicted by Hopson et al. (1989: fig. 5); medial to the arch, along its dorsal aspect, and overlapping the maxilla-squamosal suture. Similarly suggestive, but not definitive, evidence of a jugal is present on the medial aspect of the right zygomatic arch of DMNH EPV.95284 (Fig. 4d). Digital segmentation of the right zygomatic arch of UCMP 98083, however, does reveal a fragment of bone that we tentatively interpret to be at least part of the anterior end of a jugal (Fig. 13). It sits within a shallow fossa on the medial aspect of the zygomatic arch but it is clearly incomplete, as indicated by broken surfaces. It likely would not have been visible in lateral view, at least not to the extent depicted by Broom (1914: fig. 8) and Granger and Simpson (1929: figs. 4, 5A), who showed it as a substantial element forming all of the ventrolateral rim of the orbit.

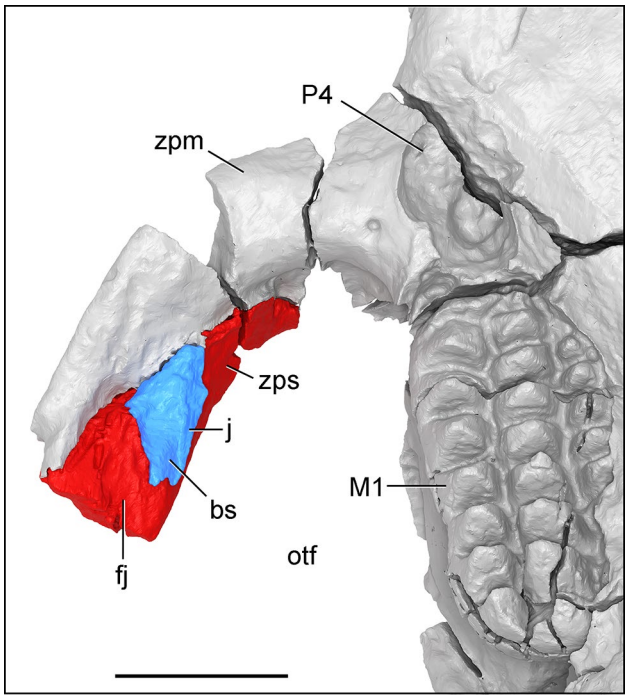

Fig. 13 Rendering of 3D virtual model of fragmentary jugal of *Taeniolabis taoensis* on medial aspect of right zygomatic arch of UCMP 98083, based on μCT data. Fragmentary jugal depicted in blue, zygomatic process of squamosal in red, and rest of cranium in gray. Abbreviations: bs, broken surface; fj, facet for jugal; j, jugal (anterior fragment); M1, upper first molar; otf, orbitotemporal fenestra; P4, upper fourth premolar; zpm, zygomatic process of maxilla; zps, zygomatic process of squamosal. Scale bar = 1 cm

The dorsal margin of the preserved left zygomatic arch of AMNH 16321 is fragmentary in the region where one might expect a postorbital process indicating the position for attachment of the ventral end of the orbital ligament and marking the lower posterior boundary of the orbit. Broom (1914: fig. 8) had speculatively illustrated the postorbital process on the jugal, roughly opposite the postorbital process on the parietal. Although the zygomatic arches are not well preserved on DMNH EPV.95284 (Fig. 4), the narrowed, ridge-like dorsal edge may be preserved on the right side and, if so, indicates that the postorbital process is on the zygomatic process of the squamosal and slightly posterior to the position indicated by Broom; unfortunately, deformation and poor surface preservation of the specimen does not allow us to have confidence in that conclusion.

Frontals The frontals of *T. taoensis* were reconstructed by Broom (1914: fig. 6; followed by Granger and Simpson 1929: fig. 5A) in dorsal view, based on AMNH 16321, as small, flat, and unfused in the midline, with each having a long, straight medial margin, a shorter, slightly curved (concave posterolaterally) posterolateral margin, and an irregular margin anterolaterally that is still shorter. Overall, the frontals are in the shape of a stemmed arrowhead, with the acute tip directed posteriorly. The medial, posterolateral, and anterior/anterolateral margins articulate with the contralateral frontal, the parietal, and the nasal, respectively. The posterolateral suture, especially on the left side, is prominently displayed on DMNH EPV.134082, where its contact with the parietal has been substantially displaced (Fig. 5c, e). There is no contact with a lacrimal bone because that element is absent in *Taeniolabis* (see "Lacrimals" above).

Broom (1914: fig. 8; followed by Granger and Simpson 1929: fig. 4) reconstructed the frontals as not contributing to either the dorsal orbital margin or to the medial orbital wall. Instead, the parietal was reconstructed as extending forward to contact the maxilla both above and within the orbit, thus contributing to the posterior part of the supraorbital margin (with the maxilla forming the anterior part) and also to the posterior part of the medial orbital wall. Digital segmentation of the medial orbital wall in DMNH EPV.136300 reveals that, although the parietal extends a process forward along the orbital rim to contact the nasal, it simply overlies the frontal in this area and the two main parts of the frontal, the dorsal frontal plate and the lateral orbital process, are connected deep to this parietal process (Fig. 12). Within the orbit, the frontal contacts the nasal anterodorsally and has a long, roughly horizontal contact ventrally with the maxilla, although parts of the intervening suture could not be fully discerned.

Parietal The parietal of *Taeniolabis*, in dorsal view, is expansive. In the middle portion of its anteroposterior extent, it lies on either side of the frontals, the contact being V-shaped and paralleled posterolaterally by the low, rounded temporal ridges. Farther anteriorly, the parietal extends as narrow processes lateral to the frontals that pass so far forward that contact is made with the nasals anteromedially and, ultimately, with the facial processes of the maxillae anteriorly. Posterior to the acute V-shaped termination of the frontals, the parietal comprises the entire posterior portion of the roof of the cranial cavity. Although the posterior-most median portion of the parietal in AMNH 16321 (Fig. 7c) is broken away, and although the left temporal ridge is more fragmentary than the right temporal ridge, the portions that are preserved indicate that the temporal ridges converged ~32 mm from the back of the cranium but did not fully meet in the midline, thus forming a double-ridged sagittal crest, the long apices of the two, more-or-less parallel crests being separated by ~6 mm. This double sagittal crest is not particularly tall. By contrast, the sagittal crest in DMNH EPV.95284 (Fig. 4a–c, e, f) is considerably longer (~45 mm), taller, and is a single, prominent midline feature. The sagittal crest in DMNH EPV.134082 (Fig. 5a–c, e, f) is not as well preserved but appears to more closely resemble that of DMNH EPV.95284 than that of AMNH 16321 in length (~41 mm), prominence, and singularity. The nuchal crests are mostly broken away in AMNH 16321 (Fig. 7) but they are almost complete in DMNH EPV.95284 (Fig. 4) and DMNH EPV.134082 (Fig. 5), demonstrating that they were very prominent and sharp, flaring posteroventrolaterally (concave anteriorly) toward the squamosals, and overhang the concave occipital region. Unfortunately, the suture between the parietal and the squamosals cannot be identified with certainty in any of the available specimens and therefore it is impossible to know the relative contributions of each element to the nuchal crests. Similarly, the suture between the parietal and the occiput is obscured in all known specimens.

DMNH EPV.95284 belies the conclusion of Simpson (1926: 233, 235) that "the sagittal and occipital [= lambdoid] crests are only moderately developed" in multituberculates and that "the temporal muscle was weak." In this specimen (and DMNH EPV.134082, Fig. 5), these crests are very prominently developed. Gambaryan and Kielan-Jaworowska (1995: 82) had earlier observed that the sagittal crest is "prominent" in *Taeniolabis* (and *Lambdopsalis*).

Gambaryan and Kielan-Jaworowska (1995: 85) inferred the position of the postorbital process in *Taeniolabis* from illustrations in Broom (1914) as being "small and situated on the anterior part of the parietal." We can confirm this position and the fact that it is a swelling rather than a distinct, pointed process from direct observation of AMNH 16321 (Fig. 7c) and DMNH EPV.95284 (Fig. 4c). This region is not well enough preserved on DMNH EPV.134082 to make similar assessments. Deformation of the cranium of DMNH EPV.95284 makes a conclusive determination of the size of the process difficult but, on the left side, it appears to be quite prominent.

Orbitosphenoids/Alisphenoids (and Anterior Lamina of the Petrosal) Sutures between the elements of the lateral wall of the braincase could not be distinguished in any of the specimens in our sample, including the extent of the orbitosphenoid, alisphenoid, and anterior lamina of the petrosal (see "Petrosals" section below). Nevertheless, a few features are visible. A large foramen for the mandibular division of the trigeminal nerve is visible in UCMP 98083 (Fig. 14d). It is oval (anteroposteriorly longer than dorsoventrally tall). A possible foramen for the ramus superior of the stapedial

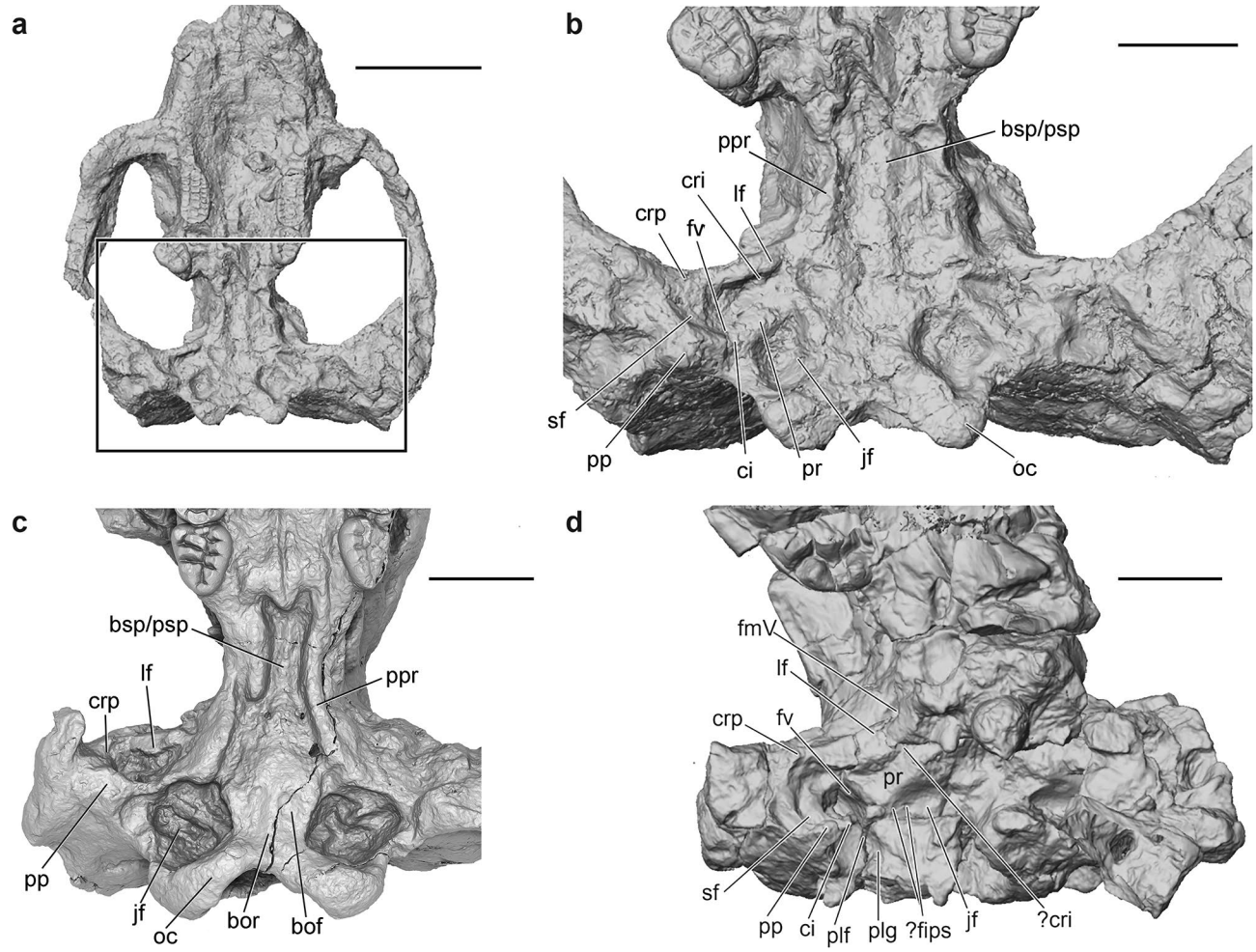

Fig. 14 Rendering of 3D virtual model of mesocranial and basicranial regions of *Taeniolabis taoensis*, based on µCT data, in ventral view. **a**, DMNH EPV.95284, overview of cranium; **b**, DMNH EPV.95284, enlarged view of area outlined by rectangle in **a**; **c**, DMNH EPV.134082; **d**, UCMP 98083. Abbreviations: bof, basioccipital fossa; bor, basioccipital ridge; bsp/psp, basisphenoid/presphenoid; ci, crista interfenestralis; cri, canal for ramus inferior; crp, crista parotica; fips, foramen for inferior petrosal sinus; fmV, foramen for mandibular division of trigeminal nerve; fv, fenestra vestibuli; jf, jugular fossa; lf, lateral flange; oc, occipital condyle; plf, perilymphatic foramen; plg, perilymphatic groove; pp, paroccipital process; ppr, pterygopalatine ridge; pr, promontorium; sf, stapedius fossa. Scale bars in a, c = 5 cm, b = 2 cm, d = 1 cm

artery is visible roughly in the center of the lateral braincase wall in DMNH EPV.95284 (Fig. 4b) and UCMP 98083 (Fig. 8b). A deep groove extends anterodorsally from it along the lateral braincase wall.

Basisphenoid/Presphenoid A subtle, low, rounded midline ridge extending directly forward from the basioccipital ridge toward the posterior margin of the choanae can be seen in DMNH EPV.134082 (Figs. 5d and 14c) and, to a lesser extent, in DMNH EPV.95284 (Figs. 4d and 14b). We interpret this ridge to be comprised of the basisphenoid and presphenoid, as interpreted for other multituberculates (e.g., Miao 1988; Wible and Rougier 2000), but, owing to poor surface preservation in these specimens, sutures delimiting either of these small elements are impossible to discern.

Pterygoids Sutures that would delimit the margins of the pterygoid also cannot be seen in any of the available cranial specimens of *T. taoensis* but presence of the bone is indicated by tall, elongate, symmetrically curved (concave laterally) ridges that extend posteriorly from the end of the palate (reconstructed in Fig. 10b). Barghusen (1986) termed these structures 'pterygopalatine ridges.' More specifically, these ridges in *Taeniolabis* pass posteriorly from opposite the distolingual margin of M2 and then gently curve laterally, diverging slightly from one another before merging seamlessly (i.e., without a discernible suture) in the region of the promontorium on the petrosal. Although relatively poorly preserved in DMNH EPV.95284 (Figs. 4d and 14b), the pterygopalatine ridges are reasonably well preserved in DMNH EPV.134082 (Figs. 5d and 14c), where the one on

the left side seems to be the least disturbed by postmortem taphonomic processes (the anterior part of the right ridge is displaced medially into the basipharyngeal canal). It is assumed that these pterygopalatine ridges articulate dorsally and/or laterally with the alisphenoids and that they articulate with the presphenoid/basisphenoid duo medially but this cannot be documented in any of the available specimens. Because of the poor surface preservation of this region in all available specimens, there is also no distinct pterygoid hamulus in evidence.

Squamosals The right zygomatic arch of AMNH 16321, except for a small section anteriorly, contributed by the zygomatic process of the maxilla, is composed almost entirely of plaster and the left arch is fragmented, with several small missing gaps having been filled with plaster, but not significantly deformed (compare Fig. 3a, b with Fig. 7). The zygomatic arches in DMNH EPV.95284 are preserved almost in their entirety (except for a short posterior section of the right arch) but are markedly bilaterally asymmetrical because of differential preservation and deformation (Figs. 2a, b and 4). Only the posterior half of the left zygomatic arch and very short anterior and posterior sections of the right zygomatic arch are preserved in DMNH EPV.134082 (Figs. 2c, d and 5), only the anterior roots of the arches are preserved in DMNH EPV.136300 (Fig. 6), and only an anterior portion of the right zygomatic arch is preserved in the juvenile cranium UCMP 98083 (Greenwald 1988: fig. 1A; Fig. 8). Measurements of depth and width of the zygomatic arches, where available, are provided in Table 5.

AMNH 16321 (Fig. 7a) and UCMP 98083 (Fig. 8b) exhibit an obliquely oriented suture (from anterodorsal to posteroventral) between the zygomatic process of the squamosal and the zygomatic process of the maxilla, the suture ending posteroventrally at slightly less than midlength along the zygomatic arch. This is as depicted in lateral views by Broom (1914: fig. 8) and Granger and Simpson (1929: fig. 4), and in Figs. 7a, 8b, and 10c. The illustrations by Broom and by Granger and Simpson added a short dorsal section of the suture that turned posteriorly again, creating an asymmetrical V-shaped suture in lateral view. The dorsal margin of the zygomatic arch of AMNH 16321 is broken away anteriorly, precluding clear evidence for this, as well for a jugal that is depicted as rising above the level of the arch. UCMP 98083 (Fig. 8b) is inconclusive in demonstrating the shape of the maxillary-squamosal suture but indicates that the jugal probably did not rise above the dorsal margin of the zygomatic arch. Only the ventral-most part of this suture is visible on the medial side; more dorsally, the suture appears to be obscured by the diminutive jugal (see "Jugals" section above).

The cross-sectional shape of the zygomatic process of the squamosal is essentially that of a tall, isosceles triangle, the most acute angle of which is positioned dorsally. In lateral view, it is distinctly arched, convex dorsally and concave ventrally. Gambaryan and Kielan-Jaworowska (1995) identified intermediate and posterior zygomatic ridges (purportedly for the origins of masseter superficialis pars posterior and masseter medialis pars posterior, respectively), as seen on the squamosal of djadochtatherioid multituberculates, the anterior zygomatic ridge (purportedly for origin of masseter superficialis pars anterior) being situated more anteriorly and confined to the lateral surface of the maxilla. As stated above (section on "Maxillae"), Kielan-Jaworowska et al. (2005), based on observation of photographs in Broom (1914: pls. XI, XII) and a personal communication from Yaoming Hu, identified anterior and intermediate zygomatic ridges in AMNH 16321 and thereby implied comparability to the situation in djadochtatherioids. Our examination of the left zygomatic arch of AMNH 16321 indicates that some qualification is necessary. An elongate, shallow, lenticular depression facing ventrolaterally (more ventrally than laterally) on the squamosal extends anteriorly from just lateral to the anterior end of the glenoid fossa to approximately midlength on the arch, anterior to the maxilla-squamosal suture. The lateral margin of this depression is likely equivalent to the intermediate zygomatic ridge of Gambaryan and Kielan-Jaworowska (1995) but it is important to emphasize that the depression itself faces more ventrally than it does laterally (unlike in djadochtatherioids). Following Gambaryan and Kielan-Jaworowska (1995), the depression served as the site of origin for pars posterior of the superficial masseter. Medial to this depression is a shallow groove that, following the inferences of Gambaryan and Kielan-Jaworowska (1995), may have served as the origin for masseter lateralis. It is relatively wide posteriorly, extending forward from just anterior to the glenoid fossa; the level of its anterior termination is not distinct.

The glenoid fossa, best preserved on AMNH 16321 (Fig. 7d) and DMNH EPV.134082 (Fig. 5d), is very large and somewhat tear-drop shaped (the sharp apex of the tear situated anterolaterally), being slightly longer anteroposteriorly than wide mediolaterally, although its anterior termination is not distinct (see estimated measurements in Table 5). Its longitudinal axis is not strictly anteroposterior but, instead, trends in a slightly anterolateral to posteromedial direction. The articular surface of the fossa is flat anteroposteriorly but shallowly concave from medial to lateral, with distinct rims both anteromedially and posterolaterally, as best seen in AMNH 16321 (Fig. 7d).

As stated above (see "Parietal"), the suture between the parietal and the squamosals cannot be discerned in any of the available specimens but, farther laterally, immediately anterior to the very prominent nuchal crests, Granger and Simpson (1929: fig. 5A) identified a partial suture between the squamosal and the petrosal in dorsal view.

Petrosals The description of the petrosal of *T. taoensis* is based on DMNH EPV.95284, DMNH EPV.134082, and UCMP 98083 (Fig. 14). Of those specimens, DMNH EPV.95284 is the most intact but the surface of the petrosal is altered because of postmortem taphonomic processes, and some finer structures are therefore difficult to discern. Furthermore, the density difference between sediment and bone is poor in this specimen and, as such, µCT data cannot aid significantly in identification of foramina or in tracing pathways of nerves and vessels. Although the external surface of UCMP 98083 (Fig. 14d) preserves greater detail (e.g., muscular attachments, grooves, foramina) than DMNH EPV.95284 (Fig. 14b), the basicranium of this specimen is more deformed. The ventral surface of the petrosal of DMNH EPV.134082 (Fig. 14c) is highly altered, however similarities between DMNH EPV.134082 and DMNH EPV.95284, including, for example, the position of the jugular fossa and promontorium, are evident. The density difference between sediment and bone is likewise poor in DMNH EPV.134082, particularly on the left side. The contrast is slightly better on the right side, where the inner ear is discernible. Most of the petrosal of AMNH 16321 is reconstructed in plaster and does not preserve actual morphology.

In ventral view, the promontorium is anteromedially-posterolaterally oriented, elongate, and forms a distinct ridge that divides the middle ear cavity into two deeply excavated spaces (Fig. 14). The surface of the promontorium does not appear to bear any distinct grooves for the internal carotid or stapedial arteries. This is best seen in the partially preserved promontorium of UCMP 98083 (Fig. 14d). DMNH EPV.95284 (Fig. 14b) does not preserve any grooves either, although it should again be noted that the surfaces of the petrosal are preservationally altered, and it is possible that any grooves might have simply been obliterated in the process. Much of the right promontorium is covered in matrix in DMNH EPV.134082 and that of the left is too poorly preserved to evaluate its surface morphology (Fig. 14c).

Based on the µCT scans and preserved external morphology of the specimens, it cannot be confirmed whether the perilymphatic duct exited the inner ear through a perilymphatic groove from the perilymphatic foramen or was enclosed in a cochlear canaliculus (and that a true fenestra cochleae was present). In UCMP 98083 (Fig. 14d), a faint groove is visible on a block close to the perilymphatic foramen/fenestra cochleae, possibly representing a perilymphatic groove, but the block is separated from the petrosal and rotated out of position, and it is therefore unclear whether it truly connected to the perilymphatic foramen in life. Nevertheless, we tentatively refer to the foramen as the "perilymphatic foramen" in the description and comparison, as it is present in all multituberculates known to date.

The shape and size of the fenestra vestibuli and perilymphatic foramen are not obvious in DMNH EPV.95284 and DMNH EPV.134082 and are obscured by a large fracture in UCMP 98083. The fenestra vestibuli appears large in UCMP 98083, but the true size is difficult to estimate as the posterior and anterior edges appear to be broken (Fig. 14d). Separating the perilymphatic foramen and fenestra vestibuli is a short, narrow, and posteriorly trending bony ridge, the crista interfenestralis. Medial to the crista interfenestralis and extending along the whole length of the promontorium is a deeply excavated jugular fossa. The jugular fossa is somewhat teardrop-shaped, with a larger and rounded posterior edge and a narrower anterior edge. The outline and size of the fossa is best seen on the right side of DMNH EPV.95284. Although the position of the fossa is also recognizable in DMNH EPV.134082 (Fig. 14c), its size appears to be considerably exaggerated by erosion. The broken fragment next to the perilymphatic foramen obscures the posterior aspect of the right jugular fossa in UCMP 98083, but the anterior aspect is visible and confirms the shape seen in the DMNH specimens (the left jugular fossa is not visible). There are several small openings in the lateral wall of the jugular fossa (along the posteromedial edge of the promontorium). Based on the poor quality of preservation, it is unclear if these represent exposed emissary veins that drained medially into the inferior petrosal sinus or actual foramina for veins that drained medially from the inferior petrosal sinus into the jugular fossa (Fig. 14d).

The crista interfenestralis is continuous with the paroccipital process posteriorly dividing the rear of the middle ear cavity (divided post-promontorial tympanic recess). The space lateral to the crista interfenestralis and promontorium is likewise deeply excavated and extends slightly farther anteriorly than the jugular fossa (DMNH EPV.95284, Fig. 14b). Laterally, a prominent crista parotica defines the border of the lateral space, best seen in DMNH EPV.95284 (Fig. 14b), UCMP 98083 (Fig. 14d), and on the right side of DMNH EPV.134082 (Fig. 14c). At the posterior aspect of the lateral space, along a slightly elevated shelf, is an elongate fossa for the stapedius muscle (Fig. 14b, d). The stapedius fossa is best seen in UCMP 98083 and is barely visible in the DMNH specimens. The stapedius fossa does not seem to extend onto the lateral aspect of the crista interfenestralis as in *Kryptobaatar* and *Guibaatar* (Wible and Rougier 2000; Wible et al. 2019). The posterior wall of the lateral space is formed by the base of the paroccipital process. The paroccipital process is distinct, small, and rounded, extending ventrally only slightly past the surface of the petrosal. This is much smaller than reconstructed by Granger and Simpson (1929: fig. 5B), who illustrated it extending ventral to the level of the occipital condyles.

The crista parotica is anteromedially confluent with a broad and low lateral flange. The lateral flange is medially inflected and contacts the promontorium anteriorly (Fig. 14b–d). At the anterior tip of the lateral flange is a small foramen that

could represent the canal for the ramus inferior of the stapedial artery (Fig. 14b, d). However, the foramen could not be traced through the µCT scans and its course is uncertain.

Several other foramina should pierce the crista parotica and lateral flange but are not visible on the external surface or in the µCT scans of any of the specimens, including the foramen for the ramus superior of the stapedial artery, tympanic aperture of the prootic canal (for the prootic sinus), and the secondary facial foramen (for the facial nerve). This is clearly due to poor preservation and does not represent absence of the foramina as those foramina (or a combination of them) are generally present in multituberculates (see "Comparisons and Discussion"). Lateral to the crista parotica lies the epitympanic recess. The fossa incudis, for the crus breve of the incus, is not preserved in any of the specimens. In other multituberculates the posterior aspect of the epitympanic recess houses a narrow fossa incudis (*Kryptobaatar*, Wible and Rougier 2000; cf. *Tombaatar*, Ladevèze et al. 2010; *Mangasbaatar*, Rougier et al. 2016). Anterior to the epitympanic recess, in what possibly represents the anterior lamina, appears to be a large foramen that opens endocranially into the cavum epiptericum. The opening is best visible in UCMP 98083 (fmV in Fig. 14d), and appears to be a single large foramen, but due to poor preservation we cannot rule out that it is a fossa with two distinct foramina. We interpret this foramen to be an opening for the mandibular division of the trigeminal nerve. Finally, in occipital view, the posttemporal foramen, which we assume lies within the petrosal, is large; it is best preserved on the left sides of DMNH EPV.134082 (Fig. 5f) and UCMP 98083 (Fig. 8f). It is surrounded by a funnel-shaped entryway, the posttemporal fossa.

The following description of the inner ear of *Taeniolabis* is primarily based on UCMP 98083, the best-preserved specimen for this region in the sample (Fig. 15; measurements in Table 6). Much of the inner ear is intact in

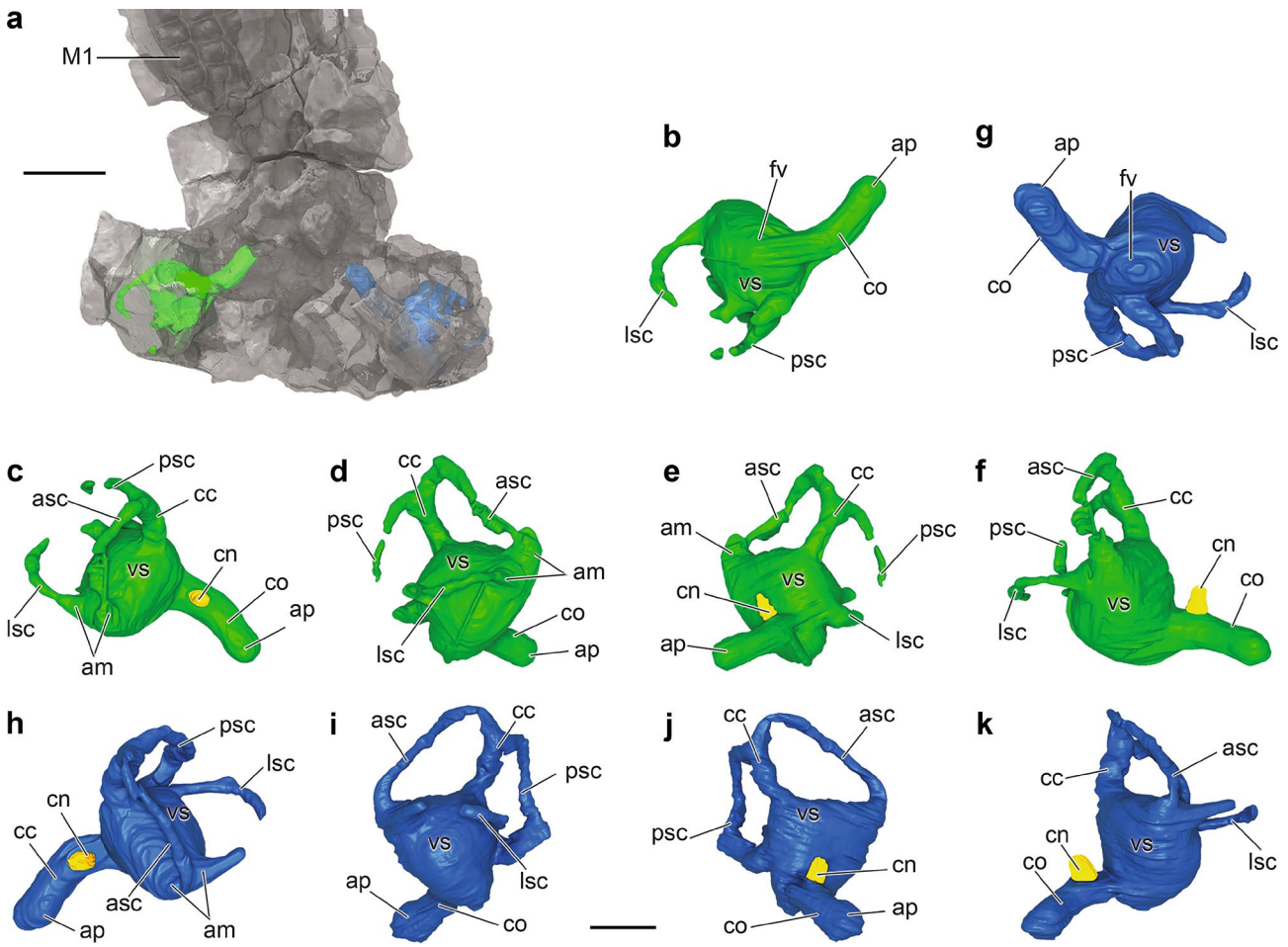

Fig. 15 Rendering of 3D virtual model of inner ears of *Taeniolabis taoensis*, UCMP 98083, based on µCT data. **a**, position of right (green) and left (blue) inner ears in ventral view of cranium; right (**b–f**) and left (**g–k**) inner ear in **b**, **g**, ventral; **c**, **h**, dorsal; **d**, **i**, lateral; **e**, **j**, medial views; and **f**, **k**, anterior views. Abbreviations: am, ampulla; ap, apex; asc, anterior semicircular canal; cc, crus commune; cn, cochlear nerve (yellow); co, cochlear canal; fv, fenestra vestibuli; lsc, lateral semicircular canal; psc, posterior semicircular canal; vs, vestibule. Scale bar in **a** = 10 mm, in **b–k** = 5 mm

UCMP 98083 (aside from parts of the semicircular canals), but the endocast is infilled with sediment that has nearly the same density as the bone, which makes differentiation of the endocast difficult in some areas (e.g., cochlear canal on the left, semicircular canals on the right). Overall, the cochlear canal and vestibule can be better differentiated on the right side, whereas the semicircular canals are more visible on the left side. Some information can be gleaned from DMNH EPV.95284. The density difference between bone and sediment infill of the endocast is worse than in UCMP 98083, but still allowed for tracing a very coarse outline of the right and left inner ears. The outline, however, might not as reliably present true morphology. The right inner ear is discernible in DMNH EPV.134082. The density contrast is much poorer on the left side where only the vestibule and parts of the semicircular canals are visible. The inner ear is not preserved among the basicranial fragments present in AMNH 16321.

The cochlear canal is only gently curved laterally in dorsal or ventral view (49°). The basal portion of the canal is directed anteromedially, then curves to an anterolateral direction (Fig. 15). The slender cochlear canal gently changes from a relatively round cross section at the apex to a more oval cross section at the base, with a width and height of 1.8 mm and 2.0 mm at mid-length. The right cochlear canal measures 7.8 mm in length (measured from the apex to the contact of the vestibule and cochlear canal). The left cochlear canal is slightly longer (8.7 mm), however its outline is less visible in the µCT scans and we believe that the 7.8 mm measured on the right is a more accurate representation of the morphology. The cochlear canal constitutes about 8.1% of cranial length in the juvenile UCMP 98083. The apex of the cochlear canal is only very gently expanded, possibly indicating the presence of a lagena macula (Fig. 15). A separate canal for the lagenar nerve could not be discerned in the µCT scans. This does not necessarily imply the absence of such a canal because the density contrast in the specimen is simply not sufficient to clearly delimit whether a lagenar nerve canal was present or not. The cochlear nerve passes into the cochlear canal through what appears to be a single foramen along the dorsal aspect of the canal. Lack of contrast makes it unclear whether any bony support structures for the cochlear nerve or hearing membrane existed. Given that the cochlear nerve passes through a single foramen in most multituberculates (Meng and Wyss 1995; Fox and Meng 1997; Ladevèze et al. 2010; Luo et al. 2016; Csiki-Sava et al. 2018; Wible et al. 2019), it is plausible that the failure to see such structures in UCMP 98083 and DMNH EPV.134082 might represent actual absence of a cribriform plate and primary or secondary bony laminae.

The vestibule of *Taeniolabis* is large, with a volume of 253–270 mm^3. It is smooth and rounded and does not provide any indications for the boundaries of the utricle or saccule. The vestibular nerve could not be traced reliably in the µCT scans and can thus not aid in the identification of the saccule or utricle. Of note is that the fenestra vestibuli opens into the vestibule, indicating that the scala vestibuli is incorporated into the inflation of the vestibule. The ampullae are slightly rounded and, in parts, difficult to differentiate from the enlarged vestibule.

The semicircular canals are better differentiated on the left side of UCMP 98083; although also present on the right side, the sediment infill on the right (Fig. 15b–f) is nearly the same density as the bony labyrinth and the canals could not be as reliably traced as on the left (Fig. 15g–k). The radius of curvature of the three semicircular canals is fairly similar, with the posterior canal being slightly the largest (Table 6). The difference in radius of curvature between the posterior canal and the lateral and anterior canals is greater on the left than on the right, which might be driven by a fracture in the left posterior semicircular canal. The left posterior semicircular canal exhibits a peculiar bend, but the corresponding part on the right could not be traced and it is unclear what the actual morphology might have looked like. The anterior and posterior semicircular canals meet to form a long and robust crus commune. A secondary crus commune is absent; the lateral and posterior semicircular canals do not merge but remain separate, leading to two ampullae.

Interparietal Discrimination of sutures in the occipital region is insufficient on any of the available specimens to resolve whether or not an interparietal (or, more finely, a postparietal and left and right tabulars) is preserved.

Table 6 Measurements of inner ear in *Taeniolabis taoensis* (UCMP 98083). Cochlear canal length measured from tip of apex to border of vestibule and cochlear canal. Total inner ear length and cochlear canal curvature follows Schultz et al. (2017). Abbreviations: ASC, anterior semicircular canal; LSC, lateral semicircular canal; PSC, posterior semicircular canal

	Left	Right
ASC height	5.7 mm	5.3 mm
ASC width	7.9 mm	6.6 mm
PSC height	6.1 mm	5.8 mm
PSC width	6.4 mm	6.5 mm
LSC height	4.4 mm	3.8 mm
LSC width	5.7 mm	5.6 mm
Crus commune length	5.1 mm	4.8 mm
ASC radius of curvature	3.4	3.0
PSC radius of curvature	3.5	3.1
LSC radius of curvature	3.1	3.1
Cochlear canal length	8.7 mm	7.8 mm
Cochlear canal curvature	—	49°
Vestibular volume	253 mm^3	270 mm^3
Total inner ear length	—	18.7 mm
Total cranial length	95.8 mm	95.8 mm
Cochlear canal/cranial length	9.1%	8.1%

Occipital The boundaries of the various components of the occipital bone (supraoccipital, paired exoccipitals, basioccipital) cannot be observed on any of the adult cranial specimens preserving the occipital region in our sample (DMNH EPV.95284, DMNH EPV.134082, AMNH 16321) simply because the sutures necessary to do so are either fused or obscured, with or without the aid of μCT imagery. There is, however, suggestive evidence of the ventral aspects of the sutures between the supraoccipital and left and right exoccipitals in the juvenile cranium of UCMP 98083 (Fig. 8f). These slant from dorsolateral to ventromedial and indicate that the supraoccipital contributed to a small median portion of the dorsal margin of the foramen magnum. The dorsal boundary of the supraoccipital, presumably with the parietal, cannot be discerned.

It is not possible to know how much of the nuchal region of the cranium is contributed by the occipital (in addition to, potentially, the parietal, interparietal, petrosal, and squamosal), again because sutures are not visible, even in UCMP 98083. Furthermore, because of the poor surface preservation of the Corral Bluffs specimens and incomplete preservation, fragmentation, and/or deformation of the San Juan Basin specimens, other osteological features expected to be found in, or bordering on, the occipital cannot be differentiated. Despite these limitations, some major features of the occipital region of *T. taoensis* can be described for the first time.

The occipital region is tall and, assuming that an interparietal is not present (see reviews of distribution among fossil and extant mammaliaforms in Koyabu et al. 2012; Krause 2014b), ends dorsally in prominent nuchal crests. Whether or not the occipital bone extends to actually participate in the nuchal crests cannot be discerned but it does so, or nearly so, in all multituberculates for which this region is known (see "Comparisons and Discussion"). The nuchal crests themselves are very prominent, joining with the equally prominent sagittal crest of the parietal in a triple junction to form a salient, peaked external occipital protuberance. This therefore differs strongly from the reconstructions by Broom (1914: fig. 8) and Granger and Simpson (1929: fig. 4), at least in lateral view, where the posterodorsal outline of the cranium appears more evenly rounded (convex posterodorsally). Furthermore, the position of the external occipital protuberance is farther posterior than depicted by Broom (1914: fig. 6) and Granger and Simpson (1929: fig. 5A). The nuchal area dorsal and lateral to the foramen magnum, between it and the prominent nuchal crests, is concave. Overall, because the occipital condyles lie slightly posterior to the level of the external occipital protuberance, the nuchal area is slightly slanted from anterodorsal to posteroventral in lateral view.

The occipital condyles, previously unknown in *T. taoensis*, are preserved in DMNH EPV.95284 (Figs. 4b, d, f and 14b) but are best preserved in DMNH EPV.134082 (Figs. 5a–d, f and 14c). They project posteriorly, slightly beyond a transverse line formed by the nuchal crests, which is farther posterior than speculatively reconstructed by Broom (1914: fig. 6) and especially Granger and Simpson (1929: figs. 5A, 6). The condyles themselves, in posterior view, occupy the lower third of the area surrounding the foramen magnum and are large and rounded posteriorly and ventrally. In ventral view, the condyles are separated by a broad, V-shaped (approximately 90º) odontoid (=intercondyloid) notch. In posterior view, the foramen magnum, as preserved in DMNH EPV.95284 (Fig. 4f) and DMNH EPV.134082 (Fig. 5f), is triangular in shape, slightly wider than tall (Table 5), with each of the two dorsolateral sides of the triangle being straight, posteriorly projecting crests. The foramen appears to be more rounded laterally in the juvenile UCMP 98083 (Fig. 8f). The foramen itself is directed straight posteriorly. A linear, vertically oriented projection of bone midway between the dorsal margin of the foramen magnum and the external occipital protuberance on DMNH EPV.95284 (Fig. 4f) represents a remnant of the external occipital crest. The crest is more faintly visible in DMNH EPV.134082 (Fig. 5f), AMNH 16321 (Fig. 7f), and UCMP 98083 (Fig. 8f).

The basioccipital, on the ventral surface immediately anterior to the foramen magnum, is poorly preserved in all of the specimens. The best indication of its morphology is preserved in DMNH EPV.134082, where a low, midline ridge, with two shallow fossae on either side of it, extends anteriorly for a short distance (Fig. 14c). Farther laterally, the basioccipital contributes a significant medial border of the jugular fossae. A faint, transverse suture anterior to the low, midline ridge and two shallow fossae flanking it may mark the position of the spheno-occipital synchondrosis in DMNH EPV.134082.

Dentary

The dentary of *T. taoensis* has been described and/or illustrated by Cope (1884a: fig. 3a–d; 1884b: pl. XXIIIc, fig. 1, 1a–c [specimen number not provided]), Osborn and Earle (1895: fig. IA, C [specimen number not provided]), Gregory (1910: fig. 8 – AMNH 748 and AMNH 968), Broom (1914: fig. 8 and pl. XI – AMNH 748), Simpson (1926: fig. 5D [specimen number not provided]); Granger and Simpson (1929: fig. 4 – AMNH 16310; condyle based on AMNH 745; reproduced or redrawn in Matthew 1937: fig. 71; Simpson 1937a: fig. 3A; Simpson 1937b: fig. 3D; Sloan 1981: fig. 6.14; Kielan-Jaworowska and Hurum 1997: fig. 12 [coronoid process based on holotype dentary of *T. lamberti*, CCM 70–110]; Kielan-Jaworowska et al. 2004: fig. 8.40C; Weil and Krause 2008: fig. 2.2A; Rougier et al. 2016: fig. 31; Wible et al. 2019: fig. 21C), Greenwald

(1988: fig. 1B, C – UCMP 98083), Gurovich (2006: fig. 4.7 [specimen number not provided]), and Kondrashov and Lucas (2015: fig. 4 – NMMNH P-8631). The following descriptions and comparisons are based primarily on first-hand examination of DMNH EPV.130973 (Figs. 2g, h, 9a–c) and AMNH 16310 (Figs. 3c, d and 9d–f), complemented with observations from µCT-scanned images of the juvenile dentaries of UCMP 98083 (Fig. 8g–l; see also Greenwald (1988: fig. 1B, C) and photographs of AMNH 745 (Fig. 3e, f), AMNH 748 (Fig. 3g, h), AMNH 968, and AMNH 27734 (Fig. 3i–n). DMNH EPV.130973 (Figs. 2g, h and 9a–c) is among the most complete dentaries known for *T. taoensis* and is missing only the dorsal portions of the coronoid process, the terminus of the mandibular condyle, and a few inconsequential fragments elsewhere; its surface preservation, however, is not as pristine as that of AMNH 16310 (Figs. 3c, d and 9d–f). The horizontal ramus of AMNH 16310 is complete and very well preserved but only the anterior half of the ascending ramus is preserved; as such, much of the coronoid process, much of the pterygoid and masseteric fossae, and all of the mandibular condyle are missing. Both dentaries of UCMP 98083 (Fig. 8g–l) are preserved but both are missing large portions (particularly posteriorly), have numerous cracks, and are considerably deformed. AMNH 745, AMNH 748, AMNH 968, and AMNH 27734 reveal more of the coronoid process and mandibular condyle than is preserved in DMNH EPV.130973, AMNH 16310, and UCMP 98083. Combined, these specimens permit a full reconstruction of the dentary of *T. taoensis* (Fig. 10f–h) and indicate significant changes to the size, shape, and position of the coronoid process and mandibular condyle.

The prior descriptions and illustrations of the dentary have revealed or confirmed that the horizontal ramus houses i1, p4, and m1–2; that there is a long diastema between i1 and p4; and that the ramus is short and deep (see Table 7 for measurements). The horizontal rami are also extraordinarily thick mediolaterally and meet anteriorly at an included angle of approximately 40–45° (precise measurement is not possible because of the difficulty of orienting specimens consistently and because the symphysis is unfused; see also fig. 1C in Osborn and Earle 1895). Given that the cheektooth row is set obliquely relative to the longitudinal axis of the dentary, and given the inferred palinal direction of the power stroke of the chewing cycle, the left and right rows would have been roughly parallel in life.

In lateral view, the ventral margin of the dentary is sinuous (most strongly developed in AMNH 16310; Figs. 3c, d and 9d, e): convex anteriorly in the region of the incisor root (ventral to the diastema), concave ventral to m1, and convex posteriorly (ventral to the masseteric fossa). The posterior convexity extends posterodorsally in a smooth arc toward the condyle in DMNH EPV.130973 but has a bend that is variably expressed in AMNH 745, AMNH 748, AMNH 968, and AMNH 27734. The ventral surface below the masseteric fossa is notable in being wide (widest at midlength and tapering anteriorly and posteriorly), flat, and strongly tilted in the coronal plane from ventrolateral to dorsomedial. The dorsal margin of the horizontal ramus is strongly concave in the region of the diastema, with the section above the incisor root being at an approximate right angle to the section anterior to the root of p4. On the lateral aspect of the dentary, a single mental foramen is present, situated anterior to and below the nadir in the arc of the dorsal margin of the diastema. The foramen is small; the canal immediately deep to it, measured in AMNH 16310, is only approximately, on average, 1.15 mm in diameter, which seems extraordinarily small for such a large animal.

The masseteric fossa is defined by anterodorsal and anteroventral margins (variably expressed as ridges) and extends anteriorly onto the horizontal ramus in the adult specimens in the sample, converging to a rounded point below p4. In the left dentary of UCMP 98083 (Fig. 8g), which represents a juvenile individual, this point appears to be slightly more posteriorly positioned, ventral to the anterior part of m1, but it is below p4 on the right (Fig. 8j). The names applied to the anteroventral margin of the masseteric fossa were reviewed by Gambaryan and Kielan-Jaworowska (1995); we follow those authors in referring to it as the masseteric crest even though it presents as a low rounded ridge in *T. taoensis*. Passing posteriorly, where it intersects the ventral margin of the dentary in lateral view, the masseteric crest becomes the masseteric line, which continues posteriorly and then posterodorsally to form

Table 7 Measurements (in mm) of adult dentaries in study sample of *Taeniolabis taoensis* (juvenile dentaries of UCMP 98083 too fractured and deformed for reliable measurement)

	DMNH EPV.130973	AMNH 16310
Total length of dentary[a]	117*	—
Diastema between i and p4[b]	27.3	23.5
Length of horizontal ramus[c]	72.5	68.8
Depth of horizontal ramus[d]	40.0	35.8
Horizontal ramus length/depth	1.81	1.92
Width of horizontal ramus[e]	14.6	14.9
Length of cheektooth row[f]	36.5	38.2

*Estimated because of incompleteness

[a]Measured from mesial margin of incisor alveolus to posterior end of mandibular condyle

[b]Measured from distal margin of incisor alveolus to mesial margin of p4 alveolus

[c]Measured from mesial margin of incisor alveolus to distal end of m2

[d]Measured as vertical depth from alveolar margin of m1 to ventral margin of dentary (on lateral side)

[e]Measured as transverse width below mesial portion of m1

[f]Measured from mesial margin of p4 to distal margin of m2

the ventral and posteroventral borders of the masseteric fossa. Both DMNH EPV.130973 (Fig. 9a) and AMNH 16310 (Fig. 9d) reveal a gently curved ridge, convex anteriorly, inside the masseteric fossa that begins dorsally at the approximate level of the embrasure between m1 and m2. There appears to be good evidence for this ridge in the photographs of AMNH 748 (Fig. 3g) and AMNH 968 (not illustrated) as well, but it is less clear in those of AMNH 745 (Fig. 3e) and AMNH 27734 (Fig. 3i). When present, the ridge descends through the masseteric fossa and becomes less distinct as it continues ventrally to ultimately intersect the masseteric line close to where the latter transitions to the masseteric crest. We refer to this feature as 'intramasseteric ridge 1.' The depression anterior to the ridge, bounded anteriorly by the convergence of the anterodorsal and anteroventral (masseteric crest) margins is the masseteric fovea (fovea massetericus of Gambaryan and Kielan-Jaworowska 1995). In other words, the masseteric fovea is the anterior-most component of the masseteric fossa (which is not the case for all multituberculates – see "Comparisons and Discussion" below). It is likely that intramasseteric ridge 1 represents the dividing line between portions of the masseter muscle. Gambaryan and Kielan-Jaworowska (1995) regarded the fovea as serving as the insertion area of masseter medialis pars anterior (anterior deep masseter of Sloan 1979 but also known as the infraorbital portion of zygomaticomandibularis Druzinsky et al. 2011), whereas the rest of the masseter muscle inserted posterior to the fossa. Farther posteriorly, at least as seen in DMNH EPV.130973 (Fig. 9a), the masseteric fossa is divided by another ridge, here termed 'intramasseteric ridge 2,' which ascends from the masseteric line where it changes directions from the ventral to the posteroventral boundary of the massteric fossa. The ridge appears to become less distinct dorsally but this observation is based on DMNH EPV.130973, which exhibits some breakage in the area (Fig. 9a). This ridge presumably marks yet another division of the masseter muscle. Based on DMNH EPV.130973 (Fig. 9a) and AMNH 27734 (Fig. 3i) in particular, we infer that the masseteric fossa (and the dentary as a whole) was shorter posteriorly than reconstructed by earlier workers (e.g., Granger and Simpson 1929: fig. 4A), in part because the mandibular condyle was not suspended on a long, posterodorsally projecting condylar process.

Kielan-Jaworowska et al. (2005) inferred the presence of a masseteric protuberance in *Taeniolabis taoensis* based on illustrations in Granger and Simpson (1929: fig. 4) and Simmons (1987: fig. 4.4). In AMNH 16310, DMNH EPV.130973, and UCMP 98083, all of which preserve good surface detail in this region, however, the masseteric crest, defining the anteroventral border of the masseteric fossa, does not end abruptly anteriorly in an enlargement similar to that identified as a protuberance in forms like *Catopsbaatar* (Kielan-Jaworowska et al. 2005: figs. 7; 9B$_1$) or *Djadochtatherium* (Kielan-Jaworowska and Hurum 1997: fig. 5A). Indeed, the anteroventral margin of the masseteric fossa becomes less distinct as it passes anteriorly. We also see no evidence of a protuberance in the photographs of AMNH 745, AMNH 748, AMNH 968, or AMNH 27734. Finally, it must be noted that Fig. 4.4 in Simmons (1987) is of the holotype dentary (CCM 70–110) of *T. lamberti* (not *T. taoensis*) and the anteroventral margin of the masseteric fossa is broken posteriorly, thus precluding determination of relative prominence along the margin and confident appraisal of the presence or absence of a masseteric protuberance; we suspect it did not exist in that species either.

On the medial side of the horizontal ramus, the mandibular symphysis is unfused (contra Weil and Krause 2008). It occupies much of the area ventral to the diastema and is comma-shaped with the head of the comma positioned anteriorly and the tail trailing posteriorly along the ventral aspect of the ramus; this is most pristinely preserved and best seen on AMNH 16310 (Fig. 9e). AMNH 16310 exhibits a distinct ridge passing posteroventrally from the dorsal portion of the symphysis, ending below the mesial portion of m1; this ridge is much less distinct on DMNH EPV.130973 (Fig. 9b). In coronal section, the medial side of the horizontal ramus below the cheek teeth is gently concave (AMNH 16310) to almost flat (DMNH EPV.130973), bounded inferiorly by a ridge that becomes stronger as it passes posteriorly to form the ventral border of the pterygoid fossa, the pterygoid shelf, on the ascending ramus. As measured on the medial side of both DMNH EPV.130973 and AMNH 16310, the occlusal plane of the molars lies at an angle of approximately 20° relative to the ventral surface of the dentary; this is considerably higher than scored for *Taeniolabis* in recent phylogenetic analyses by, for example, Kielan-Jaworowska and Hurum (2001: char. 35, "11–17 degrees"), Mao et al. (2016: char. 7, "11–17 degrees"), and Wible et al. (2019: char. 73, "equal to or less than 10°").

The pterygoid fossa, more complete on DMNH EPV.130973 (Fig. 9b) than on AMNH 16310 (Fig. 9e), is massive and deeply excavated laterally and anteriorly, providing a huge insertion area for the medial pterygoid muscle. Its anterior border is very distinct and gently convex anteriorly, merging ventrally with a very strong pterygoid shelf (pterygoid crest of Simpson 1926), which bounds the entire ventral aspect of the fossa. The pterygoid shelf itself is very wide but narrows as it ascends posterodorsally toward the posterior margin of the mandibular condyle, just as the pterygoid fossa becomes shallower posteriorly. The mandibular foramen, for passage of the inferior alveolar nerve, could not be identified in any of the specimens available to us, either on the specimens themselves or through μCT imagery. It is likely to have been positioned as in *T. lamberti*,

on the anterior wall of the pterygoid fossa at a level below m2 (see Simmons 1987).

The size and shape of the mandibular condyle and its position relative to the rest of the dentary have not been well documented previously. It is not preserved on any of the specimens we were able to examine firsthand (DMNH EPV.130973, AMNH 16310) or through μCT imagery (UCMP 98083) but is preserved on the specimens for which we have photographs (AMNH 745, AMNH 748, AMNH 968, AMNH 27734), courtesy of AMNH curator Jin Meng, and therefore can now be documented more fully. The condyle is best preserved on AMNH 27734 and is illustrated here in four views (Fig. 3k–n). The condyle was not as large and globular or with as long a neck as reconstructed by past authors (e.g., Osborn and Earle 1895; fig. 1A, C; Gregory 1910; fig. 8; Granger and Simpson 1929; fig. 4A), and certainly not as much as reconstructed in plaster on AMNH 16310 (Fig. 3c, d). In dorsal view (Fig. 3m), the condyle is lenticular in shape, strongly convex posteriorly and gently concave anteriorly, with the ridge passing anteriorly to form the mandibular notch doing so from the medial side of the condyle. In posterior view (Fig. 3n), the condyle extends only a short distance onto the posterior surface and has a distinctly convex ventral margin. The lateral and medial views (Fig. 3k, l) document a short and unconstricted condylar neck and a gently convex dorsal surface that becomes more convex posteriorly. The mandibular notch, in side view, is evenly rounded (concave dorsally) extending forward from the condyle and merging with the posterior margin of the coronoid process (Fig. 3i, j).

The coronoid process is incomplete in all specimens known to us; it was reconstructed as very low by Cope (1884a: fig. 3a, b; 1884b: pl. XXIIIc, fig. 1, 1a), who also incorrectly reconstructed a distinct angular process, as very tall and recurved by Osborn and Earle (1895: fig. 1A), and as moderately tall and recurved by Broom (1914: fig. 8) and Granger and Simpson (1929: fig. 4A). The process is, however, nearly complete and well preserved in AMNH 27734 (Fig. 3i, j), missing only some fragments along the posterior edge; it is the only specimen preserving the full anterior margin and dorsal tip. This specimen demonstrates that the coronoid process, while moderately tall, was likely not recurved, at least not strongly. The anterior base of the process is also at least partially preserved in DMNH EPV.130973 (Figs. 2g, h and 9a, b), AMNH 745 (Fig. 3e, f), AMNH 748 (Fig. 3g, h), AMNH 968, and AMNH 16310 (Figs. 3c, d and 9d, e). In lateral view, the anterior base arises opposite the posterior portion of m1 (i.e., m2 not visible in this view; DMNH EPV.130973, AMNH 748, AMNH 16310) or the anterior portion of m2 (AMNH 968, AMNH 27734). Acknowledging that there is also variability depending upon how the dentary is oriented, this is in slight contrast to Simmons (1987) who observed that it arises only opposite m1 and used it as a diagnostic feature differentiating *T. taoensis* from *T. lamberti*, in which, in the holotype and only known specimen preserving the dentary, it arises opposite the anterior part of m2; there appears to be more intraspecific variation in this feature than previously known. The process extends posterodorsally from the anterodorsal margin of the masseteric fossa, and produces a broad, shallow, U-shaped temporal groove (sulcus temporalis of Gambaryan and Kielan-Jaworowska 1995) between it and the buccal alveoloar margin of m2. The dorsal apex of the coronoid process is peaked, and the anterior and posterior edges descend more or less symmetrically from that peak, although the anterior edge is longer and less vertical. Although the posterior edge of the coronoid process is not preserved in AMNH 27734, it has been reconstructed in plaster to descend and then merge in a concave, rounded outline with the mandibular notch that seems natural (Fig. 3i–l). This shape was used in the reconstruction of the dentary in Fig. 10f, h.

Comparisons and Discussion

Comparisons with the craniomandibular morphology of other multituberculate taxa are warranted because of the new anatomical information provided for our subject taxon, *Taeniolabis taoensis*, but also because many new cimolodontan multituberculate taxa have been described, many of them represented by skull material, since the last major descriptions of *T. taoensis* material (Broom 1914; Granger and Simpson 1929). This includes specimens of other taeniolabidids, consisting of a dentary of *Taeniolabis lamberti* (see Simmons 1987) and a few cranial fragments of *Kimbetopsalis simmonsae* (see Williamson et al. 2016). But more detailed comparisons are possible with cranial specimens of the family most closely related to taeniolabidids, lambdopsalids, in part because of new material of *Sphenopsalis* (Mao et al. 2016) but, most significantly, nearly complete skull material of the type genus and best-known representative, *Lambdopsalis* (Miao 1988). Of particular importance also is the recent discovery of a nearly complete skull (and partial postcranial skeleton) of *Yubaatar*, regarded as the immediate outgroup of Taeniolabidoidea (Xu et al. 2015). In addition, a plethora of skull material of many new genera and species of cimolodontan multituberculates has been discovered in the Late Cretaceous of Asia and Europe, primarily in the form of djadochtatherioids and kogaionids, respectively. The former has been described in considerable detail (e.g., Kielan-Jaworowska 1970a, 1970b, 1971, 1974; Kielan-Jaworowska and Dashzeveg 1978; Kielan-Jaworowska et al. 1986, 2005; Hurum 1994,

1998a, b; Gambaryan and Kielan-Jaworowska 1995; Hurum et al. 1996; Rougier et al. 1996b, 1997, 2016; Kielan-Jaworowska and Hurum 1997, 2001; Wible and Rougier 2000; Ladevèze et al. 2010; Wible et al. 2019) but only preliminary details of the latter have been published to date (Rădulescu and Samson 1996, 1997; Smith and Codrea 2015; Csiki-Sava et al. 2018).

Cranial Size and Body Mass Estimates

The cranium of *Taeniolabis taoensis* is the largest known among multituberculates. There are no other multituberculates that are known, even from fragmentary remains, that might have approached the size of *T. taoensis*, which we estimate from cranial size relative to a large sample of extant therian mammals to have had a body mass of approximately 35–40 kg (see "Description"). For the comparisons below, except for the closely related taeniolabidid *Kimbetopsalis simmonsae*, which is not known from the lower dentition but reported to be ~21% smaller than *T. taoensis* (based on length of M1; Williamson et al. 2016), we primarily use size of m1 because it is the only element in common to compare with most other large multituberculates.

The length and width of *T. taoensis* m1s are 18.7–21.4 mm and 9.4–11.4 mm ($n = 35$), respectively, and the length and width of its M1s are 21.9–24.4 mm and 10.8–12.1 mm ($n = 22$), respectively (Simmons 1987; table 2), thus establishing it as the largest known multituberculate, Cenozoic or Mesozoic, from anywhere. The only m1 assigned to the congeneric *T. lamberti* is 16.0 mm long and 8.0 mm wide (Simmons 1987: table 3). *Bubodens magnus*, known from a single m1, is the largest known Mesozoic multituberculate from North America (Wilson 1987), but the length (12.8 mm) and width (6.0 mm) of the tooth are less than two-thirds the average dimensions of the m1s of *T. taoensis*. *B. magnus* is considerably larger than the largest known Mesozoic multituberculate from Eurasia, *Yubaatar zhongyuanensis* (m1 length = 9.2 mm; width = 3.6 mm) (Xu et al. 2015), which is less than half the size of *T. taoensis*. *Boffius splendidus* is the largest known Cenozoic multituberculate from Europe (M1 length = 15.2–15.3 mm; width = 8.7–9.0 mm; m1 width = 9.6–10.0 mm) (Vianey-Liaud 1979; De Bast and Smith 2017: table 1 [m1 measurements for IRSNB M2195 not used because they pertain to m1 of the palaeoryctid *Belgoryctes thaleri*; T. Smith, pers. comm. – see De Bast and Smith 2017: table 4]) and *Sphenopsalis nobilis* is the largest known Cenozoic multituberculate from Asia (m1 length = 13.6 mm; width = 7.3 mm) (Mao et al. 2016); both are, on average, considerably smaller than *T. taoensis*. All of the multituberculates, purported or substantiated, from Gondwanan landmasses are much smaller than any of the above forms (see review in Krause et al. 2017).

Cranial Shape

The most apt descriptor of the cranium of *T. taoensis* is "robust," evoking comparisons with those of extant Australian wombats (*Vombatus ursinus*) or North American beavers (*Castor canadensis*). It is almost as wide as long (Table 5) and is, in general, of very heavy construction, with massive, squared zygomatic arches, a short, blunt snout, and prominent sagittal and nuchal crests indicating bulky masticatory and cervical musculature (Fig. 10). By contrast, the crania of other multituberculates are, in general, relatively gracile (see comparison figures including some of the most recently described cimolodontan taxa in Csiki-Sava et al. 2018: suppl. fig. 8; Wible et al. 2019: figs. 21–23). The cranial shape of *Lambdopsalis* most resembles that of *Taeniolabis*, the primary differences being the relative narrowness (in dorsal or ventral view) and shallowness (in lateral view) of the snout and the presence of inflated vestibular apparatuses on either side of the occipital condyles that superficially resemble tympanic bullae; these apparatuses are not present in *T. taoensis*.

Snout Region

Snout Shape The snout of *T. taoensis*, relative to those of other multituberculates, is short and broad, although the anterior extension of the premaxilla revealed by DMNH EPV.136300 (Fig. 6) changes these proportions somewhat relative to earlier reconstructions (e.g., contrast dorsal views by Broom 1914: fig. 6; Granger and Simpson 1929: fig. 5A with that of the revised reconstruction in Fig. 10a). The strongest contrast in snout shape is with the long, narrow, tapered snouts of the European Late Cretaceous kogaionids (see Csiki-Sava et al. 2018: suppl. fig. 8D–F for dorsal reconstructions of *Kogaionon*, *Barbatodon*, and *Litovoi*). *Taeniolabis* and its close relative *Lambdopsalis* (Miao 1988: fig. 12) are noteworthy in that the sides of the snout, in dorsal view, are relatively parallel and are distinctively set off from the rest of the cranium by strong indentations at the roots of the zygomatic arches. The latter feature is also seen in at least some of the kogaionids, most notably in *Kogaionon* (Csiki-Sava et al. 2018: suppl. fig. 8D). A strong indentation is also apparent on an incomplete maxilla (UALVP 28212) of the basal taeniolabidoid *Valenopsalis* illustrated by Fox (2005: pl. 6, fig. 11). By contrast, the snouts of the ptilodontoids *Ptilodus* (Simpson 1937b: fig. 5), *Ectypodus* (Sloan 1979; fig. 1; Gingerich et al. 1983; fig. 2A), and *Filikomys* (Weaver et al. 2021: fig. 1, Extended Data fig. 4) and a variety of djadochtatherioids (see Wible et al. 2019: fig. 23) have a much smoother transition in this region whereas those of the microcosmodontid *Microcosmodon* (Fox 2005: pl. 1, figs. 1, 2), the eucosmodontid *Stygimys* (Sloan and Van Valen 1965: fig. 4), and the cimolomyid

Meniscoessus (Archibald 1982: fig. 27a) seem to be intermediate in this regard.

Bony Composition of Snout The snout of *T. taoensis* receives contributions from the nasals, premaxillae, and maxillae only. Despite the report of a septomaxilla in a specimen (V.J. 451–155) of the paulchoffatiid *Pseudobolodon* by Hahn and Hahn (1994), this could not be confirmed by Wible and Rougier (2000) or Rougier et al. (2016); as such, this element appears to be absent in all multituberculates, and we confirm its absence in *T. taoensis* as well.

There is also no evidence for facial exposure of the lacrimal in *Taeniolabis*; indeed, the bone appears to be entirely absent (Fig. 12), as has also been reported for the lambdopsalid *Lambdopsalis* (Miao 1988). The lack of facial exposure on the snout in taeniolabidoids stands in contrast to the condition in djadochtatherioids, which have a prominent, generally subrectangular facial exposure of the lacrimal, consistently articulating with the maxilla anteroventrally, the nasal anteromedially, and the frontal posterolaterally (Wible et al. 2019: fig. 23D–K). Extensive facial exposure of the lacrimal is also apparently present in the eobaatarid *Sinobaatar* (Hu and Wang 2002; Kusuhashi et al. 2009) and in the cimolomyid *Meniscoessus* (Weil and Tomida 2001). The lacrimal in the stem taeniolabidoid *Yubaatar* is reported to have "a narrow exposure on the skull roof" (Xu et al. 2015: 6) and, although not reconstructed as present in the kogaionid *Barbatodon* by Smith and Codrea (2015: fig. 2N, O), Csiki-Sava et al. (2018: suppl. appendix p. 49) scored the facial process of the lacrimal as "very small and arcuate" in both *Barbatodon* and *Litovoi* (although it was not depicted in their cranial reconstructions of the two genera [suppl. fig. 8E, F]). A facial process of the lacrimal was also not reconstructed for *Kogaionon* by either Kielan-Jaworowska et al. (2004: fig. 8.42A1) or Csiki-Sava et al. (2018: suppl. fig. 8D). As such, the condition in kogaionids is unclear. Simpson (1937b: 740) stated that "there is no suggestion of facial exposure of a lacrimal" in the ptilodontid *Ptilodus* and depicted it as absent (figs. 4, 5) and yet it was scored as "small and arcuate" by Kielan-Jaworowska and Hurum (2001) and subsequent workers; this appears to be in error. Presence of the lacrimal on the face was indicated as "uncertain" in the microcosmodontid *Microcosmodon* (Fox 2005: 15), and it is not depicted in the drawings of the neoplagiaulacid *Ectypodus* by Sloan (1979: fig. 1) and Gingerich et al. (1983: fig. 2A). Concerning relatively early-branching forms, Kielan-Jaworowska et al. (2004: 266) stated that, although the lacrimal was reconstructed as small in paulchoffatiids by Hahn (1969, 1978b), it is "very poorly preserved, and one cannot depend on the reliability of this reconstruction." This may be underscored by the fact that Simmons (1993: char. 55) scored the facial process of the lacrimal in *Paulchoffatia* (now *Meketichoffatia*; Hahn 1993) as "large." Mao et al. (2016: char. 93; and derivative character matrices) scored a facial process of the lacrimal as "large, roughly rectangular" in the paulchoffatiid *Rugosodon* but its condition appears to be unknown (Yuan et al. 2013). In conclusion, given the complete absence of the facial process of the jugal in *Lambdopsalis*, *Taeniolabis*, and *Ptilodus* (and possibly other forms), it appears that the character states frequently used to describe facial exposure of the lacrimal should be separated into two characters, with the first documenting presence versus absence and the second documenting size and shape ("small and arcuate" versus "large and roughly rectangular").

The nasal bones of *Taeniolabis* are very large, both broad and long, and are not confined to the roof of the snout; instead, they extend well posterior to the anterior margins of the orbit. In all other cimolodontan multituberculates except *Lambdopsalis* (Miao 1988: fig. 12), *Yubaatar* (Xu et al. 2015: fig. 3b), and perhaps *Ectypodus* (Sloan 1979: fig. 1), the posterior margin of the nasals lies level with or anterior to the anterior margin of the orbitotemporal fenestra.

The facial (posterodorsal) process of the premaxilla in *Taeniolabis* does not insert between the nasal and the maxilla as sharply as it does in most djadochtatherioids (*Sloanbaatar* being a possible exception; see Wible et al. 2019: fig. 21) and at least some kogaionids (*Barbatodon* and *Litovoi*; Csiki-Sava et al. 2018: suppl. fig. 8E, F). Relative to other multituberculates, the premaxilla in *Taeniolabis* houses a massive central incisor (I2), which has been related to an enhanced gnawing function and concomitant reduction of shearing lower premolars (e.g., Simpson 1937a; Bohlin 1945; Gambaryan and Kielan-Jaworowska 1995; Weil and Krause 2008; Weaver and Wilson 2020).

The facial process of the maxilla in *Taeniolabis* is unremarkable other than the fact that it contributes, in the absence of a facial process of the lacrimal, to the entire anterior orbital rim. It does not exhibit the lateral bulging described for djadochtatherioids such as *Catopsbaatar*, *Djadochtatherium*, *Kryptobaatar*, *Mangasbaatar*, and *Tombaatar*, a condition that Rougier et al. (2016) and Wible et al. (2019) attributed to possession of an enlarged maxillary sinus.

Tip of Snout and External Nasal Aperture The external nasal aperture of *T. taoensis*, although not illustrated previously in anterior view, is profoundly different than previously known, primarily because of the presence, as revealed by DMNH EPV.136300 (Fig. 6a–e), of a prominent internarial process on the premaxilla and more anteriorly extended nasals (Fig. 10a–d). Although the dorsal ends of the left and right internarial processes are not preserved in DMNH EPV.136300, we tentatively infer from their shape that they ended in blunt tips (much as in the gondwanatherian *Vintana* see Krause 2014a: fig. 1d; 2014b: fig. 5B, C, the

marsupialiform *Didelphodon* see Wilson et al. 2016: fig. 1a, b, d, f, g, h), or the "Gurlin Tsav deltatheroidan" Szalay and Trofimov 1996: fig. 22; G. Rougier, pers. comm.) and did not extend posterodorsally to insert between the anterior ends of the left and right nasals, for which we do not see direct evidence in the form of sutures near the midline.

An internarial bar, formed by a complete internarial process (variously also called the internasal, prenasal, dorsal, or ascending process) dividing the external nasal aperture into left and right halves is found in tetrapods ancestrally and, despite being rarely preserved in fossils, is known to have been retained in a variety of non-mammaliamorph cynodonts (e.g., *Beishanodon*, *Dadadon*, *Galesaurus*, *Menadon*, *Riograndia*, tritylodontids) as well as in some early-branching mammaliamorphs such as *Sinoconodon*, *Morganucodon*, *Hadrocodium*, *Haldanodon*, *Necrolestes*, and probably *Docodon* (Kemp 1982; Hopson and Barghusen 1986; Rowe 1986, 1988; Sues 1986; Lillegraven and Krusat 1991; Flynn et al. 2000; Wible and Rougier 2000, 2017; Bonaparte et al. 2001; Luo et al. 2001; Kammerer et al. 2008; Gao et al. 2010; Rougier et al. 2015; Pusch et al. 2019). Rowe (1988: 251) declared the internarial process to be "absent in adult Monotremata, Multituberculata, and Theria, rendering the external nares confluent in postnatal ontogeny."

Miao (1988), however, inferred the presence in *Lambdopsalis* of an internarial process on each premaxilla that extended posterodorsally to insert between the anterior ends of the left and right nasals, thus forming an internarial bar and dividing the external nares. Although not completely preserved on any specimen, Miao's evidence included, in addition to internarial processes projecting dorsally at the anterior ends of the palatal processes of the premaxillae between the left and right I2s, a triangular piece of bone (or the suture for it) insinuated between the anterior ends of the left and right nasals in four specimens. He identified these triangular pieces of bone as premaxillae and inferred that they were dorsal (and posterior) extensions of the internarial processes. He also suggested that an internarial bar may have been present in *Chulsanbaatar*. Hurum (1994) found no evidence for an internarial process in *Chulsanbaatar* (or *Nemegtbaatar*). Wible and Rougier (2000) also concluded that there was no evidence for an internarial bar in *Chulsanbaatar*, nor, in fact, in the more plesiomorphic paulchoffatiids *Pseudobolodon* and *Kuehneodon*. They also expressed doubt about its existence in *Lambdopsalis*, noting that the specimens of *Lambdopsalis* purported to preserve an internarial process insinuated between the nasals are quite different between specimens in this regard and that the "process" may simply be broken parts of the nasals. We share these doubts.

Nasal Foramina *Taeniolabis*, as revealed by UCMP 98083 (Fig. 8), possesses nasal foramina that are asymmetrically developed in number and position. Krause et al. (2014b) summarized the occurrence of nasal foramina in multituberculates: present in the paulchoffatiid *Pseudobolodon* (but not *Kuehneodon*); the "plagiaulacidan" *Glirodon*; the djadochtatherioids *Catopsbaatar*, *Chulsanbaatar*, *Djadochtatherium*, *Kamptobaatar*, *Kryptobaatar*, *Nemegtbaatar*, *Sloanbaatar*, and *Tombaatar*; the lambdopsalid *Lambdopsalis*; the kogaionid *Kogaionon*; and the ptilodontid *Ptilodus*. Nasal foramina have also been found in the eobaatarid *Sinobaatar* (Kusuhashi et al. 2009: figs. 9, 11), the ptilodontoid *Filikomys* (in a specimen originally attributed to *Cimexomys* by Montellano et al. 2000: fig. 1A), the djadochtatheriids *Mangasbaatar* (Rougier et al. 2016: fig. 19) and *Guibaatar* (Wible et al. 2019: figs. 2, 20A), the kogaionid *Barbatodon* (Smith and Codrea 2015: fig. 2A, although perhaps not as symmetrically portrayed as in the reconstructions in fig. 2N and Csiki-Sava et al. 2018: suppl. fig. 8E), and the stem taeniolabidoid *Yubaatar* (Xu et al. 2015: fig. 3b). The nasal foramina are asymmetrical in some taxa but are more frequently developed in symmetrical pairs. Miao (1988:18) suggested that nasal foramina may be a multituberculate synapomorphy (see also Hurum 1994) but their presence in non-mammaliamorph cynodonts and early-branching mammaliamorphs (e.g., *Sinoconodon*, *Morganucodon*, Kermack et al. 1981; contra scoring in Mao et al. 2016 and derivative character matrices, *Haldanodon*) probably indicates a plesiomorphic condition for multituberculates. Nasal foramina are also known in the gondwanatherians *Vintana* (one on each side) and *Adalatherium* (~10 on each side) (Krause et al. 2014b, 2020b). They are absent in *Cifelliodon* and, to date, have not been recorded in euharamiyidans (Huttenlocker et al. 2018; Krause et al. 2020b).

Infraorbital Foramina *Taeniolabis* has but one infraorbital foramen, completely bounded by the maxilla; in this sense, it is typical of other cimolodontan multituberculates. Multiple infraorbital foramina are not uncommon in Mesozoic mammaliamorphs (see reviews in Krause et al. 2014b, 2020b) and are also present in a range of relatively early-branching multituberculates, including various paulchoffatiids (Hahn 1985; the condition in *Rugosodon*, Yuan et al. 2013 is unknown, contra Mao et al. 2016 and derivative character matrices), the allodontid *Ctenacodon* (Kielan-Jaworowska et al. 1987; Engelmann 2004), the "plagiaulacidan" *Glirodon* (Engelmann and Callison 1999), and the arginbaatarid *Arginbaatar* (Kielan-Jaworowska et al. 1987), thus likely establishing the plesiomorphic condition. Multiple infraorbital foramina have been documented in only a few cimolodontans: *Meniscoessus* (Clemens 1973; Archibald 1982; Weil, pers. comm. in Fox 2005 reported one or two in the genus), *Lambdopsalis* (Miao 1988; usually single but one specimen exhibits two), *Catopsbaatar* (Kielan-Jaworowska

et al. 2005; can have one to three foramina), *Mangasbaatar* (Rougier et al. 2016), *Guibaatar* (Wible et al. 2019), and ?*Liaobaatar* (Kusuhashi et al. 2020).

Bony Palate

Incisor Positions The positions of the upper incisors of *Taeniolabis* (Figs. 6d and 11; Table 5) are similar to those of *Lambdopsalis* (Miao 1988: fig. 18) and *Catopsalis* (Middleton 1982: pl. 1, fig. 3) in that the alveolus for I3 lies almost directly posterior to the much larger one for I2 and is closely approximated to it. In all three forms, I2 is much larger than I3, although the disparity in size is considerably greater in *Taeniolabis*. Furthermore, the alveolus of I3 in *Taeniolabis* and *Lambdopsalis* is positioned just inside of the lateral margin of the premaxilla; in other words, just inside of the premaxillary ridge. By contrast, I3 in djadochtatherioids is well separated from I2 by a very sizable anteroposterior diastema and is positioned well medial to the lateral margin of the premaxilla (Wible et al. 2019: fig. 22D–K); this condition also obtains in the eucosomodontid *Stygimys* (Sloan and Van Valen (1965: fig. 4) and to a slightly lesser degree in the cimolomyid *Meniscoessus* (Archibald 1982: fig. 27). The condition in the ptilodontid *Ptilodus* (Simpson 1937b: fig. 6), the ptilodontoid *Filikomys* (Weaver et al. 2021), and the eobaatarid *Sinobaatar* (Kusuhashi et al. 2009: figs. 5, 10, 12, 14, 15) is different still in that I3 is separated from I2, but not to as great a degree as in djadochtatherioids but greater than in *Taeniolabis* and *Lambdopsalis*, and I3 is positioned at the lateral margin of the premaxilla. I3 is also laterally positioned in the microcosmodontid *Microcosmodon* (Fox 2005: pl. 1, fig. 1; pl. 3, fig. 3) and the kogaionids *Barbatodon* (Smith and Codrea 2015: fig. 2G, O) and *Litovoi* (Csiki-Sava et al. 2018: fig. 1B, C); it is not far separated from I2 in these genera and the size disparity between I2 and I3 appears to be not as great as in other cimolodontans, including *Taeniolabis* and *Lambdopsalis*. The size disparity between I2 and I3 is even less in the lambdopsalid *Sphenopsalis*, in which the two teeth are described as "subequal"; both lie at the margin of the premaxilla (Mao et al. 2016: fig. 3). Whereas I3 lies wholly within the premaxilla in other cimolodontans for which the condition is known, *Sphenopsalis* and *Tombaatar* (Rougier et al. 1997) are unusual in that the posterior part of the alveolus is composed of the maxilla. Finally, I3 in the taeniolabidoid *Prionessus*, although not illustrated, is described as positioned at the lateral margin of the palate and as being much smaller than I2 (Meng et al. 1998).

Incisive Foramina The incisive foramina of *Taeniolabis* are, like those of *Lambdopsalis* (Miao 1988: figs. 3, 18), *Stygimys* (Sloan and Van Valen 1965: fig. 4), *Meniscoessus* (Archibald 1982: fig. 27a; Weil and Tomida 2001), *Microcosmodon* (Fox 2005: pl. 2: fig. 1), and *Prionessus* (Meng et al. 1998; not illustrated), of moderate size, considerably larger than those of djadochtatherioids (Wible et al. 2019: fig. 22D–K; char. 47) but relatively smaller than those of *Ptilodus* (Simpson 1937b: fig. 6) and *Sphenopsalis* (Mao et al. 2016: fig. 3). *Ptilodus* exhibits an associated palatal fossa, which is unknown in non-ptilodontoid cimolodontans (except possibly in the kogaionid *Kogaionon* [Rădulescu and Samson 1996: fig. 1] but it has yet to be well documented), posterior to the incisive foramen. *Ectypodus* has been scored as possessing a large foramen and palatal fossa (Simmons 1993: char. 57; Rougier et al. 1997: char. 57) but the line drawing by Sloan (1979: fig. 1) leaves some of these details unclear. Similarly, the incisive foramina of the ptilodontoid *Filikomys* are scored as present and limited posteriorly by the maxilla but other details (e.g., size, shape, presence/absence of palatal fossae) are lacking (Weaver et al. 2021). Also, the precise size and shape of the incisive foramina in eobaatarids and kogaionids await documentation. Among the genera considered to have incisive foramina of moderate size, the foramina are anteroposteriorly elongate but of variable width, those of *Meniscoessus* and perhaps *Stygimys* (perimeter is fragmentary) being relatively wide compared to those of *Taeniolabis*, *Lambdopsalis*, and *Microcosmodon*.

Digital segmentation of DMNH EPV.136300 has revealed conclusive evidence that the incisive foramina are bounded posteriorly by the maxillae in *Taeniolabis* (Fig. 11). Miao (1988: 5) described the posterior edges of the incisive foramina in *Lambdopsalis* as "close to and anterior to the premaxillo-maxillary suture." This would indicate that the incisive foramina lie entirely within the premaxillae. However, the stereophotographs of IVPP V 5429 provided by Miao (1988: fig. 3) and the reconstruction in his fig. 17, indicate that the posterior boundaries of the incisive foramina in *Lambdopsalis* were probably formed by the maxillae, as scored by Mao et al. (2016), Rougier et al. (2016), Csiki-Sava et al. (2018), and others. The incisive foramen is also bounded posteriorly by the maxilla in the paulchoffatiid *Meketichoffatia* (Hahn 1969: fig. 10), the "plagiaulacidan" *Glirodon* (Engelmann and Callison 1999), the ptilodontid *Ptilodus* (Simpson 1937b: fig. 6), the neoplagiaulacid *Ectypodus* (Sloan 1979: fig. 1), the microcosmodontid *Microcosmodon* (Fox 2005), the cimolomyid *Meniscoessus* (Archibald 1982: fig. 27a), the lambdopsalid *Sphenopsalis* (Mao et al. 2016: fig. 3), the eucosmodontid *Stygimys* (Sloan and Van Valen 1965: fig. 4), the kogaionids *Litovoi* and *Kogaionon* (Csiki-Sava et al. 2018: char. 95), and all djadochtatherioids except perhaps *Catopsbaatar* and *Sloanbaatar*. The condition in both *Catopsbaatar* and *Sloanbaatar* seems unclear. The premaxillary-maxillary suture in *Catopsbaatar* is described as actually reaching the incisive foramen and extending "transversely along its posterior boundary" (Kielan-Jaworowska et al. 2005: 494), suggesting that the maxilla potentially forms the posterior border of the incisive foramen; the foramen (labeled as its synonym, the 'palatine fissure') is illustrated in stereo-photographs (fig. 4E) and appears to be

as described. However, the incisive foramen is consistently reconstructed as anterior to the suture (Kielan-Jaworowska and Sloan 1979: fig. 1B; Kielan-Jaworowska and Hurum 1997: fig. 11I; Kielan-Jaworowska et al. 2004: fig. 8.38I, 2005: fig. 8) and is scored by various workers as lying entirely within the premaxilla (e.g., Kielan-Jaworowska and Hurum 2001; Rougier et al. 2016; Csiki-Sava et al. 2018; Weaver et al. 2021). The situation in *Sloanbaatar* is also not clear. Kielan-Jaworowska (1971: 20) states that the premaxillary-maxillary suture "almost reaches the palatine fissure," which, as explained by Wible and Rougier (2000), is another term for the incisive foramen. Curiously, however, Kielan-Jaworowska (1971: 25) also states that the "incisive foramen is absent" (in both *Sloanbaatar* and *Kamptobaatar*). Also, whereas Kielan-Jaworowska (1971: fig. 9; see also Kielan-Jaworowska and Hurum 1997: fig. 11F; Kielan-Jaworowska et al. 2004: fig. 8.38F) illustrates the palatine fissure immediately anterior to the premaxillary-maxillary suture, Wible et al. (2019: fig. 22F) appear to illustrate the suture intersecting the posterior border of the foramen. This perhaps suggests that there is not conclusive evidence for any multituberculate possessing an incisive foramen lying entirely within the premaxilla although we must emphasize that we have not observed the relevant specimens of either *Catopsbaatar* or *Sloanbaatar* firsthand. Finally, the incisive foramen of *Sphenopsalis* is unusual in not only being large but in being bounded almost entirely by the maxilla, with only its anterior-most edge formed by the premaxilla (Mao et al. 2016: fig. 3).

Palatal Vacuities Although only a small portion of the palate is preserved in AMNH 16321 (Fig. 7d; Broom 1914: pl. XI), palatal vacuities have been scored as absent in *Taeniolabis* by several authors (e.g., Simmons 1993; Rougier et al. 1997, 2016; Kielan-Jaworowska and Hurum 2001; Mao et al. 2016; Csiki-Sava et al. 2018), presumably based on the reconstruction and statements by Granger and Simpson (1929: fig. 6), but as unknown by Wible et al. (2019). The more complete palatal material from Corral Bluffs (DMNH EPV.95284, Fig. 4d; DMNH EPV.134082, Fig. 5d; DMNH EPV.136300, Fig. 6d) conclusively confirms their absence.

In addition to *Taeniolabis*, palatal vacuities are, or appear to be, absent in the paulchoffatiids *Meketichoffatia* (Hahn 1969: Fig. 9) and *Kuehneodon* (Hahn 1969: fig. 20a), the "plagiaulacidan" *Glirodon* (Engelmann and Callison 1999: figs. 14, 15), the eobaatarid *Sinobaatar* (Kusuhashi et al. 2009), the lambdopsalids *Lambdopsalis* (Miao 1988: figs. 3, 13, 18) and *Sphenopsalis* (Mao et al. 2016), the ?taeniolabidoid *Prionessus* (Matthew et al. 1928), the microcosmodontid *Microcosmodon* (Fox 2005: pl. 1, fig. 1), the kogaionid *Kogaionon* (Rădulescu and Samson 1996: fig. 1), and the djadochtatherioids *Catopsbaatar* (Kielan-Jaworowska et al. 2005: figs. 1–5, 8), *Chulsanbaatar* (Kielan-Jaworowska 1974: fig. 5), *Kamptobaatar* (Kielan-Jaworowska 1970a: pl. XVI, fig. 1e), *Kryptobaatar* (initially reported as present by Kielan-Jaworowska 1970a but later shown to be absent by Kielan-Jaworowska and Dashzeveg 1978; see also Smith et al. 2001; fig. 5; Wible and Rougier 2000: figs. 4, 15, 34; Rougier et al. 2016: fig. 26), *Mangasbaatar* (Rougier et al. 2016: figs. 3–5, 17, 20), *Tombaatar* (Rougier et al. 1997: figs. 1, 4), and probably *Guibaatar* (Wible et al. 2019: fig. 20). *Pentacosomodon* was scored as lacking palatal vacuities by Mao et al. (2016) but we know of no specimen that documents this condition.

Palatal vacuities have been described, scored, and/or illustrated in a number of cimolodontan multituberculates, including the ptilodontid *Ptilodus* (Simpson 1937b: fig. 6), the neoplagiaulacid *Ectypodus* (Sloan 1979: fig. 1), the ptilodontoid *Filikomys* (Weaver et al. 2021), the eucosmodontid *Stygimys* (Sloan and Van Valen 1965: fig. 4), the cimolomyids *Meniscoessus* (Archibald 1982: fig. 27a) and possibly *Essonodon* (Archibald 1982: fig. 32), the stem taeniolabidoid *Yubaatar* (Xu et al. 2015: fig. 3a), and several djadochtatherioids: *Bulganbaatar* (Kielan-Jaworowska 1974: fig. 4a), *Nemegtbaatar* (Kielan-Jaworowska 1974: fig. 4b), and *Sloanbaatar* (Kielan-Jaworowska 1970a: pl. XII, fig. 2b), with the latter purportedly having two pairs of vacuities. Two pairs are mistakenly scored for *Meniscoessus*, *Nemegtbaatar*, and *Stygimys* by Mao et al. (2016; and derivative character matrices); it appears that the choanal opening was interpreted as the anterior rim of a second set of vacuities in these cases, as well as possibly in *Yubaatar*, which was described as having only one pair but scored as polymorphic with one or two pairs (Xu et al. 2015: char. 81).

Postpalatine Torus A postpalatine torus is variably developed as a ventrally projecting bulge or distinctive, raised plate at the posterior ends of the palatine bones in several Late Cretaceous djadochtatherioids (e.g., *Catopsbaatar*, *Chulsanbaatar*, *Guibaatar*, *Kamptobaatar*, *Kryptobaatar*, *Mangasbaatar*, *Nemegtbaatar*, *Sloanbaatar*, *Tombaatar* — see Rougier et al. 2016: char. 44 [*Nessovbaatar* was scored as possessing a postpalatine torus but this was presumably in error because the taxon is not yet represented by cranial material]; Wible et al. 2019: chars. 49, 50). A postpalatine torus has also been identified in the microcosmodontid *Microcosmodon* (Fox 2005: pl. 1, fig. 1) as well as in the kogaionids *Kogaionon* (Rădulescu and Samson 1996: fig. 1) and *Litovoi* (Csiki-Sava et al. 2018) but not described or illustrated in detail; none is mentioned for *Barbatodon* (Smith and Codrea 2015). In contrast, a postpalatine torus is not described or apparent in the illustrations for *Ptilodus* (Simpson 1937b: fig. 6) or *Meniscoessus* (Archibald 1982: fig. 27a). Illustration of the palatal surface of *Ectypodus* by Sloan (1979: fig. 1) leaves presence or absence of a torus ambiguous. There is variability in how this character

is coded, and how it is scored for some taxa, but it was scored as "absent or very faint" by Rougier et al. (2016) and as "absent" by Wible et al. (2019) in both *Taeniolabis* and *Lambdopsalis*. The Corral Bluffs material (DMNH EPV.95284, fig. 4d; DMNH EPV.134082, fig. 5d), even with poor surface preservation, confirms that a postpalatine torus is probably not present in *Taeniolabis*. The condition in *Lambdopsalis*, however, seems uncertain; Miao (1988:38) described the posterior part of the palatine as "greatly thickened into a torus." This does not comport with illustrations in Miao (1988: figs. 3, 13, 14, 18) or with observations of original specimens (Rougier, pers. comm.) and, as a result, the torus was scored as either absent or very faint by Rougier et al. (2016) and Wible et al. (2019).

Zygomatic Arch

Composition The zygomatic arch in *Taeniolabis* and other multituberculates is formed by the zygomatic processes of the maxilla and squamosal, which meet anterior to arch midlength and which are joined along an oblique suture that ascends anterodorsally (Figs. 7a, c, 8b, c and 10a, c, d). A small jugal also contributes to the arch (Figs. 8d and 13), probably overlapping the maxillary-squamosal suture on the medial aspect of the arch (toward the top). Where known, the jugal is reduced to a slender, splint-like element on the medial aspect of the zygomatic arch in multituberculates, buttressing the suture between the zygomatic processes of the maxilla and squamosal (Hopson et al. 1989; but see Fox 2005 for interpretation that the multituberculate 'jugal' is a neomorphic ossification). Although small and rarely preserved, the jugal has been identified in several cimolodontan multituberculates including the Paleogene ptilodontoids *Ptilodus* and *Ectypodus* (Hopson et al. 1989) and the Late Cretaceous djadochtatherioids *Nemegtbaatar*, *Chulsanbaatar*, *Kryptobaatar*, and *Guibaatar* (Kielan-Jaworowska et al. 1986; Hopson et al. 1989; Wible and Rougier 2000; Wible et al. 2019), and possibly in *Catopsbaatar* (Kielan-Jaworowska et al. 2005). Facets for a jugal are also reported in the Late Jurassic paulchoffatiids *Kuehneodon* and *Pseudobolodon* (Hahn 1987; Hopson et al. 1989). Perhaps of most relevance because of phylogenetic position, however, is the discovery of a relatively large, plate-like jugal on the medial aspect of the zygomatic arch (overlapping the zygomatic processes of the maxilla and squamosal) of *Yubaatar* (Xu et al. 2015: fig. 3) from the late Late Cretaceous of China. *Yubaatar* was recovered as the outgroup to Taeniolabididae + Lambdopsalidae by Xu et al. (2015) and Csiki-Sava et al. (2018).

The diminutive size of the jugal in multituberculates contrasts strongly with its much larger size in most other cynodonts and especially with its massive size in the gondwanatherians *Vintana* and *Adalatherium* (Krause et al. 2014a, 2014b, 2020a, 2020b). In *Vintana* it is particularly large, larger than in any known Mesozoic mammaliamorph, primarily because of the presence of a deep, scimitar-like flange. In both forms, the jugal contributes to the anteroventrolateral portion of the orbit and extends posteriorly to a level opposite the posterior margin of the glenoid fossa, but does not contribute to the fossa. Among euharamiyidans, a jugal has been recorded for *Vilevolodon* (Luo et al. 2017: Extended Data fig. 1e), *Maiopatagium* (Meng et al. 2017: Extended Data fig. 3a–d), *Arboroharamiya* (Han et al. 2017: fig. 2), and *Shenshou* (Huttenlocker et al. 2018). In *Vilevolodon* it is long (at least two-thirds the length of the zygoma), extending anteriorly to contact the facial process of the maxilla and forming a part of the anterior orbit and posteriorly to border on, but not contribute to, the glenoid fossa on the squamosal. The jugal in *Maiopatagium* is incomplete posteriorly but reconstructed as also contacting the facial process of the maxilla anteriorly. The jugal of *Arboroharamiya*, although illustrated as present, was neither described nor scored. The jugal of *Shenshou* was scored as being long (Huttenlocker et al. 2018: char. 482).

Zygomatic Ridges Curved ridges on the lateral surfaces of zygomatic arches, marking the boundaries for the origins of various parts of the masseter muscle, are well known in Late Cretaceous Asian djadochtatherioids. Identified as 'zygomatic ridges,' they have been described, illustrated, and/or scored for *Bulganbaatar*, *Catopsbaatar*, *Chulsanbaatar*, *Djadochtatherium*, *Guibaatar*, *Kamptobaatar*, *Kryptobaatar*, *Mangasbaatar*, *Nemegtbaatar*, and *Sloanbaatar* (Kielan-Jaworowska 1971; Simmons 1993; Gambaryan and Kielan-Jaworowska 1995; Rougier et al. 1997; 2016; Wible and Rougier 2000; Smith et al. 2001; Kielan-Jaworowska et al. 2004, 2005; Wible et al. 2019). Three sets of zygomatic ridges were identified by Gambaryan and Kielan-Jaworowska (1995): (1) 'anterior' for attachment of pars anterior of the superficial masseter muscle, (2) 'intermediate' for attachment of pars posterior of the superficial masseter, and (3) the smaller, much less distinct 'posterior' for attachment of pars posterior of the medial masseter. Gambaryan and Kielan-Jaworowska (1995; see also Kielan-Jaworowska et al. 2004, 2005) contended that separation of the origin of the superficial masseter into two parts was unique among mammals and reported evidence (much of it based on published illustrations) for the presence of zygomatic ridges (particularly the anterior ridge) in a host of other multituberculates, including what were then classified as "taeniolabidoids" (in addition to djadochtatherioids, these included *Stygimys*, *Taeniolabis*, *Lambdopsalis*, and *Meniscoessus*) and "plagiaulacoids" (e.g., *Ctenacodon*, *Meketichoffatia*, *Pseudobolodon*, *Monobaatar*, *Arginbaatar*, *Kielanodon*, *Renatodon*, *Glirodon*), as well as ptilodontoids (*Ptilodus*, *Prochetodon*, *Mesodma*, *Ectypodus*, *Parectypodus*) and the kogaionid *Kogaionon*. They therefore argued for the ubiquity and uniqueness of ridges on the lateral (rather than

ventral) aspect of the zygomatic arches of multituberculates and that their presence was an autapomorphy for the entire clade.

A full survey of the zygomatic arches of multituberculates to determine presence or absence of zygomatic ridges was not possible for this study; such a survey, in our opinion, would require firsthand observation of what can be relatively subtle features. Nonetheless, zygomatic ridges appear to be prominent in eucosmodontids, based on published illustrations. A strong anterior zygomatic ridge is depicted in a reconstruction of the maxilla (based on UMVP 1481–1483) of *Stygimys* (Sloan and Van Valen 1965: fig. 4); it begins just above P1 and below the infraorbital foramen and arches posterodorsally onto the zygomatic arch. The anterior edge of a prominent anterior zygomatic ridge also appears to be developed above P2 and below the infraorbital foramen in a fragmentary maxilla (AMNH 16534) of *Eucosmodon* (Granger and Simpson 1929: fig. 17A). Outside of djadochtatherians and eucosmodontids, however, evidence for zygomatic ridges is less clear and somewhat controversial. The ubiquity of these zygomatic ridges on the lateral (rather than the ventral) surface of the zygomatic arches of multituberculates has been questioned by Fox (2005), who contested the observations of Gambaryan and Kielan-Jaworowska (1995) concerning the presence of zygomatic arches in various "plagiaulacoids" (e.g., paulchoffatiids, *Monobaatar*, *Arginbaatar*) and reported their clear absence in several cimolodontans (*Valenopsalis*, *Cimolodon*, *Ptilodus*, *Ectypodus*, *Neoplagiaulax*, *Microcosmodon*) based on firsthand observation of specimens. Examining some of the same illustrations examined by these authors, we have similar reservations and can also confirm that zygomatic ridges, as defined by Gambaryan and Kielan-Jaworowska (1995), are not present in *Taeniolabis* (see sections on "Maxillae" and "Squamosals" above). We therefore tentatively concur with Simmons (1993), Rougier et al. (1997), and Fox (2005) that zygomatic ridges are not ubiquitous among Multituberculata and cannot be regarded as an autapomorphy for the clade, that they are present in only relatively derived multituberculates, and therefore that the absence of zygomatic ridges appears to be the plesiomorphic condition for Multituberculata.

Cranial Roof

Composition The cranium of *T. taoensis* is roofed by the nasals anteriorly, the parietal posteriorly, and the frontals centrally, with some relatively minor dorsolateral contributions by the premaxillae and maxillae anteriorly. This is the only taeniolabidid species for which the composition of the cranial roof is well known. Although all or most of the frontals are likely preserved in one of the cranial fragments comprising the holotype (NMMNH P-69902) of *Kimbetopsalis simmonsae*, sutures are not visible (Williamson et al. 2016: fig. 1). From what is illustrated (Williamson et al. 2016: fig. 1A), there are no obvious differences from the frontals of *T. taoensis*.

The frontals of *Lambdopsalis*, as reconstructed by Miao (1988: fig. 12; see also Wible et al. 2019: fig. 23B) in dorsal view, appear to be very similar to those of *Taeniolabis* in being small and having the same general shape and sutural contacts. The frontals in known specimens of *Sphenopsalis* are incomplete but, in dorsal view, are scored as "deeply inserted between the nasals" anteriorly and appear to be less acutely pointed than in *Taeniolabis* and *Lambdopsalis* posteriorly (Mao et al. 2016: char. 90, fig. 9B). The frontals of *Yubaatar* have a squared anterior process inserted between the nasals and a strongly pointed posterior process that resembles that of *Taeniolabis* and *Lambdopsalis* (Xu et al. 2015: fig. 3b). The mid-portion of the frontal in *Yubaatar* differs from that in *Taeniolabis* and *Lambdopsalis* in that it extends laterally to contribute to the orbital rim (without dorsal overlap from the parietal).

In dorsal view, the frontals of djadochtatherioids have a long anterior process inserted between the nasals (Wible et al. 2019: fig. 23D–K) that is more acutely pointed than the broad, blunt incursion in taeniolabidoids, as represented by *Taeniolabis* (Fig. 10a) and *Lambdopsalis* (Miao 1988: fig. 12), or in the stem taeniolabidoid *Yubaatar* (Xu et al. 2015: fig. 3b). The frontals also appear to be pointed anteriorly in the eobaatarid *Sinobaatar* (Kusuhashi et al. 2009: fig. 11). Ptilodontoids do not appear to have a consistent pattern in this regard. In the ptilodontid *Ptilodus*, the frontals combine to form a short, pointed anterior incursion between the nasals (but the frontonasal suture is more complicated laterally) (Simpson 1937b: fig. 5) whereas in *Ectypodus* it is the nasals that are inserted between the left and right frontals, at least as depicted in a simple outline drawing by Sloan (1979: fig. 1). Kogaionids also exhibit a variable pattern, with *Kogaionon* (Rădulescu and Samson 1996: fig. 1) and *Barbatodon* (Smith and Codrea 2015: fig. 2N) having a mediolaterally more-or-less straight frontal-nasal suture whereas that of *Litovoi* (Csiki-Sava et al. 2018: suppl. figs. 7A, B, 8F) is depicted as gently curved, convex anteriorly.

Posteriorly, the frontals in *Taeniolabis* (Fig. 10a), *Lambdopsalis* (Miao 1988: fig. 12), and *Yubaatar* (Xu et al. 2015: fig. 3b), as well as in the ptilodontoids *Ptilodus* (Simpson 1937b: fig. 5) and *Ectypodus* (Sloan 1979: fig. 1), are posteriorly pointed and inserted deeply into the parietal along the midline. This is also the case reported or depicted for the cimolomyid *Meniscoessus* (Weil and Tomida 2001) and the kogaionids *Barbatodon* (Smith and Codrea 2015: fig. 2N) and *Litovoi* (Csiki-Sava et al. 2018: suppl. figs. 7A, B, 8F); the suture in *Kogaionon* is relatively convoluted and less pointed (Rădulescu and Samson 1997: fig. 1). By contrast, the posterior insertion of the frontals into the parietal

is generally much more rounded, essentially U-shaped, in djadochtatherioids (Wible et al. 2019: fig. 23D–K).

The long process of the parietal that extends forward, lateral to the dorsal exposure of the frontal, to contact the nasal in *Taeniolabis* (Fig. 10a) is also seen in *Lambdopsalis* (Miao 1988: fig. 12), although such contact is less in the latter. Naso-parietal contact was also scored as present in *Yubaatar* by Xu et al. (2015: suppl. info. p. 4, char. 92) but is probably in error because such contact is elsewhere listed as absent (suppl. info. p. 18, char. 92) and their fig. 3b shows the frontal intervening between the two elements. Among cimolodontans, therefore, naso-parietal contact in *Taeniolabis* and *Lambdopsalis* appears to be a unique condition but Wible and Rougier (2000) have also reported such contact in several specimens of the paulchoffatiids *Kuehneodon* and *Pseudobolodon.* It appears to be absent, however, in the "plagiaulacidan" *Glirodon* (Engelmann and Callison 1999: figs. 1, 2).

Postorbital Process Gambaryan and Kielan-Jaworowska (1995: 45) concluded that the postorbital process in multituberculates "is situated on the parietal and the orbit is very large." The position was regarded as different than in most therians in being in a relatively posterior position and not on the frontal (Novacek 1986). There are, however, some exceptions among placental mammals. For instance, some ctenodactyloid rodents bear a postorbital process on the parietal (Wible et al. 2005) and, as noted by Gambaryan and Kielan-Jaworowska (1995) and Wible and Rougier (2000), some hyracoids have a postorbital process that receives contributions from both the frontal and parietal (reviewed by Barrow et al. 2012). Wible and Rougier (2000: 82) elaborated, in part based on more recent discoveries, that there are three positions of the postorbital process in multituberculates: (1) "on the frontal and inconspicuous" (e.g., various paulchoffatiids, *Ptilodus*, *Ectypodus*), (2) "on the parietal and short" (e.g., *Chulsanbaatar*, *Kamptobaatar*, *Nemegtbaatar*), and (3) "on the parietal and long" (e.g., *Catopsbaatar*, *Kryptobaatar*). Rougier et al. (2016) added *Djadochtatherium*, *Mangasbaatar*, and *Tombaatar* to those taxa with long postorbital processes on the parietal. Wible et al. (2019) indicated that the postorbital process was probably on the parietal in *Guibaatar* as well. Weil and Tomida (2001) described the postorbital process of *Meniscoessus* as unique among multituberculates in being comprised of both the frontal and parietal. Despite the relatively far posterior position in multituberculates, Wible and Rougier (2000) presumed (contra Miao 1988), as do we, that the process in multituberculates marks the upper boundary between the orbit and the temporal fenestra, as it does in therians.

The composition of the postorbital process in *Lambdopsalis* has been controversial. Miao (1988) identified it as on the frontal, but lateral to where the parietal meets the nasal. Gambaryan and Kielan-Jaworowska (1995), based on a personal communication from Jin Meng) disagreed, and concluded that it was formed by the parietal. Based on this controversy, Rougier et al. (2016) and Wible et al. (2019) equivocated about the composition of the postorbital process in *Lambdopsalis*. A specimen of *Lambdopsalis* (IVPP V7151.50) reexamined by Mao Fangyuan (personal communication, September 2020) confirms the conclusion that the postorbital process is indeed on the parietal. In addition, she has concluded, based on comparisons with the new material of *Lambdopsalis*, that the postorbital process in specimen IVPP V19029 of *Sphenopsalis* is also on the parietal. This pattern is then comparable to that in *Taeniolabis* (Figs. 4, 7, and 10) and the stem taeniolabidoid *Yubaatar* (Xu et al. 2015: fig. 3b).

Orbit

Bony Composition Composition of the anterior and medial walls of the orbit, as well as the lateral wall of the braincase, remains poorly known for most multituberculates other than djadochtatherioids. The lacrimal contributes to the orbital wall, including the orbital pocket (see below) in those djadochtatherioids for which it has been able to be distinguished (e.g., *Nemegtbaatar* – Hurum 1994; *Kryptobaatar* – Wible and Rougier 2000; *Mangasbaatar* – Rougier et al. 2016; *Guibaatar* – Wible et al. 2019). It is, however, a minor component relative to the frontal and maxilla. Kielan-Jaworowska et al. (2004: 266) stated that "[T]he lacrimal has not been found in any Tertiary multituberculate, including *Ptilodus* (Simpson, 1937a; Krause, 1982a) and *Lambdopsalis* (Miao, 1988)" (contra Crompton et al. 2018: fig. 1). We have concluded the same for *Taeniolabis*; it is absent (see Fig. 12 and "Lacrimals" above). Outside of Djadochtatherioidea, lacrimals have been identified in the Late Cretaceous North American cimolodontans *Meniscoessus* (Weil and Tomida 2001) and *Filikomys* (Weaver et al. 2021: char. 93) but contributions of the element to the orbital wall have not been recorded. Similarly, as elaborated above (see "Bony Composition of Snout"), although facial exposure of the lacrimal is scored as present in kogaionids (Csiki-Sava et al. 2018: char. 93), its condition within the orbit remains unknown. The presence or absence of a lacrimal in the microcosmodontid *Microcosmodon* could not be ascertained (Fox 2005). The Late Cretaceous stem taeniolabidoid *Yubaatar*, however, is reported to have a lacrimal that "occupies the anteromedial corner of the orbit" (Xu et al. 2015: 6).

Whether or not the perpendicular lamina of the palatine contributes to the medial orbital wall is unknown in *Taeniolabis*, simply because the sutures to evaluate the

condition cannot be conclusively discerned in any of the available specimens. Although uncertainty exists, the palatine is thought to be absent from the medial orbital walls of paulchoffatiids (Hahn 1987; Hurum 1994), *Lambdopsalis* (Miao 1988), *Chulsanbaatar* (Hurum 1994), *Tombaatar* (Rougier et al. 1997), *Kryptobaatar* (Wible and Rougier 2000), *Microcosmodon* (Fox 2005), *Catopsbaatar* (Kielan-Jaworowska et al. 2005), *Mangasbaatar* (Rougier et al. 2016), and *Guibaatar* (Wible et al. 2019), seemingly replaced by expansion of the maxilla. The palatine was described or reconstructed as present in the orbits of *Ectypodus* (Sloan 1979), *Kamptobaatar* (Kielan-Jaworowska 1971), and *Nemegtbaatar* (Hurum 1994, 1998a) but its presence in these taxa has been refuted, or at least questioned, by Rougier et al. (1997, 2016), Wible and Rougier (2000), and Wible et al. (2019). *Nemegtbaatar* appears to be the only possible remaining exception but, at the present time, Miao's (1988) hypothesis that the absence of orbital exposure of the palatine is a synapomorphy of Multituberculata appears to remain viable (see also Wible 1991; Crompton et al. 2018).

We tentatively conclude that, lacking definitive evidence for contributions from the lacrimal and palatine to the orbital wall in *Taeniolabis*, the wall, at least anteriorly, was likely composed of only the frontal and maxilla. In addition, the parietal formed a small posterior section of the supraorbital rim by way of the long process that extends forward on the cranial roof, lateral to (and overlapping) the frontal and the posterior end of the nasal, to contact the maxilla.

Position and Size Sloan (1981: fig. 6.14) concluded that the anterior margin of the orbit in *Taeniolabis* was placed too far anteriorly in earlier reconstructions, level with the mesial edge of M1 by Broom (1914: fig. 8) and level with the mesial edge of P4 by Granger and Simpson (1929: fig. 4). Sloan positioned it much farther posteriorly, level with the middle of M1 (see also Wible et al. 2019: fig. 21C). Correspondingly, he also estimated that the orbit was much larger (35 mm in diameter) than reconstructed by earlier workers and thereby suggested nocturnal or crepuscular habits for *Taeniolabis*. Using the distance from the anterior edge of I2 and the anterior edge of P4 as a guide to standardize anteroposterior length, both the left and right sides of DMNH EPV.136300 (Fig. 6a, b) and the left side of DMNH EPV.95284 (Fig. 4a) demonstrate that this posterior shift by Sloan (1981) was probably excessive and that the anterior margin of the orbit lies approximately level with the mesial edge of M1 (see revised position in Fig. 10a–c), the same level as reconstructed by Broom (1914).

Correspondingly, although there is no indication of a postorbital process on the zygomatic arch of *Taeniolabis* (contra Broom 1914: figs. 6, 8; Granger and Simpson 1929: figs. 4, 5A, 6), the presence of a protuberant postorbital process on the parietal sets limits on the posterior border of the eyeball and its associated structures. Sloan (1981: Fig. 6.14) depicted this process as posterior to the level of the distal end of the cheektooth row and also posterior to the posteriormost extent of the maxillary-squamosal suture on the zygomatic arch. This placement is incorrect. DMNH EPV.95284 (Fig. 4), DMNH EPV.134082 (Fig. 5), and AMNH 16321 (Fig. 7) exhibit direct or indirect evidence demonstrating that the postorbital process lies at a level farther anteriorly, opposite M2 (or even the distal end of M1) and opposite the approximate middle of the oblique maxillary-squamosal suture, almost as far anteriorly as originally reconstructed by Granger and Simpson (1929; figs. 4, 5A) but not as far as reconstructed by Broom (1914: fig. 8).

None of the available specimens has a pristinely preserved orbit, the DMNH specimens all exhibiting considerable distortion and AMNH 16321 exhibiting breakage around the periphery of the orbital rims. The least damaged orbit is on the left side of AMNH 16321 (Fig. 7) where the maximum orbital diameter anterior to the postorbital process is only about 25 mm, almost 30% smaller than estimated by Sloan (1981). Based on available evidence, we conclude that the orbit of *Taeniolabis* was farther forward and much smaller than in Sloan (1981: fig. 6.14) reconstruction. In this context, we also agree with Gambaryan and Kielan-Jaworowska's (1995: 65) assessment that the anterior margin of the orbit and the postorbital process are positioned more anteriorly in both *Taeniolabis* (Fig. 10c) and *Lambdopsalis* (Miao 1988: fig. 17) than in djadochtatherioids (Wible et al. 2019: fig. 21D–J).

Orbital Pocket The concept of an "orbital pocket" in multituberculates began with Sloan's (1979) reconstruction of the jaw musculature in the neoplagiaulacid *Ectypodus*. It was seemingly predicated on the observation that there was a space anterior to the eyeball and its adnexa (e.g., extraocular muscles, fat, lacrimal gland, nerves, vessels) that could not have been occupied by those structures, as has also been speculated for the extinct South American marsupialiform Argyrolagidae (Simpson 1970). Sloan (1979: 495) asserted that this pocket, "in front of the orbit and the temporal muscle," was the site of origin for the anterior deep masseter muscle. From his reconstruction (fig. 3B), it is clear that Sloan meant a pocket in front of the eyeball but still within (not in front of) the osseous orbital cavity. But he also appears to have envisioned the muscle overlapping the anterior edge of the eyeball superficially (and the temporalis muscle overlapping the posteroventral edge superficially), which is unlikely. Another difficulty with Sloan's reconstruction, as noted by Gambaryan and Kielan-Jaworowska (1995), is that the eye is placed opposite the postorbital

process rather than anterior to it. Gambaryan and Kielan-Jaworowska (1995) formally designated the orbital pocket (theca orbitalis) and identified it in djadochtatherioids as serving as the origin for pars anterior of the medial masseter muscle (anterior deep masseter muscle of Sloan 1979), which inserted into the masseteric fovea on the dentary.

Kielan-Jaworowska (1971) had earlier identified a fossa in the same general area in the djadochtatherioid *Kamptobaatar*, later named the "orbitonasal fossa" by Kielan-Jaworowska et al. (1986), who speculated that it contained a gland. Rougier et al. (1997) identified the orbital pocket and orbitonasal fossa as the same space (i.e., that the two structures were synonymous) but Gambaryan and Kielan-Jaworowska (1995: 52) indicated that there was both an orbital pocket, containing pars anterior of the medial masseter muscle, and an orbitonasal fossa (found in *Kamptobaatar*, *Sloanbaatar*, and other djadochtatherioids), possibly containing a gland lying "at the posterodorsal end" of the orbital pocket (see also Wible and Rougier 2000; Kielan-Jaworowska et al. 2004).

Gambaryan and Kielan-Jaworowska (1995) indicated that the anterior part of the medial masseter "rarely" originates from the orbital pocket in therian mammals and cited, as the only extant example, bathyergid hystricomorph rodents (blesmols or African mole-rats). Cox and Faulkes (2014) and Cox et al. (2020) identified the masticatory muscle of bathyergids in this region as the infraorbital portion of the zygomaticomandibularis (=pars anterior of the medial masseter of Gambaryan and Kielan-Jaworowska 1995 and other workers but other names have also been applied; see nomenclature in Druzinsky et al. 2011), originating from the anterior wall of the orbit and the zygomatic process of the maxilla. In most bathergyids, the muscle's origin is confined to these areas but in two forms, *Cryptomys* and *Fukomys*, a small slip passes through the infraorbital foramen to originate on the rostrum.

Wible and Rougier (2000) and Wible et al. (2019) reviewed the distribution of the orbital pocket in multituberculates, stating that it had been observed in a number of djadochtherioids (e.g., *Catopsbaatar*, *Chulsanbaatar*, *Guibaatar*, *Kamptobaatar*, *Kryptobaatar*, *Mangasbaatar*, *Nemegtbaatar*, *Sloanbaatar*, and *Tombaatar*) as well as in the neoplagiaulacid *Ectypodus* (Sloan 1979), the taeniolabidid *Taeniolabis* (Sloan 1981), and the lambdopsalid *Lambdopsalis* (Gambaryan and Kielan-Jaworowska 1995: 65; the evidence for its "reduced" existence in *Lambdopsalis* was in the form of a personal communication from Desui Maio). It was stated to be absent in the paulchoffatiids *Meketichoffatia* and *Pseudobolodon* by Wible and Rougier (2000) and none has been reported in the Kogaionidae (Rădulescu and Samson 1997; Smith and Codrea 2015; Csiki-Sava et al. 2018), the microcosmodontid *Microcosmodon* (Fox 2005), the ptilodontid *Ptilodus* (Simpson 1937b; Krause and Wall 1992), or, to our knowledge, any other multituberculate.

Sloan (1981) opined that the space identified as the orbit by Broom (1914) and Granger and Simpson (1929) in *Taeniolabis* is actually the pocket for the origin of the anterior deep masseter muscle (=anterior part of medial masseter=infraorbital part of zygomaticomandibularis). While we cannot rule out the existence of an orbital pocket in *Taeniolabis*, the evidence for one is much less clear than in djadochtatherioids. In djadochtatherioids, this pocket is deep anterodorsally, has a well-developed roof formed by the frontal, lacrimal, and maxilla, is open ventrally, and is demarcated posteriorly by a more-or-less vertical ridge, the orbital ridge on the medial wall. The prominence of the orbital roof is particularly evident in ventral views of the cranium (compare those of the djadochtatherioids with those of the ptilodontoids and taeniolabidoids depicted by Wible et al. 2019: fig. 22). Such a prominent roof is not present in *Taeniolabis* (which does not have a lacrimal) and an orbital ridge cannot be identified in the available sample. We therefore conclude that, if an orbital pocket did exist in *Taeniolabis*, it was much smaller than stated by Sloan (1981) and certainly much smaller and shallower (relatively) than in djadochtatherioids. Whether the orbital cavity, if it existed, contained a muscle of mastication or a gland (other than the lacrimal gland) or both we do not know. Finally, the infraorbital foramen in *Taeniolabis* is of only modest proportions and therefore it seems unlikely that any part of the infraorbital portion of zygomaticomandibularis passed through it, as speculated by Sloan and Van Valen (1965) for *Stygimys* (but see Gambaryan and Kielan-Jaworowska 1995 for contrasting opinion).

Lateral Braincase Wall

Composition Unfortunately, sutures in the lateral braincase wall in the available specimens of *Taeniolabis* cannot be identified, thus rendering moot any possible comparisons concerning relative contributions with other multituberculates. The situation is further exacerbated by the fact that sutures in the lateral wall of the braincase are indeed generally very difficult to identify and poorly known in multituberculates (Kielan-Jaworowska et al. 2004; Crompton et al. 2018).

Foramina Similarly, foramina in the lateral wall of the braincase are exceedingly difficult to discern in the available specimens of *Taeniolabis*, with the exception of a possible foramen (and groove) for the ramus superior of the stapedial artery in DMNH EPV.95284 and UCMP 98083 (?rsf and ?rsg in Figs. 4b and 8b, respectively) and what appears to be a single large foramen for the mandibular

division of the trigeminal nerve in UCMP 98083 (fmV in Fig. 14d). Typically, multituberculates have two foramina for the mandibular division of the trigeminal nerve in the anterior lamina and/or petrosal, which, following Simpson (1937b) and Wible and Rougier (2000), are identified as the foramen ovale inferium and the foramen masticatorium. This is the case for the paulchoffatiids *Kuehneodon* and *Pseudobolodon*, the ptilodontoids *Ptilodus* and *Mesodma*, and the djadochtatherioids *Catopsbaatar*, *Chulsanbaatar*, *Kamptobaatar*, *Kryptobaatar*, *Nemegtbaatar*, *Sloanbaatar*, and cf. *Tombaatar* (Wible and Hopson 1995; Wible and Rougier 2000; Ladevèze et al. 2010). Two foramina are also described for *Lambdopsalis*, but they are said to be in the alisphenoid (Miao 1988). Four foramina are noted for *Mangasbaatar*, of which three are considered to represent the foramen masticatorium (Rougier et al. 2016). The condition in *Taeniolabis* appears to be most similar to *Guibaatar* (Wible et al. 2019), with a single large foramen, although, as has been noted for *Guibaatar,* we cannot exclude the possible presence of a bony bar separating the foramen.

Mesocranium

Ridges and Troughs Posterior to the Choanae Based on descriptions and illustrations in the literature, there appear to be several documented patterns of ridges and troughs in the ventral part of the mesocranium (in the basipharyngeal canal lying posterior to the choanae and anterior to the basioccipital) of multituberculates: (1) the Late Jurassic paulchoffatiid *Pseudobolodon* and the Paleocene ptilodontid *Ptilodus* have paired, longitudinally oriented pterygopalatine ridges (sensu Barghusen 1986) medial to the ventral margin of the alisphenoid and lateral to the vomer, presphenoid, and basisphenoid in the midline, with the resulting lateral pterygopalatine trough being substantially narrower and less deep than the medial trough (Hahn 1981; Wible and Rougier 2000); (2) Late Cretaceous djadochtatherioids such as *Bulganbaatar* (Kielan-Jaworowska 1974), *Catopsbaatar* (Kielan-Jaworowska et al. 2005), *Chulsanbaatar* (Kielan-Jaworowska 1974; Kielan-Jaworowska et al. 1986), *Kamptobaatar* (Kielan-Jaworowska 1970a, 1970b, 1971), Kryptobaatar (Wible and Rougier 2000), and *Nemegtbaatar* (Kielan-Jaworowska 1974; Kielan-Jaworowska et al. 1986) also have a medial and a lateral pterygopalatine trough on each side but they are much more equal in development (Kielan-Jaworowska 1971; Kielan-Jaworowska et al. 1986; Wible and Rougier 2000); (3) the Late Cretaceous djadochtatheriids *Guibaatar* (Wible et al. 2019) and *Mangasbaatar* (Rougier et al. 2016), lacking a prominent vomer in the mesocranium, have only a single medial basipharyngeal channel, bounded by the left and right pterygopalatine ridges; and (4) the Paleocene *Lambdopsalis* does not have pterygopalatine ridges and there is therefore only a single trough between the lateral wall of the basipharyngeal canal and the midline crest formed by the vomer, presphenoid, and basisphenoid (Miao 1988). Although this region is not particularly well preserved and does not show any sutures in any of the specimens of *Taeniolabis*, it appears to resemble the condition in *Lambdopsalis* in this regard. Kielan-Jaworowska (1970b, 1974) and Kielan-Jaworowska and Hurum (1997) have emphasized the significance of the position of the pterygoid bones, medial to the lateral walls of the basipharyngeal canal, as a possible multituberculate synapomorphy but this condition does not appear to apply to *Lambdopsalis* and *Taeniolabis*. Wible and Rougier (2000) and Rougier et al. (2016) discussed possible functions of the pterygopalatine troughs.

Basicranium

Petrosal The promontorium in *Taeniolabis* is tubular, slender, and anteromedially-posterolaterally oriented, as it is in other multituberculates (Miao 1988; Wible and Rougier 2000; Ladevèze et al. 2010; Rougier et al. 2016; Wible et al. 2019). *Taeniolabis* does not appear to bear any distinct grooves for the internal carotid or stapedial arteries on the promontorium, although this might be owing to poor surface preservation. Several multituberculates exhibit a Y-shaped pattern of grooves on the promontorium for the internal carotid artery passing anteriorly and the stapedial artery passing posteriorly toward the fenestra vestibuli. This pattern is clearly identifiable in the djadochtatherioids *Kryptobaatar* (Wible and Rougier 2000), cf. *Tombaatar* (Ladevèze et al. 2010), and *Mangasbaatar* (Rougier et al. 2016), as well as in the ptilodontoid *Ectypodus* (Sloan 1979). In addition, Wible and Hopson (1995) and Kielan-Jaworowska et al. (1986) reconstructed the stapedial artery as crossing the promontorium posterolaterally from the internal carotid artery toward the fenestra vestibuli in *Valenopsalis joyneri* (previously a species of *Catopsalis* – see Williamson et al. 2016). A groove for the proximal stapedial artery is also indicated along the lateral aspect of the promontorium passing toward the fenestra vestibuli in *Litovoi* (Csiki-Sava et al. 2018: fig. S6); a transpromontorial groove for the internal carotid is not illustrated. Miao (1988: 30) described a groove for the stapedial artery "along the lateral side of the promontorium" passing anteromedially from the posteromedial rim of the fenestra vestibuli. In contrast, the transpromontorial groove for the internal carotid artery and the groove for the stapedial artery are absent in *Guibaatar* (Wible et al. 2019). Only a slight indentation on the ventral margin of the fenestra vestibuli as well as the presence of a foramen medial to the crista parotica indicate the presence of the stapedial artery in *Guibaatar*. Absence of a stapedial groove is also noted for paulchoffatiids (Lillegraven and Hahn 1993).

Similar to the condition in other multituberculates, the lateral flange contacts the promontorium medially in *Taeniolabis*; it is however unclear whether the medially inflected lateral flange houses a separate canal for the ramus inferior

of the stapedial artery and/or the post-trigeminal vein. A small foramen is present at the contact between the lateral flange and promontorium, but its course cannot be traced. In most multituberculates, the stapedial artery is reconstructed to branch into a superior ramus, passing through the crista parotica, and an inferior ramus passing anteriorly within the lateral space with the facial nerve (between the lateral flange and promontorium). A canal for the ramus inferior (canal for ?maxillary artery of Kielan-Jaworowska et al. 1986; post-trigeminal canal of Rougier et al. 1996a) within the medially inflected lateral flange has been identified in the ptilodontoid cf. *Mesodma* (Kielan-Jaworowska et al. 1986; Wible and Hopson 1995), the taeniolabidoids cf. "*Catopsalis*/*Valenopsalis*" (Kielan-Jaworowska et al. 1986; Wible and Hopson 1995) and *Lambdopsalis* (Miao 1988), the djadochtatherioid *Kryptobaatar* (Wible and Rougier 2000), and the cimolomyid ?*Meniscoessus* (Luo 1989). In contrast, the ramus inferior and post-trigeminal vein are reconstructed to pass with the facial nerve through the secondary facial foramen endocranially into the cavum supracochleare and cavum epiptericum in *Guibaatar* (Wible et al. 2019).

In addition to variation in pathways for the canal for the ramus inferior, various patterns exist for passage of the ramus superior of the stapedial artery, prootic sinus (tympanic aperture of the prootic canal), and facial nerve (secondary facial foramen) among multituberculates. Several other foramina merge in three different patterns: (1) the prootic canal and ramus superior foramen are confluent (cf. *Mesodma* – Wible and Hopson 1995; cf. "?*Catopsalis*/*Valenopsalis*" – Wible and Hopson 1995; *Kryptobaatar* – Wible and Rougier 2000; *Mangasbaatar* – Rougier et al. 2016), (2) the prootic canal and secondary facial foramen are confluent (cf. *Tombaatar* – Ladevèze et al. 2010), or (3) all are separated (?*Meniscoessus* – Luo 1989; *Chulsanbaatar* – Wible and Rougier 2000; *Guibaatar* – Wible et al. 2019). Because of poor preservation in the available specimens, the pattern is unclear in *Taeniolabis*. The jugular fossa is large in *Taeniolabis*.

The jugular fossa is scored as 'large and deep' in all Djadochtatherioidea for which this feature is known, as well as in *Lambdopsalis* (Rougier et al. 2016; Wible et al. 2019). Although the poor preservation of the *Taeniolabis* specimens prevents a precise reconstruction of the boundaries of the fossa, it is clear that it was likewise large and deep. In contrast, Wible and Rougier (2000) described the jugular fossa as shallow but not necessarily small in the ptilodontoids *Ptilodus* and *Ectypodus*, with it being scored as 'small and shallow' in *Ptilodus* by Rougier et al. (2016) and in the basal multituberculate *Pseudobolodon* by Wible et al. (2019).

The paroccipital process is small and knob-like in *Taeniolabis*, much smaller and less bulbous than speculatively reconstructed by Granger and Simpson (1929: fig. 5B). Miao (1988: 70) described the paroccipital process in *Lambdopsalis* as "distinct" and "rounded" but Wible and Rougier (2000: 94) characterized it as "triangular and posterolaterally expanded." A triangular paroccipital process is noted for *Meketichoffatia* (V.J. 446–155), *Chulsanbaatar*, *Kamptobaatar*, *Kryptobaatar*, *Nemegtbaatar*, and *Sloanbaatar* whereas it is described as finger-like in *Ectypodus*, and as expanded posterolaterally in *Pseudobolodon* (V.J. 450–155) and *Ptilodus* (Wible and Rougier 2000). Similar to their positions in some djadochtatherioids (e.g., *Kryptobaatar* – Wible and Rougier 2000; *Mangasbaatar* – Rougier et al. 2016; *Guibaatar* – Wible et al. 2019), the crista interfenestralis and crista parotica contact the paroccipital process in *Taeniolabis*.

Inner Ear Even with the increasing use of μCT scanning, publications based on virtually reconstructed endocasts of multituberculate inner ears, capable of capturing the external and internal morphology of the petrosal in great detail, are still relatively sparse. The most detailed description based on a μCT scan of the inner ear of the djadochtatherioid cf. *Tombaatar* was published by Ladevèze et al. (2010), but the resolution of the scan and preservation of the specimen left open several questions about morphology. A more recent study by Csiki-Sava et al. (2018: suppl. fig. 6) provided images and a brief description of the inner ear of the kogaionid *Litovoi* but did not provide the detail sufficient for a full comparison with those of other multituberculates. An image of a 3D reconstructed inner ear of the cimolomyid *Meniscoessus* is included in Luo et al. (2016: fig. 6.9), in addition to a description based on low-resolution CT scans by Luo and Ketten (1991), and a published abstract by Weil and Tomida (2017). Conference abstracts based on 3D reconstructed inner ears have also been published for the paulchoffatiid *Pseudobolodon* (Schultz and Martin 2015) and the neoplagiaulacid *Neoplagiaulax* (Kotrappa and Farke 2015). To date, the most detailed descriptions of multituberculate inner ear morphology are based on fragmented petrosal morphology, histological thin sections, or x-ray or low-resolution CT scanning, including those of the closely related taeniolabidoid *Lambdopsalis* (Miao 1988; Meng and Wyss 1995), several paulchoffatiids (Lillegraven and Hahn 1993), the djadochtatherioids *Chulsanbaatar* and *Nemegtbaatar* (Hurum 1998b), and three not further specified multituberculate petrosals from the Hell Creek Formation (Fox and Meng 1997). As such, the inner ear of *Taeniolabis* (Fig. 15), even though not pristinely preserved, provides valuable insight into the inner ear morphology of multituberculates.

All multituberculates known to date exhibit a cochlear canal that is only gently bent laterally, if at all. Impacting a comparison in degree of curvature of the cochlear canal among multituberculates is a paucity of accurate and

comparable measurements. In many cases, comparisons are solely reliant on qualitative descriptions of very small differences in degree of bending. For example, Miao (1988) described the cochlear canal as "straight" in *Lambdopsalis*, confirmed by Luo and Ketten (1991), whereas Meng and Wyss (1995: 142) stated that it "bends slightly laterally." Based on the images provided by Meng and Wyss (1995: fig. 2b), we concur that the cochlear canal appears to slightly bend laterally in *Lambdopsalis*, perhaps a little less so than that in *Taeniolabis* (49°). A "rod-like and straight" morphology was noted by Luo and Ketten (1991: 225) for *Valenopsalis* and ?*Meniscoessus*, but Luo et al. (2016: fig. 6.9) illustrated, with higher-resolution imaging, a slight bending in the 3D reconstruction of the *Meniscoessus* cochlear canal. This is supported by Weil and Tomida (2017), who described the cochlear canal as "curved." A "slightly curved" cochlear canal has also been previously mentioned for *Ptilodus* (Simpson 1937b: 751), the unidentified multituberculates from Hell Creek (Fox and Meng 1997: 274), and cf. *Tombaatar* (Ladevèze et al. 2010: 325). Whether the cochlear canal is straight or slightly bent or variable in djadochtatherioids is uncertain. Hurum (1998b: 83) described the cochlear canal as "straight" in *Nemegtbaatar* and *Chulsanbaatar*, although a very slight lateral bend can be seen in at least *Chulsanbaatar* (ZPal MgM-I/157), but high-resolution µCT reconstructions would be necessary to more accurately measure the degree of curvature in those forms. More recently, the djadochtatheriid *Guibaatar* was described as having a cochlear canal that is "subtly more curved laterally" than in *Nemegtbaatar* and *Chulsanbaatar* (Wible et al. 2019: 293). The degree of curvature is greater in the koigaonid *Litovoi* (76° based on measurements of Csiki-Sava et al. 2018: suppl. fig. 6d) and even greater in the paulchoffatiid *Pseudobolodon* (180°; Schultz and Martin 2015). Although some variation in the degree of curvature of the cochlear canal appears to be present in multituberculates, the cochlear canal appears to be much less curved in multituberculates than in gondwanatherians (210°, Hoffmann and Kirk 2020), basal cladotherians (> 270°, Rougier et al. 1992; Ruf et al. 2009; Luo et al. 2011, 2012; Harper and Rougier 2019), monotremes (> 140°, Schultz et al. 2017), and docodontans (Ruf et al. 2013; Panciroli et al. 2018), but is greater than in the eutriconodontan *Priacodon* and the stem therian Höövör petrosals (Harper and Rougier 2019). The relatively gentle bending of the cochlear canal in some derived multituberculates might be an apomorphic feature of these groups as lateral bending to a greater degree (< 140°) is common in mammaliaforms and appears to also be present in the most basal multituberculates, paulchoffatiids.

The cochlear canal takes up 8.1–9.1% of cranial length in *Taeniolabis* (based on the juvenile specimen UCMP 98083, Fig. 15), which is shorter than in *Lambdopsalis* (13.4%; Meng and Wyss 1995), but comparable in length to *Valenopsalis* (8.1%; Luo and Ketten 1991), ?*Meniscoessus* (7.3%; Luo and Ketten 1991), and the djadochtatherioids *Nemegtbaatar* (6.7%; Hurum 1998b), *Chulsanbaatar* (9.5%; Hurum 1998b), and cf. *Tombaatar* (9.5%; Ladevèze et al. 2010). In comparison to other Mesozoic cynodonts, the cochlear canals in multituberculates are relatively longer compared to cranial length (e.g., 2.6–6.3% of cranial length in basal non-mammalian cynodonts; Graybeal et al. 1989; Luo and Ketten 1991; Luo et al. 1995).

It is unclear whether the cochlear canal in multituberculates contained a lagena macula similar to that of extant monotremes. Several multituberculates exhibit a slightly expanded apex of the cochlear canal but none of them shows any signs of a separate canal for the lagenar nerve. A gentle expansion of the apex is present in *Taeniolabis*. Miao (1988) did not discuss the presence or absence of a lagena in the closely related *Lambdopsalis*, but Meng and Wyss (1995: 142) described the basal part of the cochlear canal as "slightly narrower" than the anterior part; they did not, however, specifically tie this to the presence of a lagena. However, the cochlear canal in *Lambdopsalis* appears to be gently enlarged to a similar degree as in *Taeniolabis* (Meng and Wyss 1995: fig. 2c). In *Valenopsalis* and ?*Meniscoessus*, the apex of the cochlear canal does not appear to be inflated in the reconstructions provided by Luo and Ketten (1991: fig. 3a, b), but Weil and Tomida (2017) noted an inflated apex for *Meniscoessus*, which is corroborated by the reconstruction provided in Luo et al. (2016: fig. 6.10). The early studies by Luo and Ketten (1991) and Luo et al. (1995) employed relatively coarse CT data, which might have not provided the high resolution necessary to detect such an inflation. Presence of a lagena has also been suggested based on apical inflation in one of the unidentified multituberculates (UALVP 26039) from the Hell Creek Formation (but not in UALVP 34144 and UALVP 26037; Fox and Meng 1997), the paulchoffatiid *Pseudobolodon* (Schultz and Martin 2015), the djadochtatherioid cf. *Tombaatar* (Ladevèze et al. 2010), and the kogaionid *Litovoi* (Csiki-Sava et al. 2018), whereas the cochlear canal has been described as straight and not showing "any signs of a lagena" in *Chulsanbaatar* and *Nemegtbaatar* (Hurum 1998b: 83).

Whether a bony support system for the cochlear nerve (e.g., cribriform plate, primary bony lamina, secondary bony lamina, osseous ganglion canal) was present in *Taeniolabis* is uncertain due to poor preservation in the available specimens. The cochlear nerve appears to enter the cochlear canal through a single foramen, but the contrast between the sediment infill and bone is so poor in all of the specimens that it is impossible to differentiate any internal morphology of the cochlear canal. However, presence of a single cochlear foramen would be consistent with other descriptions of multituberculate inner ears. Most multituberculates described to date lack a cribriform plate and the cochlear

nerve enters through a single foramen (e.g., Meng and Wyss 1995; Fox and Meng 1997; Ladevèze et al. 2010; Luo et al. 2016; Csiki-Sava et al. 2018; Wible et al. 2019). In addition, Fox and Meng (1997) described a longitudinal ridge on the inner surface of the lateral wall of the cochlear canal in an unidentified multituberculate (UALVP 26039) from the Hell Creek Formation as marking the most proximal course of the cochlear nerve within the canal. Similarly, a bony primary or secondary lamina is absent in most multituberculates (e.g., Meng and Wyss 1995; Schultz and Martin 2015; Csiki-Sava et al. 2018), although possible fragments within the cochlear canal that could represent bony laminae have been noted for some djadochtatherioids (Hurum 1998b; Ladevèze et al. 2010).

The most prominent feature of the multituberculate inner ear is the enlarged vestibule. The greatest enlargements are seen in *Lambdopsalis*, *Meniscoessus*, *Valenopsalis*, and at least one of the Hell Creek multituberculates, UALVP 26039 (Miao 1988; Luo and Ketten 1991; Meng and Wyss 1995; Fox and Meng 1997; Luo et al. 2016; Weil and Tomida 2017). The vestibule of *Taeniolabis* is also expanded, but not quite to the same degree as in those taxa. In *Lambdopsalis*, the expansion of the vestibule is so great that the endocast of the lateral and even part of that of the posterior semicircular canal are confluent with the endocast of the vestibule; at least the osseous lateral semicircular canal is also confluent with the osseous housing of the vestibule in *Meniscoessus*. This is not the case in *Taeniolabis*; all osseous semicircular canals are free from the vestibule.

A similar degree of inflation is reported in *Neoplagiaulax* (Kotrappa and Farke 2015). The vestibule is even less inflated in Djadochtatherioidea (Hurum 1998b; Ladevèze et al. 2010; Wible et al. 2019), but is still larger than the vestibule of monotremes (Hurum 1998b). The vestibule does not appear to be particularly inflated in paulchoffatiids (Lillegraven and Hahn 1993), the kogaionid *Litovoi* (Csiki-Sava et al. 2018), the ptilodontid *Ptilodus* (Simpson 1937b), and one of the Hell Creek multituberculates, UALVP 34144 (Fox and Meng 1997). Inflated vestibules are not known in any other Mesozoic mammaliaforms.

In most multituberculates, the anterior and posterior semicircular canals fuse to form a crus commune, whereas the lateral and posterior semicircular canals remain separate (i.e., absence of a secondary crus commune). This is at least the case in *Lambdopsalis*, *Meniscoessus*, *Taeniolabis*, and *Nemegtbaatar* (Meng and Wyss 1995; Hurum 1998b; Luo et al. 2016). A very short secondary crus commune is present in cf. *Tombaatar* (Ladevèze et al. 2010) and the lateral semicircular canal is too incomplete in *Litovoi* to assess whether a secondary crus commune is present (Csiki-Sava et al. 2018). The size of the radius of curvature of semicircular canals varies across multituberculates. In *Lambdopsalis*, the lateral semicircular canal is much larger than either the anterior or posterior canal, likely due to the presence of a greatly inflated vestibule (Hurum 1998b). In the paulchoffatiid *Pseudobolodon*, the anterior semicircular canal is much larger than either the posterior or lateral canal (Schultz and Martin 2015), whereas the semicircular canals are fairly similar in size in *Nemegtbaatar* (Hurum 1998b), cf. *Tombaatar* (Ladevèze et al. 2010), and *Taeniolabis*.

Occipital Region

This region is surprisingly poorly known in multituberculates. Kielan-Jaworowska et al. (2004: 268) stated that, with the exception of djadochtatherioids (e.g., *Kamptobaatar* and *Sloanbaatar*, Kielan-Jaworowska 1971; *Kryptobaatar*, Wible and Rougier 2000) and *Lambdopsalis* (see Maio 1988), the occipital plate has not been reconstructed in any other multituberculate. Since then, a partial cranium of the kogaionid *Litovoi* preserving much of the occiput was discovered although few anatomical details were described or illustrated (Csiki-Sava et al. 2018: suppl. fig. 3E). We can now add *Taeniolabis* to the list of multituberculate taxa preserving the occipital region, and some indications of overall proportions but, unfortunately, none of the specimens in our sample allows delineation of sutures between the occipital bone and the other elements that make up the occiput. We are therefore unable to ascertain, for instance, if the parietal contributed to the occipital plate, or if it was restricted to the dorsal cranial roof, as in djadochtatherioids such as *Kamptobaatar*, *Kryptobaatar*, and *Sloanbaatar* (Kielan-Jaworowska 1971; Wible and Rougier 2000), the stem taeniolabidoid *Yubaatar* (Xu et al. 2015), and the lambdopsalid *Lambdopsalis* (Miao 1988). In these forms, the suture between the parietal and the occipital appears to follow, if not bisect, the nuchal crests. In *Mangasbaatar*, the supraoccipital portion of the occipital does not reach the nuchal crest but is very close to it (Rougier et al. 2016). Also, one important distinction between the occipital regions in *Taeniolabis* and *Lambdopsalis* is that, in the former, it is concave (best seen in DMNH EPV.95284 [Fig. 4f] and DMNH EPV.134082 [Fig. 5f]), whereas in the latter, it is strongly convex, a result of the inflated vestibular apparatus (Miao 1988: figs. 12, 17, 18).

No sutures are recognized between the various components of the occipital (supraoccipital, paired exoccipitals, basioccipital) in the adult specimens in our sample of *Taeniolabis*. Intra-occipital synchondroses are generally the earliest among cranial sutures to fuse, at least in extant mammals (e.g., Wilson and Sánchez-Villagra 2009; Goswami et al. 2013; Rager et al. 2014), and are typically fused in multituberculates (Kielan-Jaworowska et al. 1986). Wible and Rougier (2000: fig. 16), however, documented a suture between the exoccipitals and the supraoccipital in one specimen (PSS-MAE 101) of *Kryptobaatar* and Rougier et al. (2016) identified sutures within the occipital bone

in *Mangasbaatar*. Similarly, we see evidence of sutures between the paired exoccipitals and the supraoccipital in the juvenile cranium (UCMP 98083, Fig. 8f) of *T. taoensis*. As for *Kryptobaatar* and *Mangasbaatar*, the supraoccipital of *Taeniolabis* appears to contribute a short, median portion of the dorsal margin of the foramen magnum, as is also the case in most non-mammaliaform cynodonts and fossil and extant mammaliaforms (reviewed in Krause et al. 2014b).

The shape of the foramen magnum in *Taeniolabis* is unusual among multituberculates in being triangular (DMNH EPV.95284, Fig. 4f; DMNH EPV.134082, Fig. 5f), with moderately sharp corners (although those preserved in the juvenile cranium UCMP 98083 appear to be more rounded [Fig. 8f]). By contrast, that of *Lambdopsalis* is described as being an "elongated oval with its greater axis being horizontally placed" (Miao 1988: 84, fig. 28). Those of *Yubaatar* (Xu et al. 2015: fig. 3a) and *Ptilodus* (Broom 1914; fig. 3; Simpson 1937b; fig. 2F) also appear to be evenly rounded. That of *Kryptobaatar* is irregular in shape but also lacks sharp corners and is certainly not triangular (Wible and Rougier 2000: fig. 35). The odontoid notch in *Yubaatar* appears to be U-shaped and deep (Xu et al. 2015: fig. 3a) rather than more V-shaped and relatively shallow as in *Taeniolabis* (Fig. 10b). That of *Ptilodus* is shallower still (Broom 1914; fig. 3; Simpson 1937b; fig. 5). Finally, the occipital condyles of *Taeniolabis* (Fig. 10a–c, e) appear to be less closely spaced than in *Ptilodus* (Simpson, 1937b: fig. 6) and more posteriorly positioned relative to the rest of the occiput than in *Lambdopsalis* (Miao 1988: fig. 18).

Dentary

Direct examination of DMNH EPV.130973 (Fig. 9a–c) and AMNH 16310 (Fig. 9d–f), and indirect evaluation of several AMNH specimens (Fig. 3e–n) from the San Juan Basin through high-resolution photographs, contribute several fundamentally new aspects to our knowledge of dentary morphology in *Taeniolabis taoensis*, most of them pertaining to the ascending ramus. The mandibular condyle is not as large and globular and it is not suspended on a long, posterodorsally directed neck (peduncle), as depicted in previous reconstructions. The coronoid process is intermediate in height relative to some earlier reconstructions and the position of its anterior border is more variable than previously characterized, thus eliminating a feature thought to differentiate *T. taoensis* from *T. lamberti* (see below). We can also establish that a masseteric protuberance is not present in *T. taoensis* (contra Kielan-Jaworowska et al. 2005) but that a masseteric fovea is present in the anterior part of the masseteric fossa.

Among other taeniolabidids, the dentary of the congeneric *T. lamberti* is represented by a single specimen, the holotype (CCM 70–110; Simmons 1987), but is unknown for *Kimbetopsalis simmonsae*, although Williamson et al. (2016) allowed that an edentulous horizontal ramus (AMNH 3030) referred by Sloan (1981) to *Catopsalis foliatus* might possibly be referable to *K. simmonsae* (Lucas et al. 1997 had earlier suggested that AMNH 3030 might belong to *Taeniolabis*). Simmons (1987) contended that the coronoid process in *T. lamberti* arises from lateral to the anterior half of m2 whereas that of *T. taoensis* arises from lateral to the posterior half of m1. The dentaries of *T. taoensis* described above indicate that there is variation in this feature, therefore likely eliminating this character as one that differentiates the two species. In other comparable parts of their anatomy, the dentaries of *T. taoensis* and *T. lamberti* also appear to be very similar, other than the tentative observation by Simmons (1987: 802) that the latter "appears slightly smaller and less massive." Although most comparable measurements of the dentary are not possible, the width of the horizontal ramus below m1 (12.1 mm in CCM 70–110; 14.6 mm in DMNH EPV.130973; 14.9 mm in AMNH 16310) and the relative lengths of the cheektooth row (34.1 mm in CCM 70–110, Simmons 1987, 36.5 mm in DMNH EPV.130973, 38.2 mm in AMNH 16310) support this observation.

In the sister group of taeniolabidids, the lambdopsalids, consisting of *Lambdopsalis bulla* and *Sphenopsalis nobilis*, the dentary is well known in the former (Miao 1986: fig. 7; 1988: figs. 4, 26, 31, 32). The horizontal ramus of the dentary of *L. bulla* resembles that of *T. taoensis* in a number of features but is generally more slender, does not exhibit strong divisions within the masseteric fossa, and the mental foramen is more anteriorly positioned. The ascending ramus of *L. bulla*, however, is very different from that of *T. taoensis* in the following features: (1) longer condylar neck; (2) relatively larger and more posteriorly (rather than posterodorsally) directed condyle; (3) more deeply incised mandibular notch; and (4) lower, more reclined coronoid process. Finally, the ventral margin of the dentary in *L. bulla*, although broad and strongly tilted (Miao 1988: fig. 4) is straighter (less sinuous) than that of *T. taoensis* in lateral view.

In the only other currently accepted lambdopsalid, *Sphenopsalis nobilis*, the dentary is represented only by a few fragments (Mao et al. 2016). Of the fragments illustrated in Mao et al. (2016: figs. 6, 7), there is nothing that would conclusively distinguish *S. nobilis* from *T. taoensis* in dentary morphology but Mao et al. (2016: 438) refer to the presence of "a long condylar process that continues posteriorly to the mandibular condyle" and a "bulbous" condyle in the former, both of which are not present in *T. taoensis*.

In *Prionessus*, a genus whose inclusion in Lambdopsalidae is debated (Xu et al. 2015; Mao et al. 2016; Scott et al. 2016; Williamson et al. 2016; Csiki-Sava et al. 2018), the dentary is represented by an edentulous, fragmentary specimen (the holotype, AMNH 20423 – Matthew and Granger 1925: fig. 6), an even more fragmentary specimen preserving m1–2 (AMNH 21710 – Matthew et al. 1928: fig. 1), and most of a horizontal

ramus bearing i1, p4, m1–2 (IVPP 11132 – Meng et al. 1998: fig. 3b). Little can be gleaned from the illustrations of these specimens that would serve to differentiate them from the dentary of *T. taoensis*, except perhaps that the dentary of *Prionessus* is more gracile, with a ventral border that is more sinuous, and a diastema that is less strongly concave dorsally.

Among taeniolabidoids outside of taeniolabidids and lambdopsalids, the dentary is known in the controversial genus *Catopsalis*, which is generally recognized to be not monophyletic (e.g., Simmons and Miao 1986; Williamson et al. 2016). Although *C. calgariensis* (see Russell 1926; Simpson 1927; Middleton 1982; Higgins 2003), *C. waddleae* (see Buckley 1995; Johnston and Fox 1984), and *C. kakwa* (see Scott et al. 2016) are only known from isolated teeth, the dentary is at least partially known in specimens of *C. alexanderi*, *C. fissidens*, and *C. foliatus*. Concerning the dentary of *C. alexanderi*, Middleton (1982: 1201) stated, "Granger and Simpson (1929: p. 611) description of the mandible of *Taeniolabis* would serve equally well for *C. alexanderi*. The jaw is not quite as robust; the masseteric fossa not as sharply defined anteriorly." In addition to these observations, it appears (see Middleton 1982: pl. 1, figs. 1, 2, 4) that the anterior limit of the masseteric fossa lies opposite the embrasure between m1 and m2 rather than below p4 as in *T. taoensis*. Furthermore, although much of the posterior and dorsal portions of the ascending ramus are not preserved, it appears that the mandibular condyle is not suspended by a long neck, as is also the case in *T. taoensis*, but that the posteroventral margin is less rounded and the ventral margin is straighter (less sinuous) than in *T. taoensis* (see also Kielan-Jaworowska and Sloan 1979: fig. 2D).

A robust dentary fragment of *Catopsalis foliatus* (AMNH 3035) containing p4, m1–2 and illustrated by Granger and Simpson (1929: fig. 10; see also Matthew 1937: fig. 75, Kielan-Jaworowska and Sloan 1979: fig. 2E, Lucas et al. 1997: figs. 2–1, 3–2) in medial view, reveals little other than the deep excavation of the pterygoid fossa posterior to m2 and the flat, tilted (from ventrolateral to dorsomedial) ventral surface below the anterior portion of the pterygoid fossa. In these features, it closely resembles the dentary of *T. taoensis*. Although fragments of the dentary of *C. fissidens* are known (Granger and Simpson 1929; Lucas et al. 1997; Williamson et al. 2016), none appear to be sufficiently complete to yield any useful comparative information other than that the anterior border of the coronoid process appears to arise opposite the embrasure between m1 and m2 or just anterior to it (Lucas et al. 1997; fig. 2–9, 10; Williamson et al. 2016; fig. 3D). Even more basal within Taeniolabidoidea is *Valenopsalis joyneri*, previously regarded as a species of *Catopsalis* (Williamson et al. 2016: figs. 4, 5). Unfortunately, dentaries have not been described for this species.

Yubaatar zhongyuanensis is currently regarded as the immediate outgroup to Taeniolabidoidea (Xu et al. 2015; see also Csiki-Sava et al. 2018) and is represented by both dentaries in the holotype and only known specimen. Relative to the dentary of *T. taoensis*, that of *Y. zhongyuanensis* is longer (relative to depth) and more slender, i1 is less erect, the anterior border of the masseteric fossa is farther posterior (below m1 rather than below p4), the coronoid process begins farther posterior (its anterior margin lying opposite m2), and the pterygoid fossa appears to be less deeply excavated (Xu et al. 2015: figs. 2, 4a [mislabeled as part d]). The peduncle for the mandibular condyle, however, is less stalk-like (indeed, it is described as not having a neck) and the condyle is more dorsally directed than in *Lambdopsalis bulla* and, in this regard, more closely resembles the dentaries of *T. taoensis*.

The ventral surface of the dentary in taeniolabidoids appears to be broad, flat, and strongly tilted (from ventrolateral to dorsomedial in coronal section) in the areas below the molars and the pterygoid fossa. This condition is present in at least *Taeniolabis* (Figs. 2h, 3d, h, j, 8h, 9b, e and 10h; Simmons 1987: fig. 4.1) and *Catopsalis* (Kielan-Jaworowska and Sloan 1979: fig. 2E; Lucas et al. 1997: fig. 3.1, 3.2, 3.5) and, seemingly, in *Lambdopsalis* (Miao 1988: figs. 26, 32) and *Prionessus* (Matthew and Granger 1925: fig. 6) and does not appear to be present, or at least as strongly developed, in other cimolodontan taxa. Earlier-branching forms such as paulchoffatiids (e.g., *Kuhneodon* – Hahn 1969: figs. 17, 18; Hahn 1978a: fig. 10; *Meketibolodon* – Martin 2018: fig. 45) and eobaatarids (e.g., *Sinobaatar* – Kusuhashi et al. 2009: figs. 8, 16) also exhibit a flat ventral surface posteriorly but it appears to be untilted or even tilted in the opposite orientation, from ventromedial to dorsolateral. This may indicate that a broad, flat, and strongly tilted ventral surface of the dentary is a synapomorphy uniting taeniolabidoids although the condition in the stem taeniolabidoid *Yubaatar* is not described or directly illustrated (Xu et al. 2015) and is unknown to us.

More definitively outside of Taeniolabidoidea, the dentaries of other cimolodontans are generally less robust than in *T. taoensis* and, more broadly, Taeniolabidoidea (Wible et al. 2019: fig. 25). Overall morphology is generally quite conservative within Multituberculata, thereby obviating the need for detailed comparison. Outside of Multituberculata, dentaries are also short and robust, with a sizeable diastema, in Gondwanatheria and Euharamiyida (Krause et al. 2020c: fig. 5 A–C, K, L) but generally longer and more slender, without a sizeable diastema in other, early-branching mammaliaform clades (Krause et al. 2020c: fig. 5J, M–X).

Conclusions

The craniomandibular morphology of the iconic early Paleocene multituberculate *Taeniolabis taoensis* is documented in this study on the basis of newly discovered specimens from

the Denver Basin, Colorado, and long-known specimens (both described and undescribed) from the San Juan Basin, New Mexico. All specimens, where possible, were subjected to examination with μCT technology. The specimens from the Denver Basin are the first to be recorded from there and, correspondingly, also establish the approximate base of the Puercan NALMA *Taeniolabis taoensis/Periptychus carinidens* Interval Zone (Pu3) in the basin for the first time.

Early reconstructions of the cranium of *T. taoensis* were based primarily on AMNH 16321, which μCT imaging reveals to be quite fragmentary, possessing major parts of the cranial roof and zygomatic arches but missing many critically important areas of the anterior snout, palate, mesocranium, basicranium, and occipital plate. The material examined in this study reveals profound changes to the shape of the skull relative to early reconstructions (Fig. 10). Some of the more salient differences include a more anteriorly extended premaxillary region; more prominent and more ridge-like sagittal and nuchal crests; pronounced peaks in the regions where the sagittal crest and temporal ridges intersect as well as where the sagittal and nuchal crests intersect; smaller and more laterally positioned incisive foramina; less posteriorly positioned choanae; smaller paraoccipital processes; a triangular foramen magnum; smaller, less bulbous, and more posteriorly situated occipital condyles; and a shorter dentary. The bony composition and features of the lateral wall of the braincase, nasal cavity, and endocranial cavity remain poorly known.

Features previously unknown for *T. taoensis* include the presence of an in situ I3, prominent internarial processes, numerous nasal foramina, a diminutive jugal on the medial aspect of the zygomatic arch, the frontal occupying a substantial portion of the medial wall of the orbit, a posttemporal foramen, and all aspects of the mesocranium, basicranium, and inner ear in the cranium, and a masseteric fovea on the dentary. We also document the absence of a septomaxilla, lacrimal, postpalatine torus, palatal vacuities, zygomatic ridges, and a masseteric protuberance. Reconstruction of the dentary was previously based primarily on AMNH 16310, which was incomplete posteriorly. The dentary specimens described herein add previously unknown details of the ascending ramus, primarily of the masseteric and pterygoid fossae, coronoid process, and mandibular condyle.

Comparison of the craniomandibular morphology of *T. taoensis* with that of other cimolodontan multituberculates confirms that, of those taxa represented by significant skull material, closest resemblances are with the lambdopsalid *Lambdopsalis*.

Acknowledgements First and foremost, we dedicate this contribution to John Wible (Carnegie Museum of Natural History), who has devoted his career to documenting the skull anatomy of mammals, both extinct and extant, and, in so doing, has provided a standard of excellence that is unparalleled. Head of the Class indeed! We thank Norwood Properties, City of Colorado Springs, Waste Management, Aztec Family Raceway, J. Hawkins, J. Hilaire, J. Carner, W. Pendleton, the Bishop family, and H. Kunstle for land access; the Office of the State Archaeologist, State of Colorado, for issuing collection permits; S. Bastien, J. Englehorn, R. Masek, and N. Toth for preparation of specimens; R. Hess, S. Milito, Y. Rollot, P. Sullivan, and K. Weissenburger for field assistance; the USGS National Unmanned Aircraft Systems team for field photography; R. Wicker for specimen photography; M. Leggitt for the drawings in Fig. 10; A. Atuchin for the reconstruction of *T. taoensis* in Fig. 1b; K. MacKenzie and N. Neu-Yagle for collections assistance; L. Weaver for facilitating access to various literature sources; and B. Snellgrove for logistics. We are also grateful to P. Holroyd and M. Goodwin (UCMP) and J. Meng, R. O'Leary, and A. Mellone (AMNH) for access to comparative material (J. Meng went above and beyond in generously providing photographs of several AMNH specimens that became inaccessible during the pandemic); T. Williamson (NMMNH) for supplying photograph of NMMNH P-47645; M. Colbert and J. Maisano (University of Texas – Austin) and M. Hill (AMNH Microscopy and Imaging Facility) for μCT imaging; J. Meng and F. Mao for sharing information on the cranial morphology of *Lambdopsalis* and *Sphenopsalis*; T. Smith and an anonymous reviewer, as well as Guest Editor G. Rougier, for comments that improved the manuscript; and Editor D. Croft for the invitation to participate in this festschrift.

Funding Funding was provided by The Lisa Levin Appel Family Foundation, M. Cleworth, Lyda Hill Philanthropies, the David B. Jones Foundation, M. L. and S. R. Kneller, T. and K. Ryan, and J. R. Tucker as part of the DMNS No Walls Community Initiative.

Data Availability The datasets generated during and/or analyzed during the current study are not publicly available due to ongoing work on taeniolabidoid skull anatomy but are available from the corresponding author on reasonable request.

Declarations

Conflict of Interest The authors declare that they have no competing interest.

References

Adams NF, Rayfield EJ, Cox PG, Cobb SN, Corfe IJ (2019) Functional tests of the competitive exclusion hypothesis for multituberculate extinction. Roy Soc Open Sci 6:181536

Archibald JD (1982) A study of Mammalia and geology across the Cretaceous-Tertiary boundary in Garfield County, Montana. Univ Calif Publ Geol Sci 122:1–286

Archibald JD, Gingerich PD, Lindsay EH, Clemens WA, Krause DW, Rose KD (1987) First North American Land Mammal Ages of the Cenozoic Era. In: Woodburne MO (ed), Cenozoic Mammals of North America: Geochronology and Biostratigraphy. University of California Press, Berkeley, pp 24–76

Barghusen HR (1986) On the evolutionary origin of the therian tensor veli palatini and tensor tympani muscles. In: Hotton N, MacLean PO, Roth JJ, Roth EC (eds), Ecology and Biology of Mammal-like Reptiles. Smithsonian Institution Press, Washington DC, pp 253–262

Barrow EC, Seiffert ER, Simons EL (2012) Cranial morphology of *Thyrohyrax domorictus* (Mammalia, Hyracoidea) from the early Oligocene of Egypt. J Vertebr Paleontol 32:166–179

Benson KP (1998) Floral diversity and paleoclimate of the latest Cretaceous and early Tertiary deposits, Denver Basin, Colorado, USA. Unpublished senior thesis, The Colorado College

Bohlin B (1945) The Jurassic mammals and the origin of the mammalian molar teeth. Bull Geol Inst Uppsala 31:363–388

Bonaparte JF, Ferigolo J, Ribeiro AM (2001) A primitive Late Triassic 'ictidosaur' from Rio Grande do Sul, Brazil. Palaeontology 44:623–635
Broom R (1914) On the structure and affinities of the Multituberculata. Bull Am Mus Nat Hist 33:115–134
Brown RW (1943) Cretaceous-Tertiary boundary in the Denver Basin, Colorado. Bull Geol Soc Am 54:65–86
Buckley GA (1995) The multituberculate *Catopsalis* from the early Paleocene of the Crazy Mountains Basin in Montana. Acta Palaeontol Pol 40:389–398
Butler PM, Hooker JJ (2005) New teeth of allotherian mammals from the English Bathonian, including the earliest multituberculates. Acta Palaeontol Pol 50:185–207
Carlson SJ, Krause DW (1985) Enamel ultrastructure of multituberculate mammals: an investigation of variability. Contrib Mus Paleontol Univ Michigan 27:1–50
Centeno-González NK, Martínez-Cabrera HI, Porras-Múzquiz H, Estrada-Ruiz E (2021) Late Campanian fossil of a legume fruit supports Mexico as a center of Fabaceae radiation. *Commun Biol* 4, 41. https://doi.org/10.1038/s42003-020-01533-9
Cifelli RL, Eberle JJ, Lofgren DL, Lillegraven JA, Clemens WA (2004) Mammalian biochronology of the latest Cretaceous. In: Woodburne MO (ed), Late Cretaceous and Cenozoic Mammals of North America. Columbia University Press, New York, pp 21–42
Clemens WA (1973) Fossil mammals of the type Lance Formation Wyoming. Part III. Eutheria and summary. Univ Calif Publ Geol Sci 94:1–102
Clyde WC, Ramezani J, Johnson KR, Bowring SA, Jones MM (2016) Direct high-precision U–Pb geochronology of the end-Cretaceous extinction and calibration of Paleocene astronomical timescales. Earth Planet Sci Lett 452:272–280
Cope ED (1881) Eocene Plagiaulacidae. Am Nat 15:921–922
Cope ED (1882a) A second genus of Eocene Plagiaulacidae. Am Nat 16:416–417
Cope ED (1882b) A new genus of Taeniodonta. Am Nat 16:604–605
Cope ED (1882c) New marsupials from the Puerco Eocene. Am Nat 16:684–685
Cope ED (1884a) The Tertiary Marsupialia. Am Nat 18:686–697
Cope ED (1884b) The Vertebrata of the Tertiary formations of the West. Rept US Geol Surv Terrs (F. V. Hayden Survey) III:1–1009
Cox PG, Faulkes CG (2014) Digital dissection of the masticatory muscles of the naked mole-rat, *Heterocephalus glaber* (Mammalia, Rodentia). PeerJ 2:e448
Cox PG, Faulkes CG, Bennett NC (2020) Masticatory musculature of the African mole-rats (Rodentia: Bathyergidae). PeerJ 8:e8847
Crompton AW, Musinsky C, Rougier GW, Bhullar B-AS, Miyamae JA (2018) Origin of the lateral wall of the mammalian skull: fossils, monotremes and therians revisited. J Mammal Evol 25:301–313
Csiki Z, Grigorescu D, Rücklin M (2005) A new multituberculate specimen from the Maastrichtian of Pui, Romania and reassessment of affinities of *Barbatodon*. Acta Palaeontol Romaniae 5:73–86
Csiki-Sava Z, Vremir M, Meng J, Brusatte SL, Norell MA (2018) Dome-headed, small-brained island mammal from the Late Cretaceous of Romania. Proc Natl Acad Sci USA 115:4857–4862
Dahlberg EL, Eberle JJ, Sertich JJW, Miller IM (2016) A new earliest Paleocene (Puercan) mammalian fauna from Colorado's Denver Basin, U.S.A. Rocky Mtn Geol 51:1–22
Dawson MR, Constenius KN (2018) Mammalian fauna of the middle Eocene Kishenehn Formation, Middle Fork of the Flathead River, Montana. Ann Carnegie Mus 85:25–60
De Bast E, Smith T (2017) The oldest Cenozoic mammal fauna of Europe: implication of the Hainin reference fauna for mammalian evolution and dispersals during the Paleocene. J Syst Palaeontol 15:741–785
Dechesne M, Raynolds RG, Barkmann PE, Johnson KR (2011) Denver Basin geologic maps: bedrock geology, structure and isopach maps of the Upper Cretaceous through Paleogene strata between Greeley and Colorado Springs, Colorado. Colorado Geological Survey, 1:250,000, 15 maps, 3 cross sections, 35 pp. ISBN 978-1-884216-57-2
Druzinsky RE, Doherty AH, De Vree FL (2011) Mammalian masticatory muscles: homology, nomenclature, and diversification. Integr Comp Biol 51:224–234
Eberle JJ (2003) Puercan mammalian systematics and biostratigraphy in the Denver Formation, Denver Basin, Colorado. Rocky Mtn Geol 38:143–169
Engelmann GF (2004) The anterior dentition of the Late Jurassic multituberculate *Ctenacodon*. Bull Am Mus Nat Hist 285:54–61
Engelmann GF, Callison G (1999) *Glirodon grandis*, a new multituberculate mammal from the Upper Jurassic Morrison Formation. In: Gillette DD (ed), Vertebrate Paleontology in Utah. Utah Geol Surv, Misc Publ 99–1:161–177
Ernst CH, Barbour RW (1989) Turtles of the World. Smithsonian Institution Press, Washington DC
Evans AR, Jones D, Boyer AG, Brown JH, Costa DP, Morgan Ernest SK, Fitzgerald EMG, Fortelius M, Gittleman JL, Hamilton MJ, Harding LE, Lintulaakso K, Lyons SK, Okie JG, Saarinen JJ, Sibly RM, Smith FA, Stephens PR, Theodor JM, Uhen MD (2012) The maximum rate of mammal evolution. Proc Natl Acad Sci USA 109:4187–4190
Evans AR, Wilson GP, Fortelius M, Jernvall J (2007) High-level similarity of dentitions in carnivorans and rodents. Nature 445:78–81
Flynn JJ, Parrish JM, Rakotosamimanana B, Ranivoharimanana L, Simpson WF, Wyss AR (2000) New traversodontids (Synapsida: Eucynodontia) from the Triassic of Madagasar. J Vertebr Paleontol 20:422–427
Fox RC (2005) Microcosmodontid multituberculates (Allotheria, Mammalia) from the Paleocene and Late Cretaceous of western Canada. Palaeontogr Canadiana 23:1–109
Fox RC, Meng J (1997) An X-radiographic and SEM study of the osseous inner ear of multituberculates and monotremes (Mammalia): implications for mammalian phylogeny and evolution of hearing. Zool J Linn Soc 121:249–291
Fuentes AJ, Clyde WC, Weissenburger K, Bercovici A, Lyson TR, Miller IM, Ramezani J, Isakson V, Schmitz MD, Johnson KR (2019) Constructing a time scale of biotic recovery across the Cretaceous–Paleogene boundary, Corral Bluffs, Denver Basin, Colorado, U.S.A. Rocky Mtn Geol 54:133–153
Gambaryan P, Kielan-Jaworowska Z (1995) Masticatory musculature of Asian taeniolabidoid multituberculate mammals. Acta Palaeontol Pol 40:45–108
Gao K-Q, Fox RC, Zhou C-F, Li DQ (2010) A new nonmammalian eucynodont (Synapsida: Therapsida) from the Triassic of northern Gansu Province, China, and its biostratigraphic and biogeographic implications. Am Mus Novitates 3685:1–25
Gazin CL (1941) Paleocene mammals from the Denver Basin, Colorado. J Wash Acad Sci 31:289–295
Gidley JW (1909) Notes on the fossil mammalian genus *Ptilodus*, with descriptions of new species. Proc US Natl Mus 36:611–626
Gingerich PD, Houde P, Krause DW (1983) A new earliest Tiffanian (late Paleocene) mammalian fauna from Bangtail Plateau, western Crazy Mountain Basin, Montana. J Paleontol 57:957–970
Goswami A, Foley L, Weisbecker V (2013) Patterns and implications of extensive heterochrony in carnivoran cranial suture closure. J Evol Biol 26:1294–1306
Gradstein FM, Ogg JG, Schmitz M, Ogg G (eds) (2012) The Geologic Time Scale 2012. Elsevier, Amsterdam, Boston, 1,176 pp
Granger W, Simpson GG (1929) A revision of the Tertiary Multituberculata. Bull Am Mus Nat Hist 56:601–676
Graybeal A, Rosowski JJ, Ketten DR, Crompton AW (1989) Inner ear structure in *Morganucodon*, an Early Jurassic mammal. Zool J Linn Soc 96:107–117

Greenwald NS (1988) Patterns of tooth eruption and replacement in multituberculate mammals. J Vertebr Paleontol 8:265–277
Gregory WK (1910) The orders of mammals. Bull Am Mus Nat Hist 27:1–524
Gurovich Y (2006) Bio-evolutionary aspects of Mesozoic mammals: description, phylogenetic relationships and evolution of the Gondwanatheria (Late Cretaceous and Paleocene of Gondwana). PhD dissertation, Universidad Nacional de Buenos Aires
Hahn G (1969) Beiträge zur Fauna der Grube Guimarota nr. 3. Die Multituberculata. Palaeontogr Abt A 133:1–100
Hahn G (1978a) Neue Unterkiefer von Multituberculaten aus dem Malm Portugals. Geol Palaeontol 12:177–212
Hahn G (1978b) Die Multituberculata, eine fosille Säugetier-Ordnung. Sonderband Der Naturwissenschaftliche Verein, Hamburg 3:61–95
Hahn G (1981) Zum Bau der Schädel-Basis bei den Paulchoffatiidae (Multituberculata; Ober-Jura). Senckenb. Lethaea 61:227–245
Hahn G (1985) Zum Bau des Infraorbital-Foramens bei den Paulchoffatiidae (Multituberculata, Ober Jura). Berliner geowissenschaftliche Abhandlungen A 60:5–27
Hahn G (1987) Neue Beobachtungen zum Schädel- und Gebiss-Bau des Paulchoffatiidae (Multituberculata, Ober-Jura). Palaeovertebrata 17:155–196
Hahn G (1993) The systematic arrangement of the Paulchoffatiidae (Multituberculata) revisited. Geol Palaeontol 27:201–214
Hahn G, Hahn R (1994) Nachweis des Septomaxillare bei *Pseudobolodon krebsi* n. sp. (Multituberculata) aus dem Malm Portugals. Berliner geowiss Abhandl E 13:9–29
Han G, Mao F, Bi S, Wang Y, Meng J (2017) A Jurassic gliding euharamiyidan mammal with an ear of five auditory bones. Nature 551:451–456
Harper T, Rougier GW (2019) Petrosal morphology and cochlear function in Mesozoic stem therians. PloS One 14:e0209457
Higgins P (2003) A Wyoming succession of Paleocene mammal-bearing localities bracketing the boundary between the Torrejonian and Tiffanian North American Land Mammal 'Ages'. Rocky Mtn Geology 38:247–280
Hoffmann S, Beck RMD, Wible JR, Rougier GW, Krause DW (2020) Phylogenetic placement of *Adalatherium hui* (Mammalia, Gondwanatheria) from the Late Cretaceous of Madagascar: implications for allotherian relationships. In: Krause DW, Hoffmann S (eds), *Adalatherium hui* (Mammalia, Gondwanatheria) from the Late Cretaceous of Madagascar. Soc Vertebr Paleontol Mem 21. J Vertebr Paleontol 40(5, Suppl):213–234
Hoffmann S, Kirk EC (2020) Inner ear morphology of *Adalatherium hui* (Mammalia, Gondwanatheria) from the Late Cretaceous of Madagascar. In: Krause DW, Hoffmann S (eds), *Adalatherium hui* (Mammalia, Gondwanatheria) from the Late Cretaceous of Madagascar. Soc Vertebr Paleontol Mem 21. J Vertebr Paleontol 40(5, Suppl):67–80
Holroyd PA, Hutchison JH (2002) Patterns of geographic variation in latest Cretaceous vertebrates: evidence from the turtle component. Geol Soc Am Spec Pap 361:177–190
Holroyd PA, Wilson GP, Hutchison JH (2014) Temporal changes within the latest Cretaceous and early Paleogene turtle faunas of northeastern Montana. Geol Soc Am Spec Pap 503:299–312
Hopson JA, Barghusen HR (1986) An analysis of therapsid relationships. In: Hotton NH, Maclean PD, Roth JJ, Roth EC (eds) The Ecology and Biology of the Mammal-like Reptiles. Smithsonian Institution Press, Washington DC, pp 83–106
Hopson JA, Kielan-Jaworowska Z, Allin EF (1989) The cryptic jugal of multituberculates. J Vertebr Paleontol 9:201–209
Hu Y, Wang Y (2002) *Sinobaatar* gen. nov.: first multituberculate from the Jehol Biota of Liaoning, northeast China. Chinese Sci Bull 47:933–938
Hurum JH (1994) Snout and orbit of Cretaceous Asian multituberculates studied by serial sections. Acta Palaeontol Pol 39:181–221
Hurum JH (1998a) The braincase of two Late Cretaceous Asian multituberculates studied by serial sections. Acta Palaeontol Pol 43:21–52
Hurum JH (1998b) The inner ear of two Late Cretaceous multituberculate mammals, and its implications for multituberculate hearing. J Mammal Evol 5:65–93
Hurum JH, Presley R, Kielan-Jaworowska Z (1996) The middle ear in multituberculate mammals. Acta Palaeontol Pol 41:253–275
Hutchison JH (1984) Determinate growth in the Baenidae (Testudines): taxonomic, ecologic and stratigraphic significance. J Vertebr Paleontol 3:148–151
Hutchison JH, Holroyd PA (2003) Late Cretaceous and early Paleocene turtles of the Denver Basin, Colorado. Rocky Mtn Geol 38:121–142
Huttenlocker AK, Grossnickle DM, Kirkland JI, Schultz JA, Luo Z-X (2018) Late-surviving stem mammal links the lowermost Cretaceous of North America and Gondwana. Nature 558:108–112
Jenkins SH, Busher PE (1979) *Castor canadensis*. Mammalian Species 120:1–8
Johnson KR, Reynolds ML, Werth KW, Thomasson JR (2003) Overview of the Late Cretaceous, early Paleocene, and early Eocene megafloras of the Denver Basin, Colorado. Rocky Mtn Geol 38:101–120
Johnston PA, Fox RC (1984) Paleocene and Late Cretaceous mammals from Saskatchewan, Canada. Palaeontogr Abt A 186:163–222
Kammerer CF, Flynn JJ, Ranivoharimanana L, Wyss AR (2008) New material of *Menadon besairiei* (Cynodontia: Traversodontidae) from the Triassic of Madagascar. J Vertebr Paleontol 28:445–462
Kemp TS (1982) Mammal-like Reptiles and the Origin of Mammals. Academic Press, London
Kermack DM, Kermack KA (1984) The Evolution of Mammalian Characters. Croom Helm, London
Kermack KA, Mussett F, Rigney HW (1981) The skull of *Morganucodon*. Zool J Linn Soc 71:1–158
Kielan-Jaworowska Z (1970a) New Upper Cretaceous multituberculate genera from Bayn Dzak, Gobi Desert. Results of the Polish-Mongolian Palaeontological Expeditions Part II. Palaeontol Pol 21:35–49
Kielan-Jaworowska Z (1970b) Unknown structures in multituberculate skull. Nature 226:974–976
Kielan-Jaworowska Z (1971) Results of the Polish-Mongolian palaeontological expeditions. Part III. Skull structure and affinities of the Multituberculata. Palaeontol Pol 25:5–41
Kielan-Jaworowska Z (1974) Multituberculate succession in the Late Cretaceous of the Gobi Desert (Mongolia). Results of the Polish-Mongolian Palaeontological Expeditions. Part V. Palaeontologia Polonica 30:23–44
Kielan-Jaworowska Z, Bonaparte JF (1996) Partial dentary of a multituberculate mammal from the Late Cretaceous of Argentina and its taxonomic implications. Revista del Museo Argentino de Ciencias Naturales "Bernardino Rivadavia" 145:1–9
Kielan-Jaworowska Z, Cifelli RL, Luo Z-X (2004) Mammals from the Age of Dinosaurs: Origins, Evolution, and Structure. Columbia University Press, New York
Kielan-Jaworowska Z, Dashzeveg D (1978) New Late Cretaceous mammal locality in Mongolia and a description of a new multituberculate. Acta Palaeontol Pol 23:115–130
Kielan-Jaworowska Z, Dashzeveg D, Trofimov BA (1987) Early Cretaceous multituberculates from Mongolia and a comparison with Late Jurassic forms. Acta Palaeontol Pol 32:3–47
Kielan-Jaworowska Z, Hurum JH (1997) Djadochtatheria – a new suborder of multituberculate mammals. Acta Palaeontol Pol 42:201–242
Kielan-Jaworowska Z, Hurum JH (2001) Phylogeny and systematics of multituberculate mammals. Palaeontology 44:389–429

Kielan-Jaworowska Z, Hurum JH, Lopatin AV (2005) Skull structure in *Catopsbaatar* and the zygomatic ridges in multituberculate mammals. Acta Palaeontol Pol 50:487–512

Kielan-Jaworowska Z, Presley R, Poplin C (1986) The cranial vascular system in taeniolabidoid multituberculate mammals. Phil Trans Roy Soc Lond B 313:525–602

Kielan-Jaworowska Z, Sloan RE (1979) *Catopsalis* (Multituberculata) from Asia and North America and the problem of taeniolabidid dispersal in the Late Cretaceous. Acta Palaeontol Pol 24:187–197

Knowlton FH (1930) The flora of the Denver and associated formations of Colorado. US Geol Surv, Prof Pap 155.

Kondrashov PE, Lucas SG (2015) Paleocene vertebrate faunas of the San Juan Basin, New Mexico. In: Lucas SG, Sullivan RM (eds), Fossil Vertebrates in New Mexico. New Mex Mus Nat Hist and Sci Bull 68:131–148

Kotrappa MS, Farke AA (2015) Anatomy of the endosseous labyrinth in the multituberculate mammal *Neoplagiaulax*. J Vertebr Paleontol, Progr Abstr 2015:158

Koyabu D, Maier W, Sánchez-Villagra RM (2012) Paleontological and developmental evidence resolve the homology and dual embryonic origin of a mammalian skull bone, the interparietal. Proc Natl Acad Sci USA 109:14075–14080

Krause DW (1977) Paleocene multituberculates (Mammalia) of the Roche Percée local fauna, Ravenscrag Formation, Saskatchewan, Canada. Palaeontogr Abt A 159:1–36

Krause DW (1982a) Multituberculates from the Wasatchian Land-Mammal Age, early Eocene, of western North America. J Paleontol 56:271–294

Krause DW (1982b) Jaw movement, dental function, and diet in the Paleocene multituberculate *Ptilodus*. Paleobiology 8:265–281

Krause DW (1986) Competitive exclusion and taxonomic displacement in the fossil record: the case of rodents and multituberculates in North America. In: Flanagan KM, Lillegraven JA (eds), Vertebrates, Phylogeny, and Philosophy: a Tribute to George Gaylord Simpson. Contrib Geol Univ Wyoming Spec Pap 3:95–117

Krause DW, Hoffmann S, Hu Y, Wible JR, Rougier GW, Kirk EC, Groenke JR, Rogers RR, Rossie JB, Schultz JA, Evans A, Koenigswald WV, Rahantarisoa L (2020a) Skeleton of Cretaceous mammal from Madagascar reflects long-term insularity. Nature 581:421–427

Krause DW, Hoffmann S, Rossie JB, Hu Y, Wible JR, Rougier GW, Kirk EC, Groenke JR (2020b) Craniofacial morphology of *Adalatherium hui* (Mammalia, Gondwanatheria) from the Late Cretaceous of Madagascar. In: Krause DW, Hoffmann S (eds), *Adalatherium hui* (Mammalia, Gondwanatheria) from the Late Cretaceous of Madagascar. Soc Vertebr Paleontol Mem 21. J Vertebr Paleontol 40(5, Suppl):19–66

Krause DW, Hoffmann S, Werning S (2017) First postcranial remains of Multituberculata (Allotheria, Mammalia) from Gondwana. Cretaceous Res 80:91–100

Krause DW, Hoffmann S, Wible JR, Kirk EC, Schultz JA, Koenigswald WV, Groenke JR, Rossie JB, O'Connor PM, Seiffert ER, Dumont ER, Holloway WL, Rogers RR, Rahantarisoa LJ, Kemp AD, Andriamialison H (2014a) First cranial remains of gondwanatherian mammal reveal remarkable mosaicism. Nature 515:512–517

Krause DW, Hoffmann S, Wible JR, Rougier GW (2020c) Lower jaw morphology of *Adalatherium hui* (Mammalia, Gondwanatheria) from the Late Cretaceous of Madagascar. In: Krause DW, Hoffmann S (eds), *Adalatherium hui* (Mammalia, Gondwanatheria) from the Late Cretaceous of Madagascar. Soc Vertebr Paleontol Mem 21. J Vertebr Paleontol 40(5, Suppl):81–96

Krause DW, Hu Y, Hoffmann S, Groenke JR, Schultz JA, Evans AR, Koenigswald Wv, Rougier GW (2020d) Dental morphology of *Adalatherium hui* (Mammalia, Gondwanatheria) from the Late Cretaceous of Madagascar. In: Krause DW, Hoffmann S (eds), *Adalatherium hui* (Mammalia, Gondwanatheria) from the Late Cretaceous of Madagascar. Soc Vertebr Paleontol Mem 21. J Vertebr Paleontol 40(5, Suppl):97–132

Krause DW, Kielan-Jaworowska Z (1993) The endocranial cast and encephalization quotient of *Ptilodus* (Multituberculata, Mammalia). Palaeovertebrata 22:99–112

Krause DW, Wall CE (1992) A biomechanical analysis of the masticatory apparatus of *Ptilodus* (Multituberculata). J Vert Paleo 12:172–187

Krause DW, Wible JR, Hoffmann S, Groenke JR, O'Connor PM, Holloway WL, Rossie JB (2014b) Craniofacial morphology of *Vintana sertichi* (Mammalia, Gondwanatheria) from the Late Cretaceous of Madagascar. In: Krause DW (ed), *Vintana sertichi* (Mammalia, Gondwanatheria) from the Late Cretaceous of Madagascar. Soc Vertebr Paleontol Mem 14. J Vertebr Paleontol 34 (6 Suppl):14–109

Kurtén B (1971) The Age of Mammals. Columbia University Press, New York

Kusuhashi N, Hu Y, Wang Y, Setoguchi T, Matsuoka H (2009) Two eobaatarid (Multituberculata; Mammalia) genera from the Lower Cretaceous Shahai and Fuxin formations, northeastern China. J. Vertebr Paleontol 29:1264–1288

Kusuhashi N, Wang Y, Jin X (2020) A new eobaatarid multituberculate (Mammalia) from the Lower Cretaceous Fuxin Formation, Fuxin-Jinzhou Basin, Liaoning, northeastern China. J Mammal Evol 27:605–623

Kwiecinski GC (1998) *Marmota monax*. Mammalian Species 591:1–8

Ladevèze S, de Muizon C, Colbert M, Smith T (2010) 3D computational imaging of the petrosal of a new multituberculate mammal from the Late Cretaceous of China and its paleobiologic inferences. Comptes Rendus Palevol 9:319–330

Lee WT (1913) Recent discovery of dinosaurs in the Tertiary. Am J Sci 35:531–534

Lemoine V (1880) Communication sur les ossements fossiles des terrains tertiaries inférieurs des environs de Reims. Association Française pour l'Avancement des Sciences, Congrès de Montpellier 8:585–594

Lillegraven JA, Hahn G (1993) Evolutionary analysis of the middle and inner ear of Late Jurassic multituberculates. J Mammal Evol 1:47–74

Lillegraven JA, Krusat G (1991) Cranio-mandibular anatomy of *Haldanodon exspectatus* (Docodonta; Mammalia) from the Late Jurassic of Portugal and its implications to the evolution of mammalian characters. Contrib Geol Univ Wyoming 28:39–138

Linnaeus C (1758) Systema naturæ per regna tria naturæ, secundum classes, ordines, genera, species, cum characteribus, differentiis, synonymis, locis. Tomus I. Editio decima, reformata. Laurentii Salvii, Holmiæ, 824 pp

Lofgren DL, Lillegraven JA, Clemens WA, Gingerich PD, Williamson TE (2004) Paleocene biochronology: the Puercan through Clarkforkian Land Mammal Ages. In: Woodburne MO (ed), Late Cretaceous and Cenozoic Mammals of North America: Biostratigraphy and Geochronology. Columbia University Press, New York, pp. 43–105

Lucas SG, Williamson TE, Middleton MD (1997) *Catopsalis* (Mammalia: Multituberculata) from the Paleocene of New Mexico and Utah: taxonomy and biochronological significance. J Paleontol 71:484–493

Luo Z-X (1989) The petrosal structures of Multituberculata (Mammalia) and the molar morphology of early Arctocyonidae (Condylarthra, Mammalia). PhD dissertation, University of California, Berkeley

Luo Z-X, Crompton AW, Lucas SG (1995) Evolutionary origins of the mammalian promontorium and cochlea. J Vertebr Paleontol 15:113–121

Luo Z-X, Crompton AW, Sun A-L (2001) A new mammaliaform from the Early Jurassic and evolution of mammalian characteristics. Science 292:1535–1540

Luo Z-X, Ketten DR (1991) CT scanning and computerized reconstructions of the inner ear of multituberculate mammals. J Vertebr Paleontol 11:220–228

Luo Z-X, Meng Q-J, Grossnickle DM, Liu D, Neander AI, Zhang Y-G, Ji Q (2017) New evidence for mammaliaform ear evolution and feeding adaptation in a Jurassic ecosystem. Nature 548:326–329

Luo Z-X, Ruf I, Martin T (2012) The petrosal and inner ear of the Late Jurassic cladotherian mammal *Dryolestes leiriensis* and implications for ear evolution in therian mammals. Zool J Linn Soc 166:433–463

Luo Z-X, Ruf I, Schultz JA, Martin T (2011) Fossil evidence on evolution of inner ear cochlea in Jurassic mammals. Proc Roy Soc B 278:28–34

Luo Z-X, Schultz JA, Ekdale EG (2016) Evolution of the middle and inner ears of mammaliaforms: the approach to mammals. In: Clack JA, Fay RR, Popper AN (eds), Evolution of the Vertebrate Ear: A Paleontological Perspective, Springer Handbook of Auditory Research 59:139–174. Springer International Publishing AG, Cham, Switzerland

Lyson TR, Joyce WG (2009a) A new species of *Palatobaena* (Testudines: Baenidae) and a maximum parsimony and Bayesian phylogenetic analysis of Baenidae. J Paleontol 83:457–470

Lyson TR, Joyce WG (2009b) A revision of *Plesiobaena* (Testudinies: Baenidae) and an assessment of baenid ecology across the K/T boundary. J Paleontol 83:833–853

Lyson TR, Joyce WG (2011) Cranial anatomy and phylogenetic placement of the enigmatic turtle *Compsemys victa* Leidy, 1856. J Paleontol 85:789–801

Lyson TR, Longrich NR (2011) Spatial niche partitioning in dinosaurs from the latest Cretaceous (Maastrichtian) of North America. Proc Roy Soc B 278:1158–1164

Lyson TR, Miller IM, Bercovici AD, Weissenburger K, Fuentes AJ, Clyde WC, Hagadorn JW, Butrim MJ, Johnson KR, Fleming RF, Barclay RS, Maccracken SA, Lloyd B, Wilson GP, Krause DW, Chester SGB (2019a) Exceptional continental record of biotic recovery after the Cretaceous-Paleogene mass extinction. Science 366:977–983

Lyson TR, Petermann H, Miller IM (2021b) A new plastomenid trionychid turtle, *Plastomenus joycei*, sp. nov. from the earliest Paleocene (Danian) Denver Formation of south-central Colorado, USA. J Vertebr Paleontol 41:e1913600

Lyson TR, Petermann H, Toth N, Bastien S, Miller IM (2021a) A new baenid turtle, *Palatobaena knellerorum*, sp. nov. from the lower Paleocene (Danian) Denver Formation of south-central Colorado, USA. J Vertebr Paleontol 41:e1925558

Lyson TR, Sayler JL, Joyce WG (2019b) A new baenid turtle, *Saxochelys gilberti*, gen. et sp. nov., from the uppermost Cretaceous (Maastrichtian) Hell Creek Formation: sexual dimorphism and spatial niche partitioning within the most speciose group of Late Cretaceous turtles. J Vertebr Paleontol 39:e1662428

Mao F-Y, Wang Y-Q, Meng J (2016) New specimens of the multituberculate mammal *Sphenopsalis* from China: implications for phylogeny and biology of taeniolabidoids. Acta Palaeontol Pol 61:429–454

Marsh OC (1880) Notice on Jurassic mammals representing two new orders. Am J Sci 20:235–239

Martin R (2018) Mesozoic mammals – early mammalian diversity and ecomorphological adaptations. In: Zachos FE, Asher RJ (eds), Handbook of Zoology, Mammalia. Mammalian Evolution, Diversity and Systematics. De Gruyter, Berlin, pp 199–299

Matthew WD (1937) Paleocene faunas of the San Juan Basin, New Mexico. Trans Am Phil Soc 30:1–510

Matthew WD, Granger W (1925) Fauna and correlation of the Gashato Formation of Mongolia. Am Mus Novitates 189:1–12

Matthew WD, Granger W, Simpson GG (1928) Paleocene multituberculates from Mongolia. Am Mus Novitates 331:1–4

McKenna MC (1975) Toward a phylogenetic classification of the Mammalia. In: Luckett WP, Szalay FS (eds), Phylogeny of the Primates. Cambridge University Press, Cambridge, pp 21–46

Meng J, Wyss AR (1995) Monotreme affinities and low-frequency hearing suggested by multituberculate ear. Nature 377:141–144

Meng J, Zhai R, Wyss AR (1998) The late Paleocene Bayan Ulan fauna of Inner Mongolia, China. Bull Carnegie Mus Nat Hist 34:148–185

Meng Q-J, Grossnickle DM, Liu D, Zhang Y-G, Neander AI, Ji Q, Luo Z-X (2017) New gliding mammaliaforms from the Jurassic. Nature 548:291–296

Miao D (1986) Dental anatomy and ontogeny of *Lambdopsalis bulla* (Mammalia, Multituberculata). Contrib Geol Univ Wyoming 24:65–76

Miao D (1988) Skull morphology of *Lambdopsalis bulla* (Mammalia, Multituberculata) and its implications to mammalian evolution. Contrib Geol Univ Wyoming Spec Pap 4:1–104

Middleton MD (1982) A new species and additional material of *Catopsalis* (Mammalia, Multituberculata) from the Western Interior of North America. J Paleontol 56:1197–1206

Middleton MD (1983) Early Paleocene vertebrates of the Denver Basin, Colorado. PhD dissertation, University of Colorado, Boulder

Montellano M, Weil A, Clemens WA (2000) An exceptional specimen of *Cimexomys judithae* (Mammalia: Multituberculata) from the Campanian Two Medicine Formation of Montana, and the phylogenetic status of *Cimexomys*. J Vertebr Paleontol 20:333–340

Nichols DJ, Fleming RF (2002) Palynology and palynostratigraphy of Maastrichtian, Paleocene, and Eocene strata in the Denver Basin, Colorado. Rocky Mtn Geol 37:135–163

Novacek MJ (1986) The skull of leptictid insectivorans and the higher-level classification of eutherian mammals. Bull Am Mus Nat Hist 183:1–112

Ogg JG (2012) Geomagnetic polarity time scale. In Gradstein FM, Ogg JG, Schmitz MD, Ogg GM (eds), The Geologic Time Scale 2012 (first edition). Elsevier, Boston, pp 85–113

Osborn HF, Earle C (1895) Fossil mammals of the Puerco beds. Collection of 1892. Bull Am Mus Nat Hist 7:1–70

Panciroli E, Schultz JA, Luo Z-X (2018) Morphology of the petrosal and stapes of *Borealestes* (Mammaliaformes, Docodonta) from the Middle Jurassic of Skye, Scotland. Pap Palaeontol 5:139–156

Poole WE (1982) *Macropus giganteus*. Mammalian Species 187:1–8

Prothero DR (2017) The Princeton Field Guide to Prehistoric Mammals. Princeton University Press, Princeton

Pusch LC, Kammerer CF, Fröbisch J (2019) Cranial anatomy of the early cynodont *Galesaurus planiceps* and the origin of mammalian endocranial characters. J Anat 234:592–621

Rădulescu C, Samson P-M (1996) The first multituberculate skull from the Late Cretaceous (Maastrichtian) of Europe (Haţeg Basin, Romania). Anuarul Institutului Geologic al României 69:177–178

Rădulescu C, Samson P-M (1997) Late Cretaceous Multituberculata from the Haţeg Basin (Romania). Sargetia 17:247–255

Rager L, Hautier L, Forasiepi A, Goswami A, Sánchez-Villagra MR (2014) Timing of cranial suture closure in placental mammals: phylogenetic patterns, intraspecific variation, and comparison with marsupials. J Morph 275:125–140

Raynolds RG (1997) Synorogenic and post-orogenic strata in the central Front Range, Colorado. In: Boyland DB, Sonnenberg SS (eds), Geologic History of the Colorado Front Range. Rocky Mtn Assoc Geol, Denver, pp 43–47

Raynolds RG (2002) Upper Cretaceous and Tertiary stratigraphy of the Denver Basin, Colorado. Rocky Mtn Geol 37:111–134

Raynolds RG, Johnson KR (2003) Synopsis of the stratigraphy and paleontology of the uppermost Cretaceous and lower Tertiary strata in the Denver Basin, Colorado. Rocky Mtn Geol 38:171–181

Romer AS (1966) Vertebrate Paleontology. The University of Chicago Press, Chicago

Rose KD (2006) The Beginning of the Age of Mammals. Johns Hopkins University Press, Baltimore

Rougier GW, Martinelli AG, Forasiepi AM (2021) Mesozoic Mammals from South America and their Forerunners. Springer, Cham, Switzerland

Rougier GW, Novacek MJ, Dashzeveg D (1997) A new multituberculate from the Late Cretaceous locality Ukhaa Tolgod, Mongolia. Considerations on multituberculate interrelationships. Am Mus Novitates 3191:1–26

Rougier GW, Sheth AS, Carpenter K, Appella-Guiscafre L, Davis BM (2015) A new species of *Docodon* (Mammaliaformes: Docodonta) from the Upper Jurassic Morrison Formation and a reassessment of selected craniodental characters in basal mammaliaforms. J Mammal Evol 22:1–16

Rougier GW, Sheth AS, Spurlin BK, Bolortsetseg M, Novacek MJ (2016) Craniodental anatomy of a new Late Cretaceous multituberculate mammal from Udan Sayr, Mongolia. Palaeontol Pol 67:197–248

Rougier GW, Wible JR, Hopson JA (1992) Reconstruction of the cranial vessels in the Early Cretaceous mammal *Vincelestes neuquenianus*: implications for the evolution of the mammalian cranial vascular system. J Vertebr Paleontol 12:188–216

Rougier GW, Wible JR, Hopson JA (1996a) Basicranial anatomy of *Priacodon fruitaensis* (Triconodontidae, Mammalia) from the Late Jurassic of Colorado, and a reappraisal of mammaliaform interrelationships. Am Mus Novitates 3183:1–38

Rougier GW, Wible JR, Novacek MJ (1996b) Middle-ear ossicles of the multituberculate *Kryptobaatar* from the Mongolian Late Cretaceous: implications for mammaliamorph relationships and the evolution of the auditory apparatus. Am Mus Novitates 3187:1–43

Rowe TB (1986) Osteological diagnosis of Mammalia, L. 1758, and its relationships to extinct Synapsida. PhD dissertation, University of California, Berkeley

Rowe TB (1988) Definition, diagnosis, and origin of Mammalia. J Vertebr Paleontol 8:241–264

Ruf I, Luo Z-X, Martin T (2013) Reinvestigation of the basicranium of *Haldanodon exspectatus* (Mammaliaformes, Docodonta). J Vertebr Paleontol 33:382–400

Ruf I, Luo Z-X, Wible JR, Martin T (2009) Petrosal anatomy and inner ear structures of the Late Jurassic *Henkelotherium* (Mammalia, Cladotheria, Dryolestoidea): insight into the early evolution of the ear region in cladotherian mammals. J Anat 214:679–693

Russell LS (1926) A new species of the genus *Catopsalis* Cope from the Paskapoo Formation of Alberta. Am J Sci 12:230–234

Savage RJG, Long MR (1986) Mammal Evolution, An Illustrated Guide. British Museum (Natural History), London

Schultz JA, Martin T (2015) The inner and middle ear of Jurassic paulchoffatiid multituberculates. J Vertebr Paleontol, Progr Abstr 2015:210

Schultz JA, Zeller U, Luo Z-X (2017) Inner ear labyrinth anatomy of monotremes and implications for mammalian inner ear evolution. J Morph 278:236–263

Schumaker KK, Kihm AJ (2006) Multituberculates from the Medicine Pole Hills local fauna (Chadronian) of Bowman County, North Dakota. Paludicola 6:9–21

Scott CS, Weil A, Theodor JM (2016) A new diminutive species of *Catopsalis* (Mammalia, Multituberculata, Taeniolabidoidea) from the early Paleocene of southwestern Alberta, Canada. J Paleontol 92:896–910

Scott WB (1913) A History of Land Mammals in the Western Hemisphere. The MacMillan Company, New York

Sereno PC (2006) Shoulder girdle and forelimb in multituberculates: evolution of parasagittal forelimb posture in mammals. In: Carrano MT, Gaudin TJ, Blob RW, Wible JR (eds), Amniote Paleobiology: Perspectives on the Evolution of Mammals, Birds, and Reptiles. University of Chicago Press, Chicago, pp 315–366

Simmons NB (1986) *Taeniolabis* Cope, 1882 (Mammalia, Multituberculata): proposed designation of *Polymastodon taoensis* Cope, 1882 as type species. Bull Zool Nom 43:310–314

Simmons NB (1987) A revision of *Taeniolabis* (Mammalia: Multituberculata), with a new species from the Puercan of eastern Montana. J Paleontol 61:794–808

Simmons NB (1993) Phylogeny of Multituberculata. In: Szalay FS, Novacek MJ, McKenna MC (eds), Mammal Phylogeny; Mesozoic Differentiation, Multituberculates, Monotremes, Early Therians, and Marsupials. Springer-Verlag, New York, pp 146–164

Simmons NB, Miao D (1986) Paraphyly in *Catopsalis* (Mammalia: Multituberculata) and its biogeographic implications. Contrib Geol Univ Wyoming Spec Pap 3:87–94

Simpson GG (1926) Mesozoic Mammalia. IV. The multituberculates as living mammals. Am J Sci 11:228–250

Simpson GG (1927) Mammalian fauna and correlation of the Paskapoo Formation of Alberta. Am Mus Novitates 268:1–10

Simpson GG (1935) The first mammals. Q Rev Biol 10:154–180

Simpson GG (1937a) The beginning of the Age of Mammals. Biol Rev 12:1–46

Simpson GG (1937b) Skull structure of the Multituberculata. Bull Am Mus Nat Hist 73:727–763

Simpson GG (1937c) The Fort Union of the Crazy Mountain Field, Montana and its mammalian faunas. US Natl Mus Bull. 169:1–287

Simpson GG (1970) The Argyrolagidae, extinct South American marsupials. Bull Mus Comp Zool 139:1–86

Sloan RE (1979) Multituberculata. In: Fairbridge RW, Jablonski D (eds), The Encyclopedia of Paleontology. Dowden, Hutchinson & Ross, Stroudsberg, pp 492–498

Sloan RE (1981) Systematics of Paleocene multituberculates from the San Juan Basin, New Mexico. In: Lucas SG, Rigby JK, Kues BS (eds), Advances in San Juan Basin Paleontology. University of New Mexico Press, Albuquerque, pp 127–160

Sloan RE, Van Valen L (1965) Cretaceous mammals from Montana. Science 148:220–227

Smith T, Codrea V (2015) Red iron-pigmented tooth enamel in a multituberculate mammal from the Late Cretaceous Transylvanian "Haţeg Island." PLoS One 10:e0132550

Smith T, Guo D-Y, Sun Y (2001) A new species of *Kryptobaatar* (Multituberculata): the first Late Cretaceous mammal from Inner Mongolia (P. R. China). Bull l'Inst roy Sci nat de Belgique, Sci de la Terre, Suppl 71:29–50

Solomon A, Codrea V, Venczel M, Dumbrava M, Smith T (2016) New remains of the multituberculate mammal *Barbatodon* from the Upper Cretaceous of the Haţeg Basin (Romania). J Mammal Evol 23:319–335

Sues H-D (1986) The skull and dentition of two tritylodontid synapsids from the Lower Jurassic of western North America. Bull Mus Comp Zool, Harvard University 151:217–268

Szalay FS, Trofimov BA (1996) The Mongolian Late Cretaceous *Asiatherium*, and the early phylogeny and paleobiogeography of Metatheria. J Vertebr Paleontol 16:474–509

Tsentas C (1981) Mammalian biostratigraphy of the middle Paleocene (Torrejonian) strata of the San Juan Basin: notes on Torreon Wash and the status of the *Pantolambda* and *Deltatherium* faunal "zones". In: Lucas SG, Rigby JK, Kues BS (eds), Advances in San Juan Basin Paleontology. University of New Mexico Press, Albuquerque, pp 264–292

Vianey-Liaud M (1979) Les mammifères montiens de Hainin (Paléocènes moyen de Belgique). Part I: Multituberculés. Palaeovertebrata 9:117–131

Vianey-Liaud M (1986) Les Multituberculés Thanetiens de France, et leur rapports avec le Multituberculés Nord-Americains. Palaeontogr Abt A 191:85–171

Wall CE, Krause DW (1992) A biomechanical analysis of the masticatory apparatus of *Ptilodus* (Multituberculata). J Vertebr Paleontol 12:172–187

Weaver LN, Varricchio DJ, Sargis EJ, Chen M, Freimuth WJ, Wilson Mantilla GP (2021) Early mammalian social behavior revealed by multituberculates from a dinosaur nesting site. Nature Ecol & Evol 5:32–37

Weaver LN, Wilson GP (2020) Shape disparity in the blade-like premolars of multituberculate mammals: functional constraints and the evolution of herbivory. J Mammalogy 102:967–985

Weil A, Krause DW (2008) Multituberculata (Chapter 2). In: Janis CM, Gunnell GF, Uhen MD (eds), Evolution of Tertiary Mammals of North America. Volume 2: Small Mammals, Xenarthrans, and Marine Mammals. Cambridge University Press, Cambridge, pp 19–38

Weil A, Tomida Y (2001) First description of the skull of *Meniscoessus robustus* expands known morphological diversity of Multituberculata and deepens phylogenetic mystery. J Vertebr Paleontol 21 (3 Suppl):112A

Weil A, Tomida Y (2003) Detailed cranial anatomy and phylogenetic affinities of the multituberculate *Meniscoessus*. J Vertebr Paleontol 23 (3 Suppl):108A

Weil A, Tomida Y (2017) Inner ear of the cimolodontan multituberculate *Meniscoessus robustus* supports functional interpretation and a novel phylogenetic hypothesis. The FASEB Journal 31(S1)

Wible JR (1991) Origin of Mammalia: the craniodental evidence reexamined. J Vertebr Paleontol 11:1–28

Wible JR, Hopson JA (1995) Homologies of the prootic canal in mammals and non-mammalian cynodonts. J Vertebr Paleontol 15:331–356

Wible JR, Rougier GW (2000) Cranial anatomy of *Kryptobaatar dashzevegi* (Mammalia, Multituberculata), and its bearing on the evolution of mammalian characters. Bull Am Mus Nat Hist 247:1–124

Wible JR, Rougier GW (2017) Craniomandibular anatomy of the subterranean meridiolestidan *Necrolestes patagonensis* Ameghino, 1891 (Mammalia, Cladotheria) from the early Miocene of Patagonia. Ann Carnegie Mus 84:183–252

Wible JR, Shelley SL, Bi S (2019) New genus and species of djadochtatheriid multituberculate (Allotheria, Mammalia) from the Upper Cretaceous Bayan Mandahu Formation of Inner Mongolia. Ann Carnegie Mus 85:285–327

Wible JR, Wang Y, Li C, Dawson MR (2005) Cranial anatomy and relationships of a new ctenodactyloid (Mammalia, Rodentia) from the early Eocene of Hubei Province, China. Ann Carnegie Mus 74:91-150

Williamson TE, Brusatte SL, Carr TD, Weil A, Standhardt BE (2012) The phylogeny and evolution of Cretaceous–Palaeogene metatherians: cladistic analysis and description of new early Palaeocene specimens from the Nacimiento Formation, New Mexico. J Syst Palaeontol 10:625–651

Williamson TE, Brusatte SL, Secord R, Shelley S (2016) A new taeniolabidoid multituberculate (Mammalia) from the middle Puercan of the Nacimiento Formation, New Mexico, and a revision of taeniolabidoid systematics and phylogeny. Zool J Linn Soc 177:183–208

Wilson GP, Ekdale EG, Hoganson JW, Calede JJ, Vander Linden A (2016) A large carnivorous mammal from the Late Cretaceous and the North American origin of marsupials. Nature Comm 7:13734

Wilson GP, Evans AR, Corfe IJ, Smits PD, Fortelius M, Jernvall J (2012) Adaptive radiation of multituberculate mammals before the extinction of dinosaurs. Nature 483:457–460

Wilson LAB, Sánchez-Villagra M (2009) Heterochrony and patterns of cranial suture closure in hystricognath rodents. J Anat 214:339–354

Wilson RW (1987) Late Cretaceous (Fox Hills) multituberculates from the Red Owl Local Fauna of western South Dakota. Dakoterra 3:118–122

Xu L, Zhang X, Pu H, Jia S, Zhang J, Lü J, Meng J (2015) Largest known Mesozoic multituberculate from Eurasia and implications for multituberculate evolution and biology. Sci Rep 5:14950

Yuan C-X, Ji Q, Meng Q-J, Tabrum AR, Luo Z-X (2013) Earliest evolution of multituberculate mammals revealed by a new Jurassic fossil. Science 341:779–783